NOTE TO USERS

Université d'Ottawa · University of Ottawa

Université d'Ottawa · University of Ottawa

FACULTÉ DE ÉTUDES SUPÉRIEURES ET POSTDOCTORALES

FACULTY OF GRADUATE AND POSTDOCTORAL STUDIES

Simone DUMAS

AUTEUR DE LA THÈSE - AUTHOR OF THESIS

Ph.D. (Earth Sciences)

GRADE - DEGREE

Department of Earth Science

FACULTÉ, ÉCOLE, DÉPARTEMENT - FACULTY, SCHOOL, DEPARTMENT

TITRE DE LA THÈSE - TITLE OF THE THESIS

Oscillatory-Flow and Combined-Flow Bed Forms : Experimental Investigation for the Shallow Marine Rock Record

B. Arnott

DIRECTEUR DE LA THÈSE - THESIS SUPERVISOR

CO-DIRECTEUR DE LA THÈSE - THESIS CO-SUPERVISOR

EXAMINATEURS DE LA THÈSE - THESIS EXAMINERS

R.J. Cheel

A. Desrochers

R. Rainbird

C. Rennie

J.-M. De Koninck, Ph.D.

LE DOYEN DE LA FACULTÉ DES ÉTUDES SUPÉRIEURES ET POSTDOCTORALES

DEAN OF THE FACULTY OF GRADUATE AND POSTDOCTORAL STUDIES

OSCILLATORY-FLOW AND COMBINED-FLOW BED FORMS
•
EXPERIMENTAL INVESTIGATION AND IMPLICATIONS FOR THE SHALLOW MARINE ROCK RECORD

by

Simone Dumas

A thesis submitted to the School of Graduate Studies
in partial fulfillment of the requirements of the degree of Ph.D. in Earth Sciences

OTTAWA-CARLETON GEOSCIENCE CENTRE
UNIVERSITY OF OTTAWA
OTTAWA, ONTARIO, CANADA

Your file Votre référence
ISBN: 0-494-01697-3
Our file Notre référence
ISBN: 0-494-01697-3

ABSTRACT

Long-period, storm-related oscillatory and combined-flows are thought to be responsible for much of the sand-sized sediment transport on the continental shelf. Yet, the relationship between these flow conditions and associated bed forms is still poorly understood. This study provides new experimental data aimed at characterizing equilibrium bed forms developed under long-period oscillatory and combined-flow conditions. Runs were conducted in a large combined-flow tunnel. Conditions explored were: oscillatory velocities (U_0) of 20-125 cm/s, unidirectional velocities (U_u) of 0-25 cm/s, oscillation period (T) of 10.5 s and 8 s, and grain size of 0.14 mm and 0.22 mm. For conditions of increasing U_0 the bed phases generated were: anorbital small-scale ripples (wavelength < 20 cm), orbital large-scale ripples (wavelength > 100 cm), and plane bed. For a given U_0 and increasing U_u, the bed generally becomes progressively more asymmetric and is eventually planed flat.

Hummocky bed forms developed under moderate oscillatory velocities (50 cm/s < U_0 < 90 cm/s) and low unidirectional velocities (0 cm/s < U_u < 15 cm/s). "Synthetic" stratification generated by these hummocky bed forms exhibits many of the features of hummocky cross-stratification (HCS). For purely oscillatory flows conditions, the addition of a weak Uu (≥ 5 cm/s) causes the stratification to become anisotropic. For greater Uu (> 10-12 cm/s) the resultant cross-stratification becomes similar to that produced by unidirectional-flow dunes.

Potential genetic differences between HCS and swaley-cross stratification (SCS) were also investigated. Higher aggradation rates increased the preservation potential of hummocks which, as a consequence, increased the likelihood of forming HCS versus SCS. A cross-shelf depositional model is proposed in which HCS forms above storm

wave base under moderate aggradation rates, whereas SCS forms at shallower depth under lower deposition/transport ratios resulting in lower aggradation rates.

Results from these experiments suggest that HCS ad SCS are genetically linked to the hummocky bed forms generated under long period, oscillatory flows and oscillatory-dominant combined flows. As long-period, high-energy waves require deep, wide basins to form, HCS and SCS may therefore serve as useful indicators of deposition in unrestricted, open water conditions.

RÉSUMÉ

Il est généralement reconnu que les courants oscillatoires et combinés (oscillatoires et unidirectionnels) de longues périodes communément générés lors de fortes tempêtes sur le plateau continental sont responsables du transport sédimentaire dans ces environnements. En dépit de cette réalité, la relation entre ces courants et les figures de courants qu'ils génèrent est encore très peu comprise. Cette étude fournit de nouvelles données expérimentales visant à caractériser les figures de courants qui sont formées par des courants oscillatoires et combinés de longues périodes. Des essais furent complétés dans un tunnel mesurant 15m de long, 1.25m de large et 0.65m de profond permettant des variations de conditions de courant et de type de sédiments. Les conditions explorées furent: velocités du courant oscillatoire (U_0) de 20-125 cm/s, velocité du courant unidirectionnel (U_u) de 0-25 cm/s, période d'oscillation (T) de 10.5 et 8 s et taille des sédiments de 0.14mm et 0.22 mm (sables fins). Les courants unidirectionnels et oscillatoires étaient colinéaires et toutes les variables ramenées à 10°C. Les résultats obtenus correspondent généralement à ceux d'études antérieures similaires et démontrent que lors d'une augmentation de U_0 la séquence de figures de courant est la suivante: rides anorbitales de petite échelle (longueur d'onde < 20 cm), rides orbitales de grande échelle (longueur d'onde > 100 cm) et litage planaire ("plane bed"). Pour une valeur fixe de U_0 accompagnée d'une augmentation de U_u, le lit de sédiments devient progressivement plus asymétrique et s'aplanit éventuellement. Les figures de courants démontrent une migration dans le sens du courant unidirectionnel non-équivoque lorsque U_u dépasse 10-12 cm/s.

Une analyse détaillée de la géométrie des figures de courants a été réalisée afin de permettre la détermination de caractéristiques diagnostiques. Le rapport de la longueur d'onde (λ) et de la hauteur d'une ride ne s'avère pas diagnostique puisqu'il

varie peu (8-12) et ce, pour toutes les figures de courants générées. Le rapport de λ et du diamètre de l'orbite d'oscillation (d_0) est utilisé afin de quantifier la relation entre la taille des figures de courants et l'ampleur du mouvement oscillatoire. La longueur d'onde des rides de petite échelle n'est pas fonction du diamètre de l'orbite du mouvement oscillatoire et elles sont dites anorbitales, tandis que les rides de grande échelle obéissant à la relation $d_0/\lambda \sim 2$ sont dites orbitales. L'indice de sphéricité, une mesure de la convexité du dos de la ride, est maximal pour les figures de courants mamelonnées ("hummocky bed forms").

Les figures de courants mamelonnées se forment sous l'action de forts courants oscillatoires (50 cm/s < U_0 < 90 cm/s) et de faibles courants unidirectionnels (0 cm/s < U_u < 15 cm/s). Les caractéristiques diagnostiques des figures de courants mamelonnées incluent: 1) la symétrie et le faible angle d'inclinaision du dos et de la face d'avalanche de la figure de courants; 2) la longueur d'onde élevée (de l'ordre du mètre); 3) la zone de crête tri-dimensionelle; 4) la forme biconvexe (vue de profil); et 5) l'absence d'un sommet de face d'avalanche bien défini. Les structures en mamelons sont mieux développées lors d'essais sous l'influence de la plus longue des périodes d'oscillation (10.5 s) et persistent jusqu'à des valeurs de courants unidirectionnels plus élevés ($U_u \sim$ 17 cm/s) avec le sable plus fin (0.14 mm). Le stratification "synthétique" construite par ces figures de courants mamelonnées présente plusieurs des caractéristiques des structures de stratification entrecroisée en mamelons ("hummocky cross-stratification") retrouvées dans les roches sédimentaires. Lors de conditions de courants purement oscillatoires ou de courants combinés à faible composante unidirectionnelle (U_u < 5 cm/s), la stratification est isotropique. Pour un courant unidirectionnel plus élevé (5-10 cm/s), la stratification devient anisotropique mais l'angle d'inclinaision de la face d'avalanche demeure faible. Éventuellement, pour un U_u > 10-12 cm/s, les structures mamelonnées développent de plus forts angles d'inclinaision et une asymétrie, puis

commencent à migrer dans le sens du courant undirectionel ce qui résulte en une stratification qui ressemble beaucoup à celle produite par des dunes de courant purement unidirectionnel. Par conséquent, les résultats de ces expériences suggèrent qu'une grande partie de la stratification entrecroisée en mamelons observée dans les roches sédimentaires serait formée sous l'influence de courants oscillatoires élevés (> ~ 50 cm/s) et de longues périodes (> ~ 8 s), et de faibles courants unidirectionnels (< ~ 12 cm/s). Puisqu'une vaste étendue d'eau est nécessaire à la formation de vagues de longues périodes et de haute-énergie, il s'en suit que la stratification entrecroisée en mamelons pourait servir d'indicateur de dépôt en milieu marin à bassin ouvert.

Cette étude s'est aussi penchée sur l'identification de possibles différences génétiques entre la stratification entrecroisée en mamelons et la stratification entrecroisée en auges ("swaley cross-stratification"). Dans cette perspective, un lit comportant des structures mamelonnées a été alluvionné de façon synthétique à des taux de 4.2 mm/min et 1 mm/min. Le taux de déposition le plus élevé s'est avéré favorable à la préservation des structures en mamelons et, par conséquent, a favorisé la formation de stratification entrecroisée en mamelons au détriment de la stratification entrecroisée en auges. Sur une coupe longitudinale d'un profil de dépôt potentiel appartenant au plateau continental, la stratification entrecroisée en mamelons se forme au dessus (mais près) de la limite d'influence des vagues de tempête, sous des courants combinés dominés par la composante oscillatoire, sous des taux de déposition modérés, et également sous des conditions de préservation optimales. Par opposition, la stratification entrecroisée en auges se forme également sous des courants combinés dominés par la composante oscillatoire mais à des profondeurs moindres et sous des conditions où le plus faible rapport dépôt/transport résulte en de plus faibles taux de dépôt. Les relations paléogéographique et stratigraphique proposées entre la stratification entrecroisée en mamelons et la stratification entrecroisée en auges sont en

accord avec les observations faites lors d'études de roches déposées dans des milieux marins peu profonds.

ACKNOWLEGEMENTS

First and foremost, Bill Arnott is thanked for his infectious enthusiasm and his timely support, even when faced with proliferating students! I'm grateful to John Southard for giving me my first welding lesson; it proved to be one of the most useful lessons of the project. I've also learned a lot from John's motto: "why buy it when you can build it yourself?" Sound advice on many aspects of the Ph.D. process was often sought from thesis veteran Hazen Russell. Don Cummings contributed throughout the whole process, from grinding steel to surviving the Pikans; I'm glad we were in this together! Lab assistants Andrew Wigston, Andrew Buttle, Ralph Rowe, and Elizabeth Powles are thanked for their help during the construction and data collection phases. Valuable technical advice was provided by several experimental sedimentologists at the MIT Sed Lab, in particular Miwa Yokokawa, Jeff Parson, and Jim Buttles. Construction and early experimental phases were facilitated thanks to the expertise of Andy Gallant and Kevin O'Keefe of the MIT Central Machine Shop, and Ben Olsen and Bill Mallonée of the Terracon Corporation. Jamie Peets's expertise proved to be very valuable during the critical times of design reevaluation and wave-drive modifications. Holliston Sand Co. is gratefully acknowledged for supplying 16 tons of sand, free of charge ! I'm also greatly indebted to Léo's entourage for freeing up some crucial thesis writing time, especially during the final sprint of the last few months. Finally, I would like to thank the following funding agencies for their financial support: the Natural Science and Engineering Research Council of Canada, le Fonds de recherche sur la nature et les technologies (Gouvernement du Québec), the Ontario Graduate Scholarship in Science and Technology, the University of Ottawa, and the Alice E. Wilson fund.

TABLE OF CONTENTS

LIST OF FIGURES

LIST OF TABLES

CHAPTER 1

INTRODUCTION

RATIONALE

Despite the ubiquity of physical sedimentary structures in the geological record, and the breadth of flow conditions under which they form, remarkably few diagnostic criteria are available to relate bed form geometry to flow conditions. Bed forms are typically sub-divided into three broad categories: 1) unidirectional-flow (current) bed forms, 2) oscillatory-flow (wave) bed forms, and 3) combined-flow (wave-current) bed forms (Harms 1969). For unidirectional-flow bed forms, the genetic relationship between flow conditions and bed form geometry is well established (Southard and Boguchwal 1990), and similarly for small-scale (wavelength < 20 cm) oscillatory-flow ripples (Miller and Komar 1980b). In contrast, genetic relationships for larger-scale oscillatory-flow bed forms (Southard et al. 1990), as well as virtually all combined-flow bed forms (Arnott and Southard 1990; Yokokawa 1995), remain poorly understood. Hummocky bed forms, which are widely believed to form hummocky cross-stratification, are one of these large-scale bed forms and are of specific interest because they are believed to be good indicators of high-energy storm events on continental shelves (e.g., Cheel and Leckie 1993). It is during these events that most of the nearshore sand-sized sediment is thought to be transported offshore and deposited to form the modern and ancient shallow marine sedimentary record (Snedden et al. 1988). However, due to the limited

size of experimental flumes needed or to logistical challenges, these more extreme flow conditions are difficult to reproduce in the laboratory or to study in-situ.

OBJECTIVES

The general objective of this work was to study oscillatory-flow and combined-flow equilibrium bed forms generated in the laboratory under long-period oscillatory flows. These data, in turn, will help further our understanding of shallow marine storm deposits. More specifically, the objectives of the study were to:

(1) Construct phase diagrams representing the equilibrium bed phase for the range of oscillatory and unidirectional velocities, oscillation periods, and grain sizes explored.

(2) Describe in detail the morphological characteristics of the different bed forms and provide diagnostic criteria to facilitate the differentiation of unidirectional, oscillatory, and combined-flow bed forms.

(3) Study the effect of unidirectional current velocity and bed aggradation rate on 3D symmetric large-scale bed forms (hummocky bed forms) and associated stratification.

Bed forms were generated in a combined-flow tunnel that acted as a forced damped harmonic oscillator, and made the production of long-oscillation period possible (Southard et al. 1990). In addition, to the best of our knowledge, the tunnel was the widest and second deepest of similar devices used to date, and therefore permitted the development of equilibrium large-scale bed forms more comparable in size to their natural counterparts, while at the same time minimizing the influence of the walls and ceiling. The maximum oscillatory velocity of 125 cm/s was also among the highest ever produced in the laboratory. This made it possible to explore the upper limit of bed form stability where all positive topographic elements are planed flat to form a plane bed. For

these reasons, we believe this study is the most comprehensive work to date on experimentally generated, long-period oscillatory-flow and combined-flow bed forms. The results of the study should help in developing a better understanding of the shallow marine depositional record.

SHALLOW MARINE SEDIMENTARY PROCESSES: CURRENT STATE OF KNOWLEDGE

Wave and combined flow boundary layers - Sediment is very commonly transported by fluids (e.g., water, ice, wind, high-concentration flows). One inherent property of fluids is viscosity, the internal resistance of a fluid to deformation (i.e. flow) (Allen 1985). When flowing over a solid boundary, viscous fluids develop a zone of fluid retardation close to that boundary. This zone, called a boundary layer, is the direct expression of the fluid's viscosity in response to the frictional resistance exerted by the boundary on the fluid. In the boundary layer, the velocity of the fluid changes from that of the boundary, which by the no-slip condition is zero, to that of the unaffected part of the flow (potential flow) some distance away from the boundary (Middleton and Southard 1978) (see Fig. 1.1). Boundary layers exhibit different velocity gradients depending on the flow regimes under which they form. For example, boundary layers that develop under deep, steady unidirectional flows are thick with low velocity gradients and accordingly low shear stresses. In contrast, oscillatory flow boundary layers are generally thin since they have little time to grow before the flow reverses and collapses the boundary layer every half oscillation period. As a result, oscillatory boundary layers typically have steep velocity gradients and high shear stresses. In the oceans, the high shear stress associated with the bottom boundary layer allows for the exchange of sediment particles, chemicals, and organisms between the sea bed and overlying water

column (Grant and Madsen 1986). For this reason, boundary layers have been of interest to engineers, oceanographers, physicists, and geologists. Of particular importance is the complex boundary layer that results from the interaction of unidirectional and oscillatory flows near the ocean bottom (see Fig. 1.1). In 1979, Grant and Madsen modeled the near-bottom combined-flow boundary layer and reported that the unidirectional-flow and oscillatory-flow boundary layers interact non-linearly, and that the combined bed shear stress was greater than the sum of their individual shear stresses. Their work was followed by other studies that developed similar predictive models and confirmed the work of Grant and Madsen (e.g., Davies et al. 1988; Fredsoe 1984; Li and Amos 1998; Li et al. 1997; Li and Davies 1996; Tanaka 1986; Tanaka et al. 1991; Wiberg 1995). This non-linear interaction has important implications for the understanding and prediction of sediment transport on continental shelves. For example, Manighetti and Carter (1999) estimated that the superimposition of two-meter high waves on a near-bottom current of 50 cm/s could enhance sediment transport rates by up to 50 times.

Sediment movement under oscillatory and combined flow - Within the boundary layer, the mechanisms by which sediment particles are entrained by a moving fluid have been studied extensively. The threshold for grain movement is a function of the grain-entrainment forces exerted by a moving fluid on a grain (lift and drag) versus the forces that oppose grain movement (weight, friction, and cohesion). One common way of representing sediment entrainment conditions is the experimentally derived Shields diagram where thresholds of sediment motion in a unidirectional flow are plotted on a graph of dimensionless bed shear stress versus grain Reynolds number. Bagnold (1946) was the first to attempt to represent sediment-movement thresholds for quartz grains of various sizes under the influence of wave motion, while Cartens et al. (1969) were the

first to plot a Shields diagram for oscillatory flow. In 1973, Komar and Miller compiled the data from four experimental studies on sediment-movement threshold including the work of Bagnold (1946) and Cartens et al. (1969), and established a modified Shields diagram for the entrainment of quartz grains of various diameters by oscillatory flows with varying oscillation period (Komar and Miller 1973). Similar work on oscillatory-flow sediment-movement thresholds soon followed (e.g., Dingler 1979; Lofquist 1978), and eventually, modified Shields diagrams for combined flows were proposed (Paphitis et al. 2001). It is generally accepted that unidirectional flow movement threshold criteria are not applicable to oscillatory and combined flows. This is due to the important influence of oscillation period on sediment movement under the influence of oscillating flows. At higher oscillation period, a thicker boundary layer develops, and as a consequence, a higher oscillatory velocity is needed to move sediment of a given grain size (Dingler 1979; Komar and Miller 1973; Lofquist 1978; Paphitis et al. 2001). Furthermore, under combined flows, oscillation period is observed to dictate how the unidirectional current and wave component combine in order to initiate sediment movement. Long-period oscillatory flows were measured to combine linearly with a superimposed current while under short oscillation periods, the effects of both flows were observed to decouple (Paphitis et al. 2001).

Bed forms - Once the sediment movement threshold is exceeded and sediment is entrained by the flow, small topographic elements, known as bed forms, start to develop on the bed. In 1946, Bagnold oscillated a bed of sediment under a stationary water column to experimentally generate oscillatory-flow bed forms. Just beyond movement threshold, he observed the formation of a series of flow transverse parallel rows that were a few grain diameters high, which he called rolling-grain ripples. For velocities of approximately twice the critical oscillatory velocity for grain motion a higher

relief type of ripple formed, and was termed vortex ripple for the characteristic flow-separation-induced vortices that swept from trough to crest every half cycle. Subsequently, others claimed to have generated rolling-grain ripples in the laboratory (Allen 1979; Sleath 1976), but Miller and Komar (1980a) attributed their formation to the suppression of vortices by the oscillating-bed type of apparatus. Others have also criticized the oscillating-bed apparatus suggesting that it introduces unnatural inertial forces on the sediment grains, and because experimental results are commonly inconsistent with those derived from flumes and tunnels (Brebner and Riedel 1973; Carstens et al. 1969; Miller and Komar 1980b). In the 1960's, 1970's and early 1980's, other experimental studies of oscillatory-flow bed forms followed the initiative of Bagnold (e.g., Brebner and Riedel 1973; Carstens et al. 1969; Dingler 1979; Kennedy and Falcon 1965; Lofquist 1978; McKee 1965; Miller and Komar 1980b; Sleath 1976). Experimental set-ups, flow conditions, and bed form characteristics from these experiments are summarized in Table 1.1. At the same time, Clifton et al. (1971, 1976) proposed a model for bed forms observed on a modern unbarred shoreface while others developed equations relating wave-ripple geometry to paleohydraulic conditions (Allen 1979; Clifton and Dingler 1984; Komar 1974; Sleath 1976). Another attempt at relating flow conditions and ripple geometry was made by Miller and Komar (1980b) who categorized wave ripples according to the relationship between ripple wavelength and wave orbital diameter. The objective of all these studies was to aid geologists in interpreting part of the ancient shallow marine sedimentary record. However, most of these experimental set-ups could only generate short oscillation periods, generally only a few seconds; few had investigated bed forms produced under long oscillation periods. In 1990, Southard et al. were the first to investigate bed forms generated by high-velocity long-period flows, conditions thought to be representative of those in shallow water during storms (i.e., when most of the sand-sized sediment transport occurs). One of their observations was

that spacing of oscillatory flow ripples was split into two distinct populations (spacing ≤ 50 cm, and spacing > 100 cm) with seemingly no intermediate-sized ripples (see their Fig. 11). In the same year, Southard and Boguchwal (1990) published a synthesis of unidirectional flume data presenting bed forms as a function of depth, grain size, and flow velocity in the form of a series of phase diagrams (see Fig. 1.2A). A similar compilation for experimental data of oscillatory-flow bed forms, as a function of orbital velocity and oscillation period was presented in Harms et al. (1982) (see Fig. 1.2B). Based on exploratory experimental work, a preliminary combined-flow phase diagram was drafted by Arnott and Southard (1990) (see Fig. 1.2C). However, to date, there has been no attempt to compile laboratory results from various sources into a combined-flow phase diagram. This effort might not be possible until more studies of combine-flow bed forms are undertaken.

Experimental studies of combined-flow bed forms started in the 1960's (Harms 1969; Inman and Bowen 1963). Inman and Bowen (1963) simulated sediment transport on beaches and found that adding a unidirectional current of 2 cm/s optimized transport rates for oscillatory flows of 21 cm/s. In 1969, Harms published results of his extensive descriptive study of the morphology and hydraulic significance of experimentally generated current, wave, and combined-flow ripples. To this day, this study remains the only one to provide detailed descriptions and diagnostic criteria for all three types of ripples (unidirectional-flow, oscillatory-flow, and combined-flow ripples). Then, it was not until the 1990's that more interest was devoted to combined flows in the laboratory. Arnott and Southard (1990) continued the work of Southard et al. (1990) on long-period oscillatory flows by fitting the oscillatory-flow tunnel with a recirculating pump enabling the generation of combined-flow conditions. They found that superimposing a unidirectional current of only a few cm/s to intermediate-velocity oscillatory flows was sufficient to make large-scale 3D bed forms asymmetrical. This, in turn, suggested that

stratification showing no strongly preferred dip direction must be generated by almost purely oscillatory flow. In addition, their experimental results showed that the addition of a weak (a few cm/s) unidirectional current to high oscillatory flows transformed oscillatory-flow large-scale bed forms into a plane bed. Consequently, they argued that plane bed should be more common under combined-flow than under oscillatory-flow conditions where large-scale ripples would persist up to higher flow velocities. In 1995, Yokokawa published the most comprehensive study to date on small-scale combined-flow ripples formed under short oscillation periods. She reported that oscillatory and combined-flow ripples could be differentiated from unidirectional-flow ripples based on symmetry and high roundness (as defined by the roundness index). The 1990's also saw the start of the physical modeling of combined flows where current and waves are at an angle to each other (as opposed to being colinear) (Khelifa and Ouellet 2000; Lee Young and Sleath 1990; Van Rijn and Havinga 1995). Such studies are needed to define empirical properties between ripple geometry and flow conditions under the more complex case where current and wave combine at an angle other than zero or 180°. The findings of these technical studies have yet to be applied to the investigation of geological problems. In addition to the physical modeling of multidirectional wave-current flows, future experimental work will probably be able to better approximate natural conditions with the design of more sophisticated flumes and tunnels. For example, such devices could make possible the aggradation of a storm bed, while adjusting the oscillation period, flow velocities, and flow directions to match conditions measured during continental shelf storms. Details of experimental combined-flow studies are presented in Table 1.1.

Sediment transport on shorefaces and inner shelves - In parallel with the experimental work, oceanographers and geologists devoted much attention to the study

of sediment transport on modern shorefaces and inner shelves. In 1963, Bagnold proposed the concept of autosuspension, which in turn made possible the occurrence of turbidity currents on shallow dipping continental shelves. Soon after, Hayes (1967) studied the distribution of seafloor sediment after Hurricane Carla, one of the worst on record. Based on the graded nature of the beds and the relationship between bed thickness and bottom topography, he suggested that storm surge ebb currents catastrophically drained from back-barrier lagoons and developed into turbidity currents capable of transporting sand seaward onto the shelf for at least 15 km. Based on geological evidence, and particularly on a sedimentary structure called hummocky cross-stratification (HCS) (see Fig. 1.3A), Walker (1979) used the turbidity current idea to develop a model for shallow marine storm sedimentation. Some argued against the idea, namely Morton (1981) who preferred a wind-forced downwelling current explanation to the graded beds deposited by Hurricane Carla. Later, Swift and Figueiredo (1983) also argued against the possibility of autosuspension on the inner shelf based on the insufficient sediment concentration measured during a storm on the Long Island shoreface. The controversy continued as Wright (1987) suggested that much seaward sediment transport takes place in gravity-induced hyperpycnal plumes on shorefaces where high concentrations of fine sand and silt are frequently or continuously suspended by waves or strong currents. More recently, Myrow et al. (2002) invoked the hyperpycnal-plume model in their study of Cambrian shelf deposits and referred to the transport mechanism as wave-modified turbidity current. They postulated that high-density oceanic floods, originating from the sharp relief of the tectonically active hinterland adjacent to the shoreline, could trigger the sediment gravity flows responsible the emplacement of the tempestite beds observed. The debate about the potential existence of turbidity currents on inner continental shelves will most likely continue for quite some time.

Since the inferred mechanism of sediment transport is intimately related to the direction of transport, part of the debate lies on observed evidence of transport direction. For example, geologists infer shore-normal, flow direction that they attribute to shelf turbidity currents based on observed shore-perpendicular sole marks on the base of shallow-marine storm beds (e.g., Higgs 1990; Walker et al. 1983) (see Fig. 1.4A). In contrast, oceanographers measure shore-parallel flow direction that they attribute to the balance between a pressure-driven, shore-normal downwelling current resulting from coastal set-up during a storm, and the flow-deflecting Coriolis effect (Snedden et al. 1988; Swift and Figueiredo 1983) (see Fig. 1.4B). In an attempt to reconcile these conflicting views, Myrow and Southard (1996) proposed a unifying model whereby shallow-marine storm beds were deposited by turbidity currents, geostrophic currents, wave oscillations or any combination of the three. Their model presents the various sedimentologic features of the storm beds associated with each of the generating flow mechanisms and combinations of flow mechanisms. Table 3.1 (see Chapter 3) presents examples of flow and sedimentation conditions as measured on modern continental shelves.

Stratification - Bed forms are rarely preserved in the rock record. For this reason, geologists commonly base their interpretations of depositional environments on the more readily preserved internal stratification produced by migrating and aggrading bed forms. Conceptual models of wave-influenced sedimentary structures have been developed to provide a basis for interpreting the shallow marine rock record. In 1971, Clifton at al. proposed such a model for wave-generated sedimentary structures and sequences on non-barred shorefaces. Soon after, Davidson-Arnott and Greenwood (1976) extended the model to barred shorefaces. Another frequently referenced model is the one by De

Raaf et al. (1977), which defined and illustrated diagnostic structural features of small-scale wave ripple stratification (see their Fig. 8).

Of special interest to sedimentologists is hummocky cross-stratification, a large-scale sedimentary structure thought to indicate deposition in shallow-marine environments during storm conditions. HCS was first described by Campbell (1966) who referred to the structure as truncated wave-ripple laminae. Later, Harms et al. (1975) introduced the term HCS to describe gently dipping (< 15°) cross-stratification characterized by the presence of both hummocks and swales (meter-spacing, decimeters high) found in coarse silt to fine sand (see Fig. 1.3A). Based on the sharp basal contact, the mantling relationship between the laminae and the lower set boundary, and the association with wave ripples, HCS was postulated to be generated by large storm waves of a rough sea (Harms et al. 1975). Following the official introduction of hummocky cross-stratification in the geological literature, there were numerous reports of HCS in the rock record, but at the same time, raging debates about its origin (e.g., Dott and Bourgeois 1982; Duke 1986; Greenwood and Sherman 1986; Leckie and Krystinik 1989; Nottvedt and Kreisa 1987). For example, there were disagreements on the type and origin of the formative flow (oscillatory flow, unidirectional flow, or combined flow), and the precise mechanism under which HCS formed (scour and drape structure vs. actively growing bed form). In 1993, Cheel and Leckie published a summary of the issues surrounding the enigmatic HCS. In the same period, a morphologically similar large-scale sedimentary structure was defined: swaley cross-stratification (SCS) (Leckie and Walker 1982) (see Fig. 1.3B). As HCS, swaley cross-stratification consists of meter-scale, gently undulating sub-parallel shallow-dipping laminae, but has a much higher prevalence of swales (only ~ 5% hummocks). Because of the morphologic similarities between SCS and HCS, the two sedimentary structures are thought to be genetically related and debates about their origin revolve around the

same issues. Beyond their similarities, there are differences. For example, SCS is generally found in coarser sediment than HCS (up to coarse sand), and deposits containing SCS are frequently amalgamated and show evidence of reworking by fairweather conditions. For these reasons, SCS is thought to represent more proximal settings than HCS. In shoaling upward sections of the stratigraphic record, SCS is generally assigned to the upper shoreface (above fairweather wave base), while HCS, which occurs stratigraphically below SCS, is generally assigned to inner shelf to lower shoreface (above storm wave base) (Arnott 1992; Duke 1985; Plint and Walker 1987; Tillman 1986) (see Fig. 1.5). Further discussion of the morphology and origin of HCS and SCS is provided in Chapter 3.

THESIS ORGANIZATION

The thesis consists of four chapters, of which two are self contained chapters written in a paper format. Chapter two is the core of the thesis and presents a detailed account of the experimental results. Chapter three focuses on the characteristics of the stratification generated by large-scale oscillatory-flow-dominant bed forms and discusses the effects of aggradation rate and unidirectional flow. The final chapter summarizes the principal conclusions of the study.

Fig. 1.1 Velocity gradient, boundary layer, and shear stress. Thin near-bottom wave-current (combined-flow) boundary layer is associated with a steep velocity gradient and high boundary shear stress. Immediately above the combined-flow boundary layer, the thicker current (unidirectional-flow) boundary layer is associated with shallower velocity gradient and lower shear stress (modified from Vincent 1986).

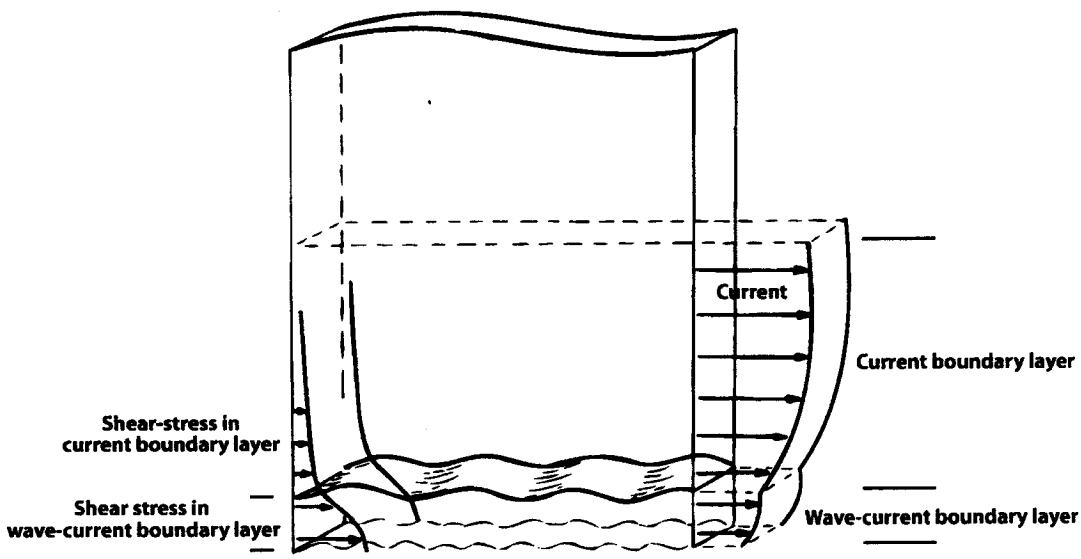
Current
Current boundary layer
Shear-stress in
current boundary layer
Shear stress in
wave-current boundary layer
Wave-current boundary layer

Fig. 1.2 Bed phase diagrams. **A.** Unidirectional flow phase diagram synthesizing flume data (Southard and Boguchwal 1990). **B.** Oscillatory flow phase diagram compiled from multiple source experimental data (Harms et al. 1982). **C.** Combined-flow phase diagram (where grain size is 0.09 mm, and oscillation period is 8.5 s), slightly modified from the exploratory experimental work of Arnott and Southard (1990, in Myrow and Southard 1990).

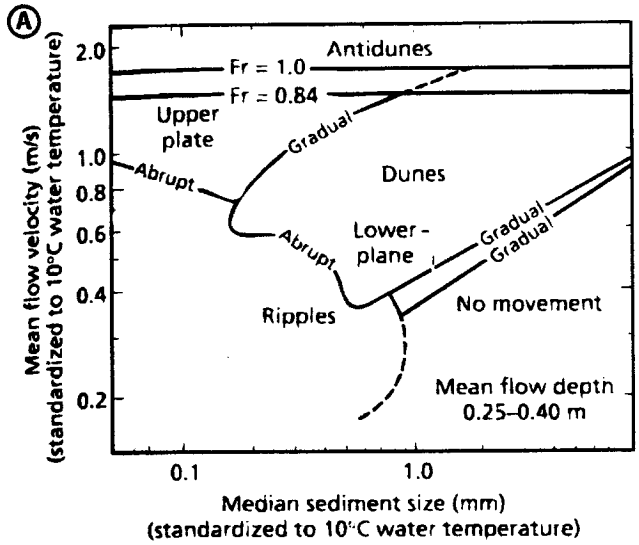
A
Antidunes
Fr = 1.0
Fr = 0.84
Upper plate
Gradual
Abrupt
Dunes
Lower-plane
Abrupt
Gradual
Gradual
Ripples
No movement
Mean flow depth 0.25–0.40 m
Mean flow velocity (m/s) (standardized to 10°C water temperature)
2.0
1.0
0.8
0.6
0.4
0.2
0.1
1.0
Median sediment size (mm) (standardized to 10°C water temperature)

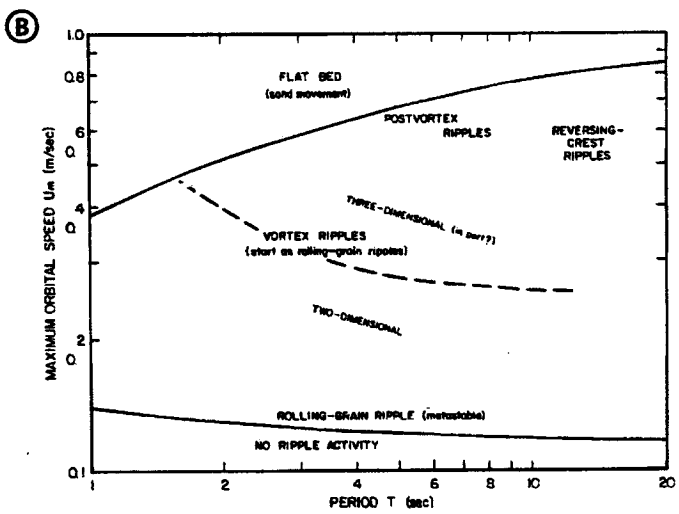
B
FLAT BED
(sand movement)
POSTVORTEX RIPPLES
REVERSING-CREST RIPPLES
VORTEX RIPPLES
(start as rolling-grain ripples)
ROLLING-GRAIN RIPPLE (metastable)
NO RIPPLE ACTIVITY
MAXIMUM ORBITAL SPEED Um (m/sec)
PERIOD T (sec)
1.0
0.8
0.1
1
2
4
6
8
10
20

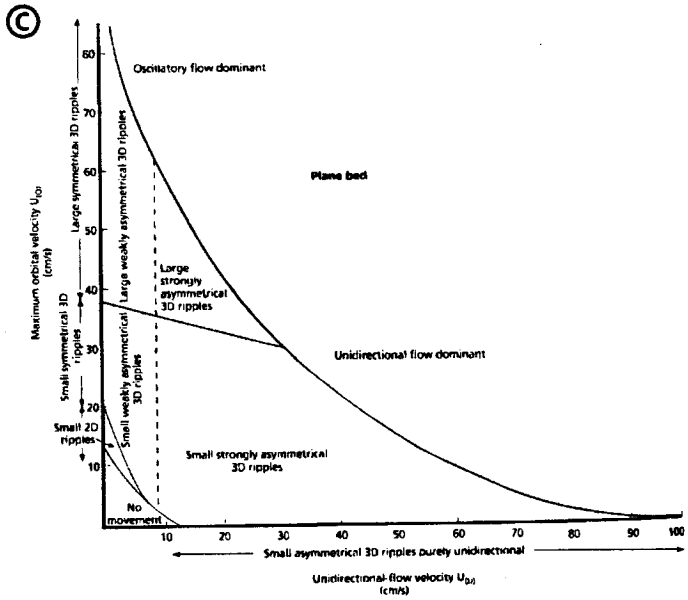
C
Oscillatory flow dominant
Plane bed
Large strongly asymmetrical 3D ripples
Unidirectional flow dominant
Small strongly asymmetrical 3D ripples
No movement
Small 2D ripples
Small symmetrical 3D ripples
Large symmetrical 3D ripples
Small weakly asymmetrical 3D ripples
Large weakly asymmetrical 3D ripples
Maximum orbital velocity Uo (cm/s)
10
20
30
40
50
60
70
80
90
100
Small asymmetrical 3D ripples purely unidirectional
Unidirectional flow velocity U0 (cm/s)

Fig. 1.3 Original block diagrams illustrating the plan and cross-sectional morphology of hummocky cross-stratification. **A.** Hummocky cross-stratification (Harms et al. 1975). **B.** Swaley cross-stratification (Leckie and Walker 1982).

(A) Hummocky cross-stratification

Found in silt to fine sand sized sediment
Occurs as sharp-based sandstones
alternating with shales and musdtones,
or as amalgamated sandstone bodies
Deposits have thicknesses of up to several meters

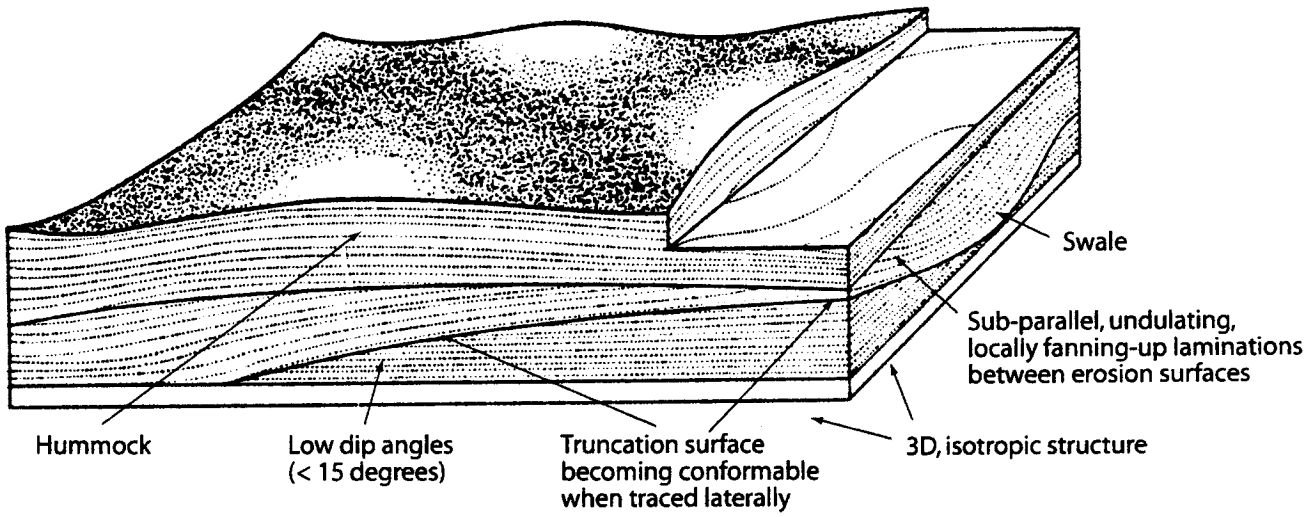

(B) Swaley cross-stratification

Found in sand sized sediment
Occurs as amalgamated sandstone bodies
Deposits have thickness of up to several meters

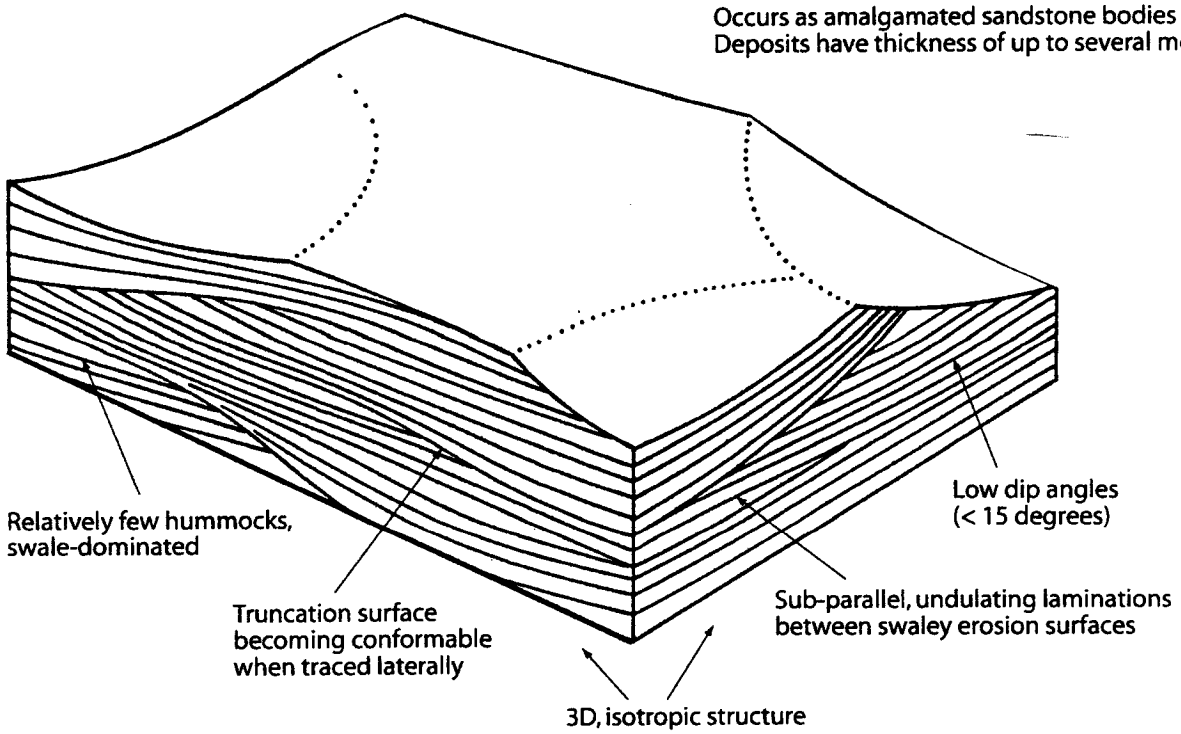

Fig. 1.4 Direction of near-bottom flows. **A.** The geological perspective – during major storms, shore-perpendicular bottom flows are generated by storm surge initiated turbidity currents (Walker 1979). **B.** The oceanographic perspective – shore-oblique flow that results from the balance of the downwelling pressure force, Coriolis force, and friction force (Swift et al. 1986).

(A) Shore-normal bottom flows - the geological perspective

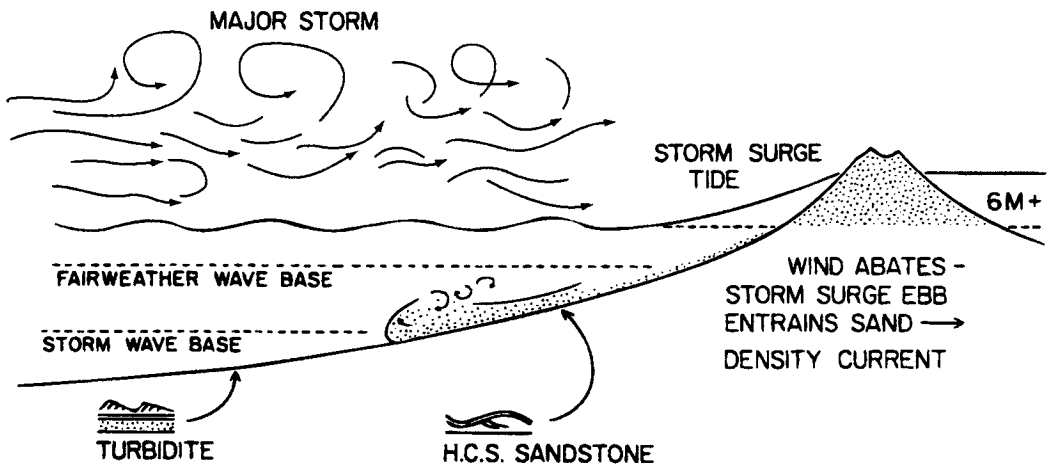

(B) Shore-parallel bottom flows - the oceanographic perspective

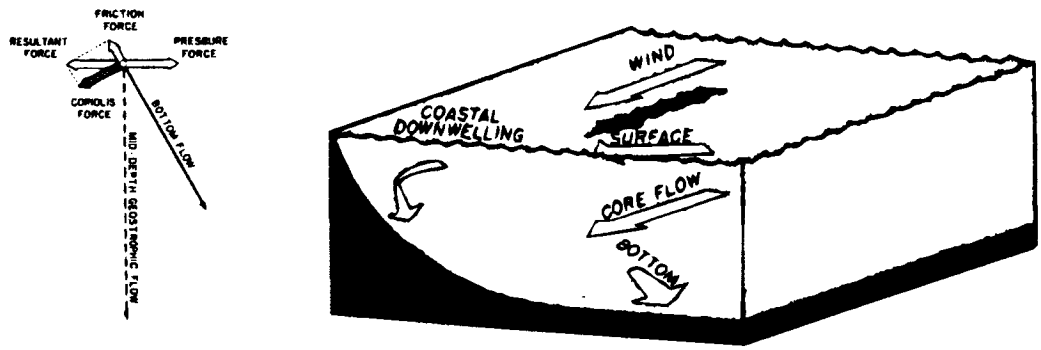

Fig. 1.5 Stratigraphic relationship of HCS and SCS. Stratigraphic section of a wave-dominated, progradational (shallowing upward), shallow-marine succession. HCS occurs on the lower shoreface, above mudstones of the outer shelf. SCS overlies HCS and underlies beach and breaker zone sandy deposits (modified from Walker and Plint 1992).

Coastal plain

Coal / Backshore

Beach

Breaker zone - ridge and runnel / rip channels

Shoreface - ***Swaley cross-stratification***

Lower shoreface - inner shelf transition - ***Hummocky cross-stratification***

Mid-shelf-bioturbated Sandy siltstone

Outer shelf-bioturbated Mudstone

Table 1.1 Summary of experimental studies on oscillatory and combined flows

N/A: does not apply
-: information not provided
↗: increase
↘: decrease
^{Ts} : small wave tunnel
^{TL} : large wave tunnel
vfsa: very fine sand
fsa: fine sand
msa: medium sand
csa: coarse sand
U_0: oscillatory velocity
U_u: unidirectional velocity
U_c: velocity of the combined oscillatory and unidirectional flows
d_0: orbital diameter of the flow
T: oscillation period
λ: ripple wavelength
Height: ripple height
RI: ripple index; ripple wavelength/ripple height
SI: symmetry index; horizontal length of the stoss side/horizontal length of the lee side
RDI: roundness index; length of stoss side at half the bed form height/full horizontal length of stoss side

Table 1A. Summary of experimental studies on oscillatory and combined flows – *Apparatus*

Date	Author	Type	Wave mech.	Length (m)	Width (m)	Height (m)	Ratio Sand thick. /Depth	Location and focus of study
COMBINED FLOW EXPERIMENTS								
2002	Dumas, Arnott, and Southard	wave tunnel	pistons (2)	15	1.2	0.65	0.31	MIT., USA. Long period U_0 and U_c bed forms plotted on U_0 vs U_u graphs. Verify the effect of oscillation period and grain size
2001	Paphitis, Velegrakis, et al.	flume	oscil. tray	2.7	0.27	0.25	-	University of Southhampton, UK. Sediment movement threshold
2000	Khelifa and Ouellet	flume (U_0 & U_u at ∠)	paddle	15 (flume) 5.7 (test section)	3.7	0.6	-	Université Laval, Canada. Prediction of ripple wavelength and height from flow conditions (U_0, U_u)
1995	Yokokawa and Masuda	flume	piston	10	0.2	0.5	0.26	Osaka University, Japan. Small-scale U_c ripple dynamics
1995	Yokokawa	flume	piston	10	0.2	0.5	0.26	Osaka University, Japan. Develop dictinction criteria for U_c vs. U_0. vs. U_u small ripples
1995	Van Rijn and Havinga	flume (U_0 & U_u at ∠)	-	26.5	4.0	-	-	Delft University, Netherlands. Sediment concentrations and transport rates
1993	Van Rijn and Nieuwjaar, et al.	flume	-	45	0.8	1	0.2	Delft University, Netherlands. Sediment concentrations and transport rates
1991	Murray and Davies	wave tunnel	piston (1)	9	0.5	2.3	-	Marine Science Laboratories, Menai Bridge, UK. Combined flow boundary layer; sediment concentration
1991	Tanaka, Yoshitake, et al.	flume	-	18	0.3	0.5	0.13	Tohoku University, Japan. Sediment transport rates for different grain sizes; evolution of bed profile. basis for numerical model of grain sorting
1990	Arnott and Southard	wave tunnel	piston (1)	15	0.4	0.26	-	MIT., USA. Investigate long period U_0 and U_c bed forms; generate phase diagrams.
1990	Lee Young and Sleath	flume (⊥ U_0 & U_u)	oscil. tray	5 (flume) 0.7 (test section)	1.2 0.7	0.25 0.04	0.16	Cambridge University, UK. Try to develop model to predict ripple geometry as a function of flow parameters (serpentine ripples never described elsewhere)
1969	Harms	flume	fan	61	2.44	1.22	-	Colorado State University, USA. Thourough description and illustrations of U_0, U_u, and U_c ripples. Define diagnostic proprieties
1963	Inman and Bowen	flume	paddle	28.6	0.61	0.91	0.08	Hydraulic Research Station, UK. Sediment transport rates
OSCILLATORY FLOW EXPERIMENTS								
1990	Southard, Lambie, et al.	wave tunnel	piston (1)	6 (small tunnel)[TS] 15 (large tunnel)[TL]	0.1 0.4	0.25 0.26	0.40 0.38	MIT., USA. Investigate long period U_0 bed forms (shallow marine storm conditions). Understanding HCS
1980	Miller and Komar	flume	paddle	104	3.7	4.6	-	Oregon State University, USA. Comparison of various types of experimental devices. Define a relationship between ripple wavelength and orbital diameter
1980	Brebner	wave tunnel	piston (1)	15 (test section)	0.5	1	0.15	Queen's University, Canada. Ripple wavelength as a function of flow parameters
1979	Dingler	flume	paddle	44 (flume) 6 (test section)	2.4 0.5	2.4 1-1.18	0.05	Scripps Institution of Oceanography, USA. Sediment movement threshold and compare with Bagnold (1946)
1978	Lofquist	wave tunnel	pistons (2)	2.53	0.21	0.3	-	Coastal Engineering Research Center, USA. Sediment movement threshold; ripples geometry as a function of flow parameters
1975	Sleath	flume	oscil. tray	2.14 (flume) 1.22 (test section)	0.31	0.91	0.06	Cambridge University, UK. Relation between wavelength of rolling-grain ripples and wave characteristics
1969	Carstens, Neilson, et al.	wave tunnel	piston (1)	3.05 (test section) 1.83 (bed)	1.22 1.22	0.30 0.10	0.33	Coastal Engineering Research Center, USA. Study of large-scale U_0 bed forms in various grain sizes (movement thresholds, bed dynamics, equilibrium bed forms, energy dissipation over large ripples)
1965	Kennedy and Falcon	flume	paddle or piston	15.2	0.76	0.91	0.076	MIT, USA. Ripple geometry as a function of flow parameters; sediment transport rates
1965	McKee	flume	baffle paddle	13.7 4.6	-	> 0.13	-	US Geol. Survey. Effect of flow and sediment parameters on ripple morphology
1946	Bagnold	flume	oscil. tray	< 2	~ 0.5	~ 1	-	Imperial College, UK. sediment movement theshold; ripple morphology

Table 1B. Summary of experimental studies on oscillatory and combined flows - *Flow conditions*

Date	Author	*Fluid*	*Flow*					
		Temp. (° C)	U_0 (cm/s)	U_u (cm/s)	d_0 (cm)	T (sec)	Wave height (cm)	Water depth (cm)
COMBINED FLOW EXPERIMENTS								
2002	Dumas, Arnott, and Southard	6-30	20-125	0-25	50-420 (U_0) 60->500 (U_c)	7 and 9.4	N/A	65
2001	Paphitis, Velegrakis, et al.	10	0-28	0-24	< 200	5, 12, 15	-	-
2000	Khelifa and Ouellet	-	8-26	7-34 (at 60°,90°)	-	0.9-1.4	5-14	30
1995	Yokokawa and Masuda	-	7.7-17.9	16.1-19.2	-	0.65-1.25	-	-
1995	Yokokawa	-	0-30.6	0-44.4	-	0.65-1.25	-	-
1995	Van Rijn and Havinga	-	-	10-30 (at 60°,90°,120°)	-	2.5	7-14	40
1993	Van Rijn and Nieuwjaar, et al.	-	0-40	10-40	-	2.5	7.5-18	50
1991	Murray and Davies	-	40 110	20 40	≤ 230	10	N/A	230
1991	Tanaka, Yoshitake, et al.	-	-	25.1		1.85	11.2	29.3
1990	Arnott and Southard	-	0-80	0-25	-	8.5	N/A	26
1990	Lee Young and Sleath	-	0-38	- (at 90°)	≤ 19	0.5-6	-	25
1969	Harms	17	~ 0-25	~ 0-45	-	1.6, 3.1, 8.1	12	15-61
1963	Inman and Bowen	7-8 6-15	21 30	0, 2, 4, 6 0, 2, 4, 6	9.5 18.5	1.4 2.0	15 17	50
OSCILLATORY FLOW EXPERIMENTS								
1990	Southard, Lambie, et al.	10	10-98 [TS] 17-88 [TL]	0 0	20-360 [TS] - [TL]	3.1-19.3 [TS] 6.7-9.6 [TL]	N/A	25 [TS] 26 [TL]
1980	Miller and Komar	-	15.9-33.7	0	15.2-53.6	3-5	34.2-37.6	317
1980	Brebner	-	7.3-55.1	0	15-150	3-15	-	100
1979	Dingler	-	~ 6.7-20.7 (fsa)	0	4.2-65.7 (fsa)	2-10 (fsa)	-	100-118 (fsa)
1978	Lofquist	21.2	17.7-77.0	0	18.3-91.6	1.6-16.0	N/A	29.8
1975	Sleath	12.4-14.3	17.96-71.8	0	4-40	0.54-3.55	-	50
1969	Carstens, Neilson, et al.	17.2-27.2	9.0-55.7 (fsa)	0	10.2-62.7 (fsa)	3.6	9.1-91.8 (theoretical)	30
1965	Kennedy and Falcon	15.6-23.9	2.4-42.1 12.2-17.4 (vfsa)	0 0	0.76-25.6 2.0-5.9 (vfsa)	1.07-2.95 1.07-2.34 (vfsa)	1.7-8.6	35.7-61.0
1965	McKee	-	-	0	-	-	-	10-13
1946	Bagnold	-	0-65 rad/s	0	<2-64	6.8	-	-

Table 1C. Summary of experimental studies on oscillatory and combined flows - *Bed and bed forms*

Date	Author	*Sand*			*Bed form*								
		Size	Mean/med (mm)	Specific gravity	Name	Size	d_0/λ	λ (cm)	Height (cm)	RI	SI	RDI	Lee dip (°)
COMBINED FLOW EXPERIMENTS													
2002	Dumas, Arnott, and Southard	vfsa fsa	0.11 0.17	2.65	ripples (2,3D) ripples (2,3D) hummocky bed plane bed	small large	15 (T=9.4), 8 (T=7) 1-2 1-2 N/A	6-18 90- >300 100-250 N/A	0.5-1.5 8-30 8-15 N/A	~ 8-10 ~ 10-12 10-25(vfsa), 9(fsa) N/A	1.2-1.6 1.0-5.1 1.2-2.0 N/A	0.5-0.8 0.4-0.7 0.6-0.9 N/A	12-25 15-30 5-25 N/A
2001	Paphitis, Velegrakis, et al.	msa-csa	0.315-0.513	2.65	- (mvt. thresh.)	-	-	-	-	-	-	-	-
2000	Khelifa and Ouellet	fsa msa	0.15 0.5	2.65	vortex ripples vortex ripples (U_0 & U_u at $\angle$)	small small	- -	2.9-4.1 3.5-12.1	0.55-0.81 0.37-1.66	4.68-6.11 5.91-11.78	-	-	-
1995	Yokokawa and Masuda	fsa	0.18	2.65	ripples	small	-	6	0.8	7.5	-	-	-
1995	Yokokawa	csilt fsa msa	0.06 0.18 0.29	2.65	ripples (U_u<19) ripples (U_u>19)	small small	-	~ 5 ~ 5-10	~ 1 ~ 1	~ 6 [5.4-6.8] ~ 6 [4.9-7.9]	1-1.3 1-3	< 0.45 > 0.54	-
1995	Van Rijn and Havinga	vfsa	0.1	2.65	ripples (U_0 & U_u at $\angle$)	small	-	8.2	0.9	9.1	0.85-1.6	-	-
1993	Van Rijn and Nieuwjaar, et al.	vfsa fsa	0.1 0.2	2.65	ripples ripples	small small	-	8.0 12.2	1.1 1.8	7.3 6.8	-	-	-
1991	Murray and Davies	vfsa	0.124	2.65	ripples (U_0=110) plane bed (U_u=40 + U_0=110)	-	orbital (U_0=110) N/A	- N/A	- N/A	- N/A	- N/A	- N/A	- N/A
1991	Tanaka, Yoshitake, et al.	csa msa-pebl	1.75 0.25-5	2.65	- (mvt. thresh.)	-	-	-	-	-	-	-	-
1990	Arnott and Southard	vfa	0.09	2.65	ripples (2,3D) ripples (3D) hummocky bed plane bed	small large large	sub-orbital orbital orbital (?)	5-15 (?) ~10's- >200 ~ 80-150	~ < 5 (small) ↗ to > 10, and then ↘ (large)	~ 8-10 variable ~ 15-20	-	-	-
1990	Lee Young and Sleath	fsa msa csa vcsa	0.203 0.445 0.700 1.065	2.65	serpentine ripples ($\perp$ U_0 & U_u)	-	-	7.5-25 λ // to U_u ($\perp$ to U_0)	-	-	-	-	-
1969	Harms	msa	0.28	2.65	oscillatory ripples combined ripples		orbital	0.2- >200 10-25	1/6λ (<0.1-40) 20-45	6-10 > 25	-	-	≤ 25 25-repose
1963	Inman and Bowen	fsa	0.2	2.65	ripples	small	~ 1.5 (T=1.4) ~ 1.8 (T=2.0)	~ 6.5 ~ 10.5	1.0 1.5	6.5 7	1.18 1.31	-	-
OSCILLATORY FLOW EXPERIMENTS													
1990	Southard, Lambie, et al.	fsa msa vfsa	0.18 ^{TS} 0.30 ^{TS} 0.11 ^{TL}	2.65	ripples (2,3D) ripples (3D)	small large	suborbital ^{TS} 2.6-3.9 ^{TL}	12-196 (small) 0.5-3 ^{TL}	2.2-23.9 ^{TS} ↗ to 20, ^{TL} then ↘	1.59-20.0 ^{TS} - ^{TL}	-	-	-
1980	Miller and Komar	fsa	0.168	2.65	roling grain & vortex ripples		1.54-5.10	6.0-13.5	1.0	> 10 (roll.-grain) ~ 6.66 (vortex)	-	-	-
1980	Brebner	vfsa fsa	0.1 0.2	2.65	ripples	-	1.5-25 1.5-50	-	-	≥ 7.14	-	-	30
1979	Dingler	fsa-vcsa	0.18-1.45	2.65	- (mvt. thresh.)	-	-	-	-	-	-	-	-
1978	Lofquist	fsa fsa csa	0.18 0.21 0.55	2.65	rolling grain vortex ripples (2D,3D)	small small & large	1.56-24.10 1.54-2.22 1.18-1.84	3.8-26.8 11.4-33.2 16.9-72.5	1.56-3.67 1.60-4.38 2.83-15.5	~7.5 - -	-	-	-
1975	Sleath	msa csa	0.404 1.14	2.65	rolling grain ripples	small	1.6-5.9 (msa) 1.9-3.4 (csa)	2.20-10.23 (msa) 9.33-16.75 (csa)	-	high (>10)	-	-	-
1969	Carstens, Neilson, et al.	fsa msa csa	0.190 0.297 0.585	2.66 2.47 2.62	ripples & dunes		1.6-6.3 (fsa dunes)	10.0-15.2 (fsa dunes)	0.48-2.45 (fsa dunes)	5.0-20.8	-	-	-
1965	Kennedy and Falcon	vfsa vfsa msa csa	0.095 0.107 0.32 1.00	2.67 1.35 2.67 1.035	ripples		0.7-1.2 (vfsa)	3.0-5.6 (vfsa) 1.7-8.6 (all)	0.3-0.6 (vfsa) 0.05-5.2 (all)	9.3-12 (vfsa)	-	-	-
1965	McKee	fsa csa	- -	2.65	ripples	small	-	11.2 (fsa) 18.4 (csa)	1.6 (fsa) 2.3 (csa)	7 (fsa) 8 (csa)	-	-	24.7 (fsa) 26.0 (csa)
1946	Bagnold	vfsa fsa csa	0.09 0.16 0.6, 0.8	2.65	rolling grain & vortex ripples	small	-	1.5-18	(0.33-6) inferred	4.5-8	-	-	-

CHAPTER 2

EXPERIMENTAL INVESTIGATION OF EQUILIBRIUM OSCILLATORY- AND COMBINED-FLOW BED FORMS

INTRODUCTION

In general, combined flow designates the combination of two or more types of flow in space and time. However, most commonly it is used to indicate a combination of oscillatory and unidirectional flow. Even within this limited definition numerous possibilities exist, since any of the following unidirectional flows (tidal currents, fluvial currents, rip currents, geostrophic flows, downwelling flows, gravity flows) and oscillatory flows (fairweather or storm wind waves, swell waves, internal waves) can interact and form a combined flow. Sedimentary environments where combined flows occur are diverse and include: tidal flat, estuary, delta front, beach, lake, shoreface, shelf, open ocean, etc. It follows that shallow and marginal marine settings and, accordingly, much of the stratigraphic record, is influenced by combined flow, especially because a combined wave-current flow transports sediment more efficiently than the sum of its parts (Grant and Madsen 1979; Li and Heffler 2002; Murray et al. 1991). Despite this, our understanding of combined-flow bed forms is currently rather limited. In particular, due to logistical challenges on modern continental shelves and the need for prohibitively large laboratory flumes, the effect of long-period, high oscillatory-flow waves is still very poorly understood. These conditions, however, are attained during high-energy storms on continental shelves, and it is under these extreme conditions that sand is thought to be transported basinward from the coast, generating bedload transport in a setting that

is otherwise characterized by suspension fallout (e.g., Grant and Madsen 1986; Li and Heffler 2002; Sherwood et al. 1994; Trowbridge and Nowell 1994; Wright et al. 1994). In addition, hummocky cross-stratification is interpreted to be formed during high-energy storms (e.g., Arnott and Southard 1990; Cheel and Leckie 1993; Dott and Bourgeois 1982; Duke 1985; Harms et al. 1975; Southard et al. 1990; Walker et al. 1983). This paper presents the results of wave-tunnel experiments on long-period oscillatory- and combined-flow equilibrium bed forms. In particular, it outlines the formative conditions and stratal characteristics of these bed forms, which in turn will form a basis for interpreting parts of the storm-dominated stratigraphic record.

EXPERIMENTAL APPARATUS AND METHODS

Experiments were made in a combined-flow tunnel 15 m long with a cross section 1.20 m wide by 0.65 m deep (Fig. 2.1). The flow was fully enclosed, with no free surface. The body of the combined-flow tunnel was constructed of polypropylene supported by an external steel frame. The central 5 m of the tunnel housed removable lids that allowed access to the bed and transparent windows on both sides for continuous monitoring of bed and flow conditions. Oscillatory flow was produced by the simple harmonic motion of drive arms translating into the up-and-down movement of two coupled, loose-fitting vertical pistons at either end of the U-shaped tunnel. A slurry pump integrated into a closed recirculating loop provided the unidirectional component of the flow. The oscillatory and unidirectional flows could either be generated independently or superimposed colinearly. The study investigated bed forms produced over a wide range of oscillatory and unidirectional velocities using two different grain sizes (0.11 and 0.17 mm; unscaled variables), and two wave periods (9.4 and 7 s; unscaled variables). The average thickness of the sediment bed was about 0.11 m which reduced the mean flow depth to about 0.54 m. All runs were non-aggrading.

Flow velocities were measured with an acoustic Doppler velocimeter (ADV) probe inserted near the center of the tunnel. Velocities could be sampled at various depths simply by moving the ADV up and down along a vertical axis. The oscillation period was obtained by timing the cyclic harmonic motion of the drive mechanism, which corresponded well with the period observed in the oscillatory flow record measured by the ADV probe. Water temperature was measured throughout each run and was used to scale flow parameters following the method outlined in Southard et al. (1990). Scaling equations are detailed in Appendix B. Orbital diameter was determined by physically measuring the horizontal excursion of neutrally buoyant particles during a full oscillation.

Data for this study consist of 18 series of experiments each comprising several runs (totaling 76) (Table 2.1). In addition, there were ten runs which were performed by a different operator. To insure consistency in the quantitative description of ripples, these runs do not appear in Table 2.1 but velocity and qualitative bed-form data were integrated into the dataset (see Fig. 2.5). For a given wave period, the oscillatory velocity (U_0), which is limited by the geometry of the drive mechanism, could assume only six different values. The unidirectional velocity (U_u), in contrast, could be changed continuously by adjusting a gate valve. An experimental series comprised a preselected oscillatory period and velocity onto which a progressively higher U_u, ranging from 0 to 25 cm/s, was superimposed; each combination of oscillatory and unidirectional velocity formed a run. This experimental strategy was repeated twice: first with the shorter wave period and then with the coarser sediment.

During each run, the morphological evolution and migration rates of the bed forms were monitored through sidewall markings, measurements, photos, and video. Equilibrium between the bed and the flow was assumed to be reached when the bed configuration remained unchanged for at least a few hours. The run was then stopped and the bed was sketched, measured, photographed, and filmed. Even though the bed did not aggrade, stratification patterns and bed evolution were approximated by drawing sidewall profiles of the bed surface at 5 min intervals (Southard et al. 1990).

Although the experiments were conducted using an apparatus similar to that of Arnott and Southard (1990), several important design modifications were made. One major improvement was the use of the ADV probe, which provided more accurate measurements of flow velocity. Also, the combined-flow tunnel had a larger cross-sectional area (increased by a factor of 8), which allowed better development of large three-dimensional bed forms, and two oscillatory-flow pistons instead of one, to improve the symmetry of the oscillatory flow. The apparatus used is the largest of its kind to date.

Also, because high oscillatory velocities could be generated, the transition between combined-flow ripples and combined-flow plane bed was able to be explored experimentally for the first time.

TERMINOLOGY

Over the past several years a large number of terms have been used to describe oscillatory-flow and combined-flow bed forms. Previous terminology is mostly genetic, as opposed to descriptive, and is therefore not readily applicable to description of the stratigraphic record. For example the definitions of rolling-grain ripples, a series of parallel rows a few grain diameters high developing at oscillatory velocities just beyond conditions of movement threshold, and vortex ripples, for which vortices induced by flow separation sweep across from trough to crest every half cycle, have genetic implications (Bagnold, 1946). Other examples of genetic terms are post-vortex ripples, flattened vortex ripples, which occur prior to the transition to plane bed, and reversing-crest ripples, generated under long oscillation periods (Harms, 1982; Clifton, 1984). The classification of combined-flow bed forms into current-dominated or wave-dominated also carries genetic implications (Harms, 1969; Yokokawa, 1995). On the basis of the above genetic definitions all ripples generated in the present experiments were vortex ripples (no rolling-grain, post-vortex, or reversing-crest ripples were observed). However, in this paper, a more descriptive terminology is favoured and the term "ripple" is chosen to represent all positive topographic elements (bed forms). The term "dune" is not used to describe large-scale bed forms since we do not believe that the bed forms generated scaled to flow depth as is the case for unidirectional flow dunes (Bridge 2003). Ripples

are then classified on the basis of size (small, wavelength (λ) < 20 cm vs. large, λ > 100 cm), and symmetry (symmetric vs. asymmetric).

A variety of ratios are used to further define ripple morphology (Fig. 2.2). The ripple index (RI), defined as the ratio of the bed-form wavelength to height, gives an indication of the vertical relief of the ripple (higher RI values denote flatter profiles) (Allen 1984). The symmetry index (*SI*), the ratio of the horizontal length of the stoss versus the lee sides, quantifies the degree of asymmetry (Allen 1984). *SI* of ~ 1 represents symmetrical bed forms whereas indices > 1 indicate progressively more asymmetrical bed forms. The roundness index (*RDI*), defined as the ratio of the length of the stoss side at half the bed form height to the full-horizontal length of the stoss side, expresses the degree of convexity of the stoss side of the ripple (Yokokawa 1995). *RDI* can range from 0.866 (arc of a circle), to 0.5 (straight), to near zero (highly concave). All of these indices are useful indicators that can be used in an attempt to determine ripple-generating flow conditions.

RESULTS

Phase Diagrams

Existence fields of the various bed forms produced are shown in Figures 2.3, 2.4, and 2.5. Bed-form data are plotted on phase diagrams of oscillatory velocity versus unidirectional velocity for the two grain sizes (0.14 and 0.22 mm; scaled to 10°C) and two oscillation periods (8.0 and 10.5 s; scaled to 10°C). Phase boundaries represent the simplest division (generally straight lines) between the different bed phases and do not necessarily imply any hydrodynamic significance. Also, with the exception of the transition from purely oscillatory small-scale to large-scale ripples and the flattening to

plane bed, all transitions between bed phases appear to be gradational. Additional work is needed to explore more fully the shape and dynamical significance of these boundaries. Below are descriptions of the various bed phases.

"No Movement"

The initiation of sediment motion was not an objective of this study, and therefore the no-movement field in the phase diagrams were simply determined by fitting a straight line between movement threshold velocities for purely oscillatory and purely unidirectional flow. Sediment movement threshold conditions for pure oscillatory flow were estimated from data presented in Komar and Miller (1975, their Fig. 7), whereas for purely unidirectional flow, movement threshold was determined by gradually increasing the unidirectional velocity until generalized bed-load movement was attained (spacial and temporal).

Symmetric Small Ripple (SSR)

Symmetric small ripples form under U_0 between the sediment movement threshold velocity and ~ 40 cm/s with a superimposed *Uu* of up to 10 cm/s (Fig. 2.6A). Ripple spacing varies between 7 and 11 cm but averages ~ 9 cm and increases with increasing U_u. Ripple height ranges from 0.5 to 1.3 cm but is typically around 1.0 cm and also shows a slight increase with higher U_u. SSR are characterized by narrow, sharp (well defined) crests, broad, rounded troughs, straight stoss and lee sides, and a symmetrical profile. In planform, crestlines are continuous and oriented perpendicular to the flow direction (across the tunnel). The bed configuration, therefore, is two-dimensional (2D).

Ripple index for SSR ranges between 6 and 14 and averages 10. The symmetry index is generally ~ 1 (symmetrical). Average dip of lee sides is 14°. Roundness index is most commonly about 0.4, suggesting a moderately concave stoss side.

Dynamically, conditions of pure U_0 and oscillation-dominated combined flow ($U_u \leq$ 10 cm/s) produce comparable flow-separation eddies during each half of the oscillatory orbital motion. This results in a symmetrical back-and-forth motion of a wedge of sediment about a mean crestal position and hence the maintenance of a symmetrical ripple profile. SSR bed forms can migrate both with and against the unidirectional flow at speeds of no more than a few centimeters per hour.

Asymmetric Small Ripple (ASR)

Under U_0 ranging from 0 to 40 cm/s but with higher U_u of 10-25 cm/s, symmetric small ripples become progressively more asymmetric (Fig. 2.6B; 2.6C). Ripple wavelength varies between 11 and 21 cm (average 13 cm) and height from 1.2 to 2.9 cm (average 1.8 cm). Both length and height increase with increasing U_u, but height eventually decreases when the plane bed boundary is neared. The asymmetric profile of ASR exhibits a wide crest area, and convex-up stoss and lee faces. In planform, crestlines are bifurcating and/or discontinuous, resulting in a 3D (three-dimensional) geometry.

RI are between 4 and 11 and average 8. ASR are moderately asymmetrical (*SI* ~ 1.5). Dip of lee sides varies from 11 to 27° but averages about 21°. Bed forms exhibit a rounded profile as indicated by a *RDI* of ~ 0.6.

Because of the higher U_u, the lee side (downstream) separation eddy is stronger. This asymmetry causes the lee face to be eroded more deeply and steeply, and in turn creates a more concentrated cloud of suspended sediment that is then deposited on the stoss side of the next ripple downstream. This results in an asymmetric biconvex ripple

profile (Fig. 2.7) and a net sediment transport in the direction of U_u. Migration speeds increase rapidly with increasing U_u and can reach over 200 cm/h near the phase boundary with asymmetric large ripple (Table 2.1, S6R5).

Symmetric large ripples (SLR)

Symmetric large ripples succeed SSR with increased oscillatory velocity (Fig. 2.8A). SLR are the dominant bed forms for U_0 between 40 and 100 cm/s and superimposed $U_u \leq 10$ cm/s. Bed-form wavelength varies between 111 and 224 cm (averaging 154 cm) and height between 6 and 27 cm (averaging 14 cm). Increase in either U_0 or U_u does not result in increased dimensions. In profile, SLR are symmetrical, have sharp and peaked crests corresponding to the brinkpoint, broad and round troughs, and approximately straight stoss sides. Planform geometry of SLR is almost invariably 2.5D (bed configuration is locally 2D and locally 3D) with discontinuous (not traceable across the combined-flow tunnel) and bifurcating crestlines. These large ripples are commonly covered with small superimposed ripples. The superimposed ripples have geometry similar to the small ripples described above (SSR or ASR) but have much larger ripple index (*RI* ~ 20, compared to *RI* ~ 10 for SSR and ASR), a consequence of their lower height. The superimposed ripples are better developed under lower U_0 and are washed out when U_0 conditions are near the plane bed boundary.

Symmetric large ripples vary widely in the degree of relief, as indicated by the broad range of *RI* 8-26 (average: 13). Low *SI* ranging from 1.0 to 1.9 (average: 1.3) confirms their symmetrical form. Lee sides dip moderately and vary from 5 to 23° (averaging 16°). Finally, *RDI* of 0.4-0.7 (averaging 0.5) indicate moderately rounded profiles.

Similarly to symmetric small ripples, the symmetry of SLR can be explained by the dominance of the symmetric oscillatory flow creating sub-equal sediment transport in

the downstream and upstream directions, in turn producing symmetric bed forms. SLR migrate both up and downstream at speeds of up to ~ 40 cm/h.

Asymmetric Large Ripples (ALR)

Asymmetric large ripples form when U_0 is in the range of 40-100 cm/s and U_u > 10 cm/s (Fig. 2.8D; 2.8E). These bed forms vary widely in wavelength 108-441 cm (186 cm on average) and height 9-40 cm (19 cm on average). There appears to be no correlation between ripple dimensions and velocity conditions. ALR profiles exhibit both sharp and diffuse crests, deep troughs, and round stoss sides. ALR planform geometry is variable and decreases from 2.5-3D to 2D (continuous crestlines) as U_u increases and the plane-bed boundary is approached. Similar to SLR, small ripples are superimposed on the large ripples and are washed out as U_0 conditions approach plane-bed conditions.

ALR ripple index varies from 7 to 19 (averaging 10). Asymmetry is high, with *SI* up to 9.0 (3.3 on average), with the highest asymmetry being produced under conditions of high U_u. Dips of lee sides are also high ranging from 11 to 31° but typically are near the angle of repose. Lastly, ALR have rounded profiles with *RDI* of ~ 0.6.

The asymmetry in the flow caused by the addition of a moderately strong current (Uu > 10 cm/s) generates unique features. As for ASR, the reattachment point of the separation eddy is displaced farther downstream as U_u increases. This, in turn, can create local ephemeral scours at the lower end of the stoss side. This results in a stoss side comprising two segments of unequal slope: a steeper lower section dipping ~ 10-15° followed downstream by a nearly horizontal section. In addition, with increasing U_u, the asymmetry of the profile increases further as the brinkpoint separates from the crest and migrates downstream. ALR generally migrate in the direction of the unidirectional current at speeds ~ 30-50 cm/h but up to 300 cm/h.

Reverse Large Ripples (RLR)

Reverse large ripples form under conditions of high U_0 (~ 80-120 cm/s) and moderate U_u (≤ 15 cm/s) but were observed only in runs with the coarser grain size (0.22 mm) and longer oscillation period (10.5 s) (Fig. 2.8B). The adjective "reverse" is used to indicate that the direction of migration is opposite to their sense of asymmetry. With wavelength ranging from 200 to > 500 cm and height of 30-40 cm, these were the largest bed forms produced in the experiments. Bed-form wavelength increases when U_0 and/or U_u are increased, but height increases only with higher U_0. RLR have an asymmetric profile with proportionally short and steep convex-up flanks, a long (~ 1/2 wavelength) and mostly horizontal crest area, and a diffuse brinkpoint typically located at a lower elevation downstream of the crest (along the steeper lee side). The RLR generated consistently have a 2D planform geometry, but this may be a limitation imposed by the relatively small dimensions of the combined-flow tunnel compared to the large size of the bed form. With an increase in U_0, RLR are replaced by plane bed. As U_u increases these bed forms evolve into asymmetric large ripples.

As mentioned above, reverse large ripples have an unusual migration direction with respect to their geometry: sediment is eroded on the short steep lee side and deposited along the longer, gently dipping stoss side. This atypical migration pattern is most easily explained in the context of the cyclical motion of the oscillatory component of the flow (Fig. 2.9). First, when U_0 is in the same direction as U_u, their effects combine to produce peak flow velocity creating a large flow-separation eddy, violent scouring, and a highly concentrated cloud of suspended sediment at the toe of the steep lee side. Then, as oscillatory flow stalls and reverses, eddying within the sediment cloud slows and the plume lifts. Next, when U_0 reverses and now opposes U_u, the sediment cloud is entrained upstream but its migration is impaired by the downstream unidirectional

current. Consequently, deposition occurs just upstream of the brinkpoint and all along the gently sloping stoss. It follows that RLR migrate upstream or against the unidirectional flow. As U_u reaches values of ~ 15 cm/s and higher, reverse large ripples gradually evolve into asymmetric large ripples (Fig. 9). The unidirectional velocity is now such that during the part of the cycle when U_0 and U_u are opposed it stalls the upstream progression of the sediment cloud, triggering deposition on the downstream side of the crest. This leads to a more conventional bed-form profile with erosion upstream of the crest and deposition downstream of it, straighter stoss and lee sides, a better definition of the brinkpoint, and a shorter lee side (Fig. 2.9). Also, bed-form migration is in the same direction as the unidirectional current.

Plane Bed (PL)

At oscillatory velocities of ~ 90-120 cm/s, but also for U_0 as low as ~ 60 cm/s when a $U_u \geq 20$ cm/s is added, bed forms are planed flat to form a plane bed. Commonly, this transition is attributed to high sediment concentration near the bed, which in turn suppresses turbulence and decreases the efficiency of the separation eddy (Bridge and Best 1988). Consequently, erosional faces decrease in height and steepness, and eventually, because the flow no longer separates, troughs are infilled, and the bed is planed flat. Hence, flatter (more subdued) bed profiles and more 2D planform are generally the incipient characteristics of the transition to plane bed.

Hummocky "Zone"

Under oscillatory flow velocities of ~ 50-90 cm/s and unidirectional flow velocities < ~ 15 cm/s, large-scale, broad-crested, 3D domal bed forms develop (Fig. 2.8C). These hummocky bed forms (HM) are similar in size to large symmetric and asymmetric ripples

and have wavelength of ~ 150-300 cm and height of ~ 10-25 cm. They can be distinguished from the other large-scale bed forms by their broad and rounded crests, which do not develop a sharply defined brinkpoint, their symmetric profile (vs. ALR), and their isolated 3D dome-like morphology. Ripple index is variable and ranges from 7 to 26 (average = 13). The degree of symmetry is between that of symmetric and asymmetric large ripples (average = 2.4). Lee sides exhibit a wide range of dip angles (~ 10-25°) and have maximum values between those of SLR and ALR. Roundness indices, which range from 0.4 to 0.9, reflect well the rounded nature of this bed form and generally peak in the hummocky zone. Because they are commonly observed at the transition between symmetric and asymmetric large ripples, HM exhibit variable migration direction (upflow and downflow) at speeds varying from ~ 10 cm/h to > 100 cm/h. Significantly, hummocky bed forms are stable under a wider velocity range with the longer (10.5 s) oscillation period.

At no time do hummocky bed forms populate the entire bed surface. Instead they coexist with other bed forms (mainly large-scale ripples), and as a result are not considered to be a separate bed state on the phase diagrams (Fig. 2.3, 2.4, and 2.5). Accordingly, they are depicted as a zone of hummocky bed forms superimposed on other bed phases. More precisely, hummocky bed forms appear near the phase transitions from SLR to ALR, from SLR to plane bed, and from SSR to SLR. For a given U_0 (in the 50-90 cm/s range) and progressively increasing Uu (from 0 to 25 cm/s) the bed configuration typically evolves through the following bed form assemblages: 1) SLR; 2) SLR + HM; 3) SLR + HM + ALR; 4) HM + ALR; and 5) ALR.

DISCUSSION

Phase Diagrams

Of the few experimental studies that have investigated long-period oscillatory or combined flows (e.g., Arnott and Southard 1990; Dingler 1979; Harms 1969; Lofquist 1978; Murray et al. 1991; Southard et al. 1990), the dataset that is the most comparable to our study is that of Arnott and Southard (1990), who used a similar combined-flow tunnel and similar oscillation period, flow velocities, and grain size. In general the two datasets are consistent, except for a few differences in terminology: 1) their small transitional ripples equate to the boundary between our 2D symmetric and 3D asymmetric small ripples; 2) their low-angle and high-angle large ripples are equivalent to our symmetric and asymmetric large ripples, respectively. Nevertheless, beyond these similarities, there are some notable differences. First, the boundary between small-scale and large-scale ripples is horizontal and is placed at lower U_0 (~ 40 cm/s) in Arnott and Southard's (1990) diagram. In our diagrams (Figs. 2.3-2.5), this boundary occurs at U_0 ~ 40-60 cm/s and slopes downward to the lower right, indicating that the addition of a current lowers the U_0 needed to generate large-scale ripples. Second, because we were able to generate plane bed under purely oscillatory flow, the phase boundary between large-scale ripples and plane bed is experimentally constrained instead of estimated. Third, our results show a change in the geometry of asymmetric large ripples from 3D to 2D near the plane-bed phase boundary, which was not reported by Arnott and Southard (1990). Fourth, we define a zone of hummocky bed forms that coexist with other equilibrium ripples, compared to Arnott and Southard (1990), who qualified their entire large ripple field as being hummocky.

Ripple Morphology

Understanding the relationship between bed-form morphology and flow conditions is key to interpreting modern and ancient depositional environments (Allen 1979; Clifton and Dingler 1984; Komar 1974). Many attributes can be used to describe the morphology of oscillatory-flow and combined-flow bed forms. Some of the most useful include: size (length, height, ratio of the two), symmetry, steepness of stoss and lee sides, roundness, shape of crestline, stoss side, and lee side, and planform geometry. Table 2.2 summarizes these morphological attributes for small-scale and large-scale oscillatory-flow and combined-flow bed forms.

Size - Unlike unidirectional ripples and dunes, there is currently no official classification for oscillatory-flow or combined-flow bed forms according to height (Ashley 1990). Our results show an abrupt jump in ripple size from small scale (λ > 20 cm) to large scale (λ > 1 m), with no intermediate-sized ripples. The dynamical reason for this is not yet understood but may analogous to the destruction of the viscous sublayer portion of the turbulent observed at the transition between ripples and dunes generated by a unidirectional flow. At the very least, this observation suggests that the formation of small versus large oscillatory-flow and combined-flow ripples is governed by a different coupling mechanism between the sediment and fluid flow.

The jump in size is particularly evident in the experiments using finer sand (0.14 mm) and longer period (10.5 s) for which the equilibrium oscillatory ripple wavelength increased from 6.5 to 160 cm with only a small increase in oscillatory velocity (56 to 61 cm/s) (Fig. 2.3). In the literature, wave-ripple size is commonly reported to form a continuum from small to large (e.g., Bucher 1919; Campbell 1966; Harms 1969; Lofquist 1978). However, recent experimental studies with equipment capable of generating larger bed forms (larger channels, higher U_0) do suggest a grouping of ripple wavelength

into two distinct populations (Clifton and Dingler 1984; Southard et al. 1990, their Fig. 11). Further research using different flow parameters and grain sizes is clearly needed.

Combined-flow ripples also show a distinct jump in size, but the increase in wavelength is more gradational than for oscillatory-flow ripples. A mixed population of small (centimeter-scale) and medium ripples (decimeter-scale) coexist near the transition to large-scale ripples, but transform rapidly to large ripples (meter-scale) with only a slight increase in oscillatory velocity. Arnott and Southard (1990) also observed two size populations. Similarly, on the modern Scotian shelf, an approximately 10-fold increase in ripple wavelength was observed between small-scale and large-scale wave-dominated combined-flow bed forms (Li and Amos 1999a). In contrast, in the rock record, a statistical analysis of wavelength of combined-flow bed forms from the Fernie Formation (Jurassic) reveals that combined-flow bed forms form a continuous size population with no jump in size between small-scale and large-scale ripples (Banerjee 1996).

Ripple index - Ripple index proved to be of limited use in differentiating between oscillatory-flow and combined-flow ripples. In this study, wave-ripple *RI* range between 6 and 13, whereas combined-flow ripple *RI* range between 8 and 12. Previous experiments report an even greater range, from ~ 5 to over 30 (Allen 1979; Carstens et al. 1969; Harms 1969; Inman and Bowen 1963; Kennedy and Falcon 1965; Lofquist 1978; Miller and Komar 1980; Southard et al. 1990). While oscillatory-flow ripples generally become flatter (higher *RI*) with increasing oscillatory velocity (Allen 1979; Arnott and Southard 1990; Carstens et al. 1969; Harms 1969; this study), combined-flow ripples tend to become steeper (lower *RI*) with increasing unidirectional velocity.

Symmetry – As previously observed (e.g., Harms 1969; Inman and Bowen 1963; Yokokawa 1995) the superposition of an increasing unidirectional current on a symmetric oscillatory flow forces symmetric ripples to become progressively more

asymmetric. In the field for small-scale ripples, this trend was observed, although no precise value of *SI* marks the boundary between symmetric and asymmetric ripples. The *SI* index had previously been proposed to differentiate small-scale oscillatory-flow and combined-flow ripples (SI ≤ 3) from unidirectional-flow ripples (*SI* > 4) (Yokokawa 1995). Although this study did not generate unidirectional-flow ripples, all of our small-scale oscillatory-flow and combined-flow ripples have *SI* << 3 ($SI_{max.}$ = 1.6). In contrast, for large-scale ripples, the symmetry index clearly differentiates the symmetric (*SI* ≤ 2) from asymmetric (*SI* > 2) bed forms. To our knowledge, this is the first time that *SI* was systematically measured for large-scale oscillatory-flow and combined-flow ripples.

In addition, Figures 2.3 to 2.5 show that the boundary between symmetric and asymmetric bed forms slopes downwards to the right, indicating that: 1) for a given U_u, bed forms become more asymmetric with increasing U_o, and 2) large ripples become asymmetric at lower U_u (~ 8-10 cm/s) than do small ripples (~ 10-12 cm/s). The latter reflects a more effective wave-current coupling under higher oscillatory velocities (U_o > ~ 50 cm/s) and confirms earlier observations made by Arnott and Southard (1990) under similar flow conditions.

Steepness of lee faces – The angle of the lee side increases with increasing U_u, and can be used as a proxy for the degree of asymmetry.

Oscillatory-flow and oscillatory-dominant combined-flow ripples (U_u ≤ 10 cm/s) have lee-side dip angles < ~ 24° with the exception of reverse large ripples, which have slightly steeper lee sides. Similarly, Harms (1969) observed lee-side dip angles ≤ 23° for oscillatory ripples, although Miller (1980a) reported angles of ~ 32°.

Unidirectional-dominant combined-flow ripples (U_u > 10 cm/s) display a wide range of lee-side dip, although lee sides have steep dips (up to > 30°) overall. This is

comparable to a previous study which found combined-flow ripples to have lee-side dip angles ~ 23-34° (Harms 1969).

Roundness – Roundness of the ripple profile has long been recognized as a good indicator of combined-flow conditions (Bucher 1919; Harms 1969). Roundness was first quantified by Yokokawa (1995). She introduced the roundness index to express the degree of convexity of the stoss side. In this study, we find the qualitative visual estimation of bed form roundness to be a more reliable and diagnostic indicator of combined-flow conditions than the roundness index. Bed forms generated in this study show a clear visible increase in roundness as conditions evolve from purely oscillatory-flow to increasingly unidirectional-dominant combined flow that is not well reflected by the *RDI* (*RDI* is between 0.45 and 0.65 for all bed forms). One exception is elevated *RDI* for hummocky bed forms; the index seems to capture the domal nature of these bed forms. In contrast, Yokokawa (1995) found that a *RDI* of 0.54 separated oscillation-dominated ($RDI \leq 0.54$) from current-dominated ($RDI > 0.54$) combined-flow ripples under short oscillatory periods.

Shape of crest, stoss side and lee side – Distinctive characteristics of both small-scale and large-scale oscillatory-flow ripples are the straight to concave-up stoss and lee sides, broad shallow troughs, and sharp, continuous crestlines with well defined brinkpoints. Similar descriptions are reported in the literature (e.g., Harms 1969; Yokokawa 1995). Locally, the crests of large-scale oscillatory ripples can also be round and crestlines more discontinuous (Table 2.2).

Features common to both small-scale and large-scale oscillatory-dominant ($U_u \leq$ 10 cm/s) combined-flow ripples include: straight to biconvex flanks, locally deep and narrow troughs, round crests, and more discontinuous crestlines than for oscillatory-flow ripples. In addition, unique to large-scale ripples are the local broad round crest with no

brinkpoint characteristic of hummocky bed forms. Arnott and Southard (1990) made similar observations.

With further increase in unidirectional velocity (U_u > 10 cm/s), stoss and lee sides become unequivocally biconvex, crests become well rounded and locally distinct from the brinkpoint, and local deep scours develop on the lower end of the stoss side. These result from the action of high-energy, localized and short-lived flow-separation eddies acting at the point of flow reattachment. The combination of this steep-walled scour and the biconvex nature of the stoss and lee faces gives the small-scale combined-flow ripples their unique "boxy" profile (Fig. 2.7, ripple #2). Another characteristic of these small combined-flow ripples are "bulging structures" created by local, short-lived deposition at the inflection point of the lee-side foreset (Fig. 2.7, ripple #3). These "bulging structures" along with the general rounder nature of the higher U_u small-scale combined-flow ripples were also observed by Yokokawa (1995). Both the "boxy" profile and the "bulging structure" are features unique to small-scale combined-flow ripples and could be helpful in distinguishing them from oscillatory-flow ripples. Large-scale combined-flow ripples of higher U_u (> 10 cm/s) also have a distinctive profile with a break in slope occurring between the steeper lower stoss side and the nearly horizontal crest area (Table 2.2). Also characteristic is the migration of the brinkpoint downstream of the crest. This feature was also noted by Bucher (1919). With a further increase in U_u, small-scale and large-scale combined-flow ripples would presumably increasingly resemble current ripples or dunes.

Planform geometry – In planform, small-scale oscillatory-flow ripples have straight, locally bifurcating crestlines, perpendicular to flow that form a 2D bed geometry. In contrast, large-scale oscillatory ripples have a more 3D planform geometry with mostly discontinuous crestlines. This is consistent with previous observations (Arnott and Southard 1990; Southard et al. 1990). The reason for the absence of large 2D

oscillatory-flow ripples is unknown. Perhaps, as for current ripples, there is no stable form of large-scale 2D oscillatory-flow ripples in sand-sized sediment. It is possible that as flow velocities and ripple dimension increase, secondary flows perpendicular to the main flow become more important and contribute to the generation of a more 3D bed geometry, as is hypothesized to occur in the transition from 2D to 3D unidirectional ripples and dunes (Allen 1985a).

With increasing U_u, there is an increase in ripple crestline discontinuity, and bed geometry becomes increasingly 3D. These variations in bed geometry were well summarized in diagrams by Harms (1969, 1982). Combined-flow ripples evolve to a 3D bed geometry at U_u ~ 10-15 cm/s for small-scale ripples and at U_u ~ 13-18 cm/s for large-scale ripples. Eventually, over a narrow range of U_u near the plane-bed boundary, the bed assumes a 2D geometry. As previously mentioned, these might represent a transitional bed configuration resulting from the suppression of turbulence associated with an increase in near-bed suspended-sediment concentration at the onset of plane-bed conditions (Bridge and Best 1988).

Scaling to Flow

In order to identify the potential scaling relationship between ripples and the flow, ripple wavelength (λ) was plotted against orbital diameter (d_0) (Fig. 2.10). In this paper, the relationship between wavelength and orbital diameter is described as being either orbital ($\lambda \approx d_0$), suborbital ($\lambda = Cd_0$, where $C << d_0$), or anorbital ($\lambda \neq f(d_0)$) regardless of ripple size, symmetry, or grain diameter. (This contrasts slightly with the original definitions; see Clifton, 1976). Small-scale bed forms (λ < 20 cm) show no relationship with flow conditions (i.e., they are anorbital ripples); that is, an increase in the orbital diameter does not result in a commensurate increase in ripple spacing. Rather, the wavelength of small-scale oscillatory-flow and combined-flow ripples remains constant at

~ 10 cm regardless of orbital diameter. In the literature, small-scale oscillatory ripples generated under long oscillation periods are suborbital (Arnott and Southard 1990; Komar 1974; Southard et al. 1990). Clifton's observations (1976) suggest that ripples in fine sand are suborbital at moderate oscillatory velocities (U_0 = 15-25 cm/s) but anorbital at higher velocities (U_0 = 25-70 cm/s). Under short oscillation periods, the case of most experiments, small oscillatory ripples are typically observed to be orbital (Campbell 1966; Carstens et al. 1969; Clifton and Dingler 1984; Harms 1969; Inman and Bowen 1963; Kennedy and Falcon 1965; Komar 1974; Lofquist 1978; Miller and Komar 1980).

Wavelength of large-scale bed forms (λ > 1 m) increased linearly with orbital diameter (Fig. 2.10). A linear regression using data from all three data sets yields the following relationship: $\lambda = 1/2\ d_0 + 38.5$ (correlation coefficient = 0.81). The d_0/λ ratio for large bed forms (SLR, HM, ALR, RLR) is therefore ~ 2, and these ripples are classified as orbital. This finding, which is consistent with previous studies (Arnott and Southard 1990; Murray et al. 1991; Southard et al. 1990), provides a useful tool to geologists who wish to reconstruct paleohydraulic conditions when working in the stratigraphic record. For example, if depth can be inferred (trace fossil, stratigraphic relationships, association with other sedimentary structures), knowing the bed form's wavelength and that it scales to the orbital diameter of the oscillatory flow would make it possible to estimate wave characteristics such as oscillation period, wave height, and maximum oscillatory flow velocity (Allen 1979; Clifton and Dingler 1984; Komar 1974). Another important implication of the scaling relationship between the wavelength of large-scale bed forms and d_0 is that large orbital diameters can only be generated by large waves, which in turn need large unrestricted bodies of waters to form.

Stratification

The synthetic aggradation technique described in Southard et al. (1990) is used herein to simulate deposition in the presence of bed forms. Particular attention is given to the stratification generated by symmetrical large-scale and hummocky bed forms, since they are the most likely feature that forms hummocky cross-stratification observed in the shallow marine rock record (Cheel and Leckie 1993). This intriguing sedimentary structure figured prominently in the geological literature of the 1980s (e.g., Allen 1985b; Dott and Bourgeois 1982; Duke 1985; Duke 1987; Eyles and Clark 1986; Greenwood and Sherman 1986; Klein and Marsaglia 1987; Leckie and Krystinik 1989; Swift and Figueiredo 1983; Walker et al. 1983). More recently, HCS has received much less attention (e.g., Gallagher 2003; Hill et al. 2003; Li and Amos 1999b; Myrow et al. 2002) even though many fundamental questions remain, namely, the generating flow conditions (oscillatory flow vs. combined flow) and the mechanism by which HCS forms (scour and drape vs. active bed form).

Figure 2.11 depicts two synthetic stratification profiles constructed by stacking 24 sidewall bed surfaces in five-minute intervals (total running time of 115 minutes). The profiles were compiled by first sequentially stacking the sidewall traces with an aggradation rate of the order of 1 mm/min, and erasing segments (truncation) that lay above later bed profiles. The choice of the imposed aggradation rate of 1 mm/min was based on observations of sedimentation rates during storm events on modern shelves (e.g., Cheel, personal communication 2004; Hill personal communication 2003; Madsen et al. 1993; Morton 1988). The uppermost flow-parallel profile (Fig. 2.11A) shows synthetic stratification produced by purely oscillatory flow (run S18R5; U_o = 75 cm/s), while the bottom profile (Fig. 2.11B) shows stratification generated by oscillatory-dominant combined flow (run S13R3; U_o = 80 cm/s, U_u = 5 cm/s). Both profiles display many of the diagnostic characteristics of HCS outlined by Harms (1975) (refer to Fig.

2.11). The diagrams clearly exhibit the characteristic swale-and-hummock morphology. Certain laminae thicken or thin laterally, giving the stratification a fan-like appearance with fluctuating dips. In addition, truncation surfaces commonly become conformable when traced laterally. Laminae generally dip < 15°, although high values (up to ~ 25°) are observed locally.

The two profiles differ with respect to the preferred dip direction. The stratification from the oscillatory-flow run (Fig. 2.11A) is isotropic, in that it shows no preferred dip direction. In contrast, the combined-flow run stratification (Fig. 2.11B) is more anisotropic despite an approximately symmetrical surface profile. This anisotropy results from preferential deposition on lee side of the bed form, and as a consequence, the bed form migrates streamwise. This supports earlier results which suggest that the addition of only a small unidirectional current (a few cm/s) to an intermediate oscillatory flow (~ 65-80 cm/s) causes bed forms to become anisotropic (Arnott and Southard 1990).

In summary, our experiments are consistent with the earlier work of Southard et al. (1990) and Arnott and Southard (1990), and suggest that some (much?) of the HCS observed in the rock record was generated by actively growing and migrating hummocky bed forms under long-period high-velocity oscillatory flows (U_0 > 40 cm/s) and oscillatory-dominant combined flows (U_u < 12 cm/s). Nevertheless, the latter is more likely, because the unidirectional flow component provides a mechanism to advect sediment into the area of deposition.

Effect of Oscillation Period

The wavelength of large-scale ripples is observed to decrease with wave period (T). This is likely caused by the decrease in the orbital diameter that occurs at shorter period. The piston excursion is fixed by the nature of the drive mechanism although, at shorter period (T = 8.0 s), the faster motion of the piston results in a poorer piston/water

coupling and consequently, in a shorter orbital diameter. Since large-scale ripples are orbital, a decrease in orbital diameter causes a decrease in wavelength. Small-scale ripples are anorbital, and therefore a decrease in orbital diameter does not affect their spacing. Other workers have also observed a decrease in ripple wavelength and height with a shortening of the wave period but have not elaborated on possible explanations (Harms 1969; Inman and Bowen 1963; Kennedy and Falcon 1965; Lofquist 1978; Southard et al. 1990).

At shorter oscillation period, bed phases are generated at lower velocities than at longer period (see Figs. 2.3 and 2.4). For example, the triple point among plane bed, symmetric ripples and asymmetric ripples occurs at U_0 ~ 80 cm/s and U_u ~ 8.5 cm/s for T = 10.5 s, but at U_0 ~ 76 cm/s and U_u ~ 5.5 cm/s for T = 8.0 s. The thinner boundary layer developed under shorter oscillation periods imparts greater peak shear stress at the bed (Middleton and Southard 1978). For this reason, at shorter period, a lower U_0 is needed to generate a shear stress equivalent to the one generated by higher U_0 under longer periods. As a consequence, all phase boundaries are shifted towards lower velocities (down and left) when the oscillation period is reduced from 10.5 to 8 s. However, part of the boundary shift might be explained by lack of data points constraining the phase boundaries.

Another potentially significant observation is that hummocky bed forms were better developed under long oscillation periods (compare Figs. 2.3 and 2.5 with Fig. 2.4). If HCS is indeed generated by these hummocky bed forms, then this implies that HCS should be more common in large, deep, and unsheltered bodies of water where high-energy long-period waves can develop.

Effect of Grain Size

The height of ripples is observed to increase with grain size. In the literature, increase in ripple dimensions is also commonly reported to accompany increase in sediment size (Carstens et al. 1969; Kennedy and Falcon 1965; McKee 1965; Miller and Komar 1980; Sleath 1976; Van Rijn et al. 1993). In addition, 3D (vs. 2D) oscillatory and combined-flow ripples are better developed in runs that used the finer grain size (0.14 mm). This was previously observed for oscillatory ripples (Southard et al., 1990).

The increase in threshold velocity associated with the increase in grain size is reflected in the shift of the phase boundaries towards higher velocities. Most significantly, the field for large-scale ripples is greatly expanded and U_0 needs to exceed 120 cm/s for plane bed to form. In addition, reverse large ripples formed only in runs using the coarser sediment (0.22 mm). The reason for the absence of reverse large ripples in the finer sediment is unknown.

Grain size also influences the extent of the hummocky zone. Hummocks are present over a narrower velocity range in the runs that use the coarser sediment. From this observation, it is possible to hypothesize that, with further increase in grain size, hummocks would presumably disappear. This supports evidence from the rock record, where HCS is most common in sediment of silt to fine sand size (e.g., Cheel and Leckie 1993; Dott and Bourgeois 1982).

CONCLUSIONS

This experimental study investigated equilibrium bed forms generated by long-period oscillatory and combined flows with the objective of providing tools for geologists to better understand modern and ancient shallow marine depositional environments. Our results show that:

- Equilibrium bed forms under the range of conditions explored are: small symmetric and asymmetric ripples, large symmetric and asymmetric ripples, reverse large ripples, and plane bed.
- The phase boundary for combined-flow plane bed is experimentally defined for the first time.
- Hummocky bed forms occur in conjunction with other bed forms and are, therefore, not considered to be a distinct bed phase.
- Phase diagrams are consistent with findings of earlier exploratory work by Arnott and Southard (1990).
- Small ripples have wavelength < 20 cm and large ripples > 100 cm; no intermediate size ripples were generated.
- The boundary between symmetric and asymmetric ripples is defined by a symmetry index of 2.
- Small combined-flow ripples can be distinguished from oscillatory-flow ripples by their round crest, convex-up sigmoidal profile, local pronounced scour at the toe of the stoss ("boxy" profile), and more 3D planform.
- Large combined-flow ripples have features similar to small combined-flow ripples but, in addition, have a characteristically long stoss side with a marked change in slope (steeper lower section and nearly horizontal crest area), and

a 3D planform that becomes 2D when the plane-bed phase boundary is approached.

- Small-scale and large-scale ripples behave differently with respect to scaling of the bed-form wavelength (λ) versus the orbital diameter of the oscillatory motion (d_0). Small ripples do not scale to the flow (anorbital ripples), whereas large bed forms scale to the flow with a $d_0/\lambda \sim 2$ (orbital ripples).
- Stratification exhibiting many of the characteristics of HCS was generated by aggrading large 3D ripples using a synthetic stratification technique. Our experiments suggest that HCS can be generated by migrating hummocky bed forms under either purely oscillatory flow ($U_0 \sim$ 50-90 cm/s) or oscillatory-dominant combined flow ($U_u <$ ~ 12 cm/s). A further increase in U_u causes bed forms to become asymmetric, migrate downstream, and generate anisotropic stratification not unlike that of unidirectional-flow dunes.
- Hummocky bed forms are better developed under the longer period (10.5 s or 9.4 s unscaled) and in finer sediment (0.14 mm or 0.11 mm unscaled). Under shorter periods (< ~ 8 s) and in coarser sediment (> ~ 0.22 mm) hummocky bed forms would presumably cease to develop. This implies that HCS should be more commonly generated during high-energy storm events in large, deep, and unsheltered bodies of water where long-period waves can form and where fine sediment (very fine to fine sand) is available.

Fig. 2.1 Diagram of combined-flow tunnel (side view). Oscillatory flow is generated by motor-driven coupled pistons 1 and 2. Unidirectional flow component can be added by turning on a slurry pump; flow in tunnel is from left to right.

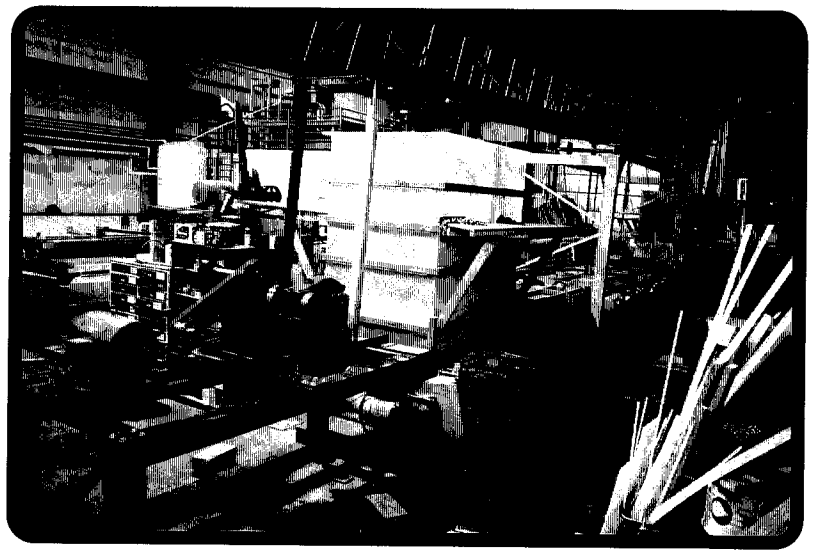

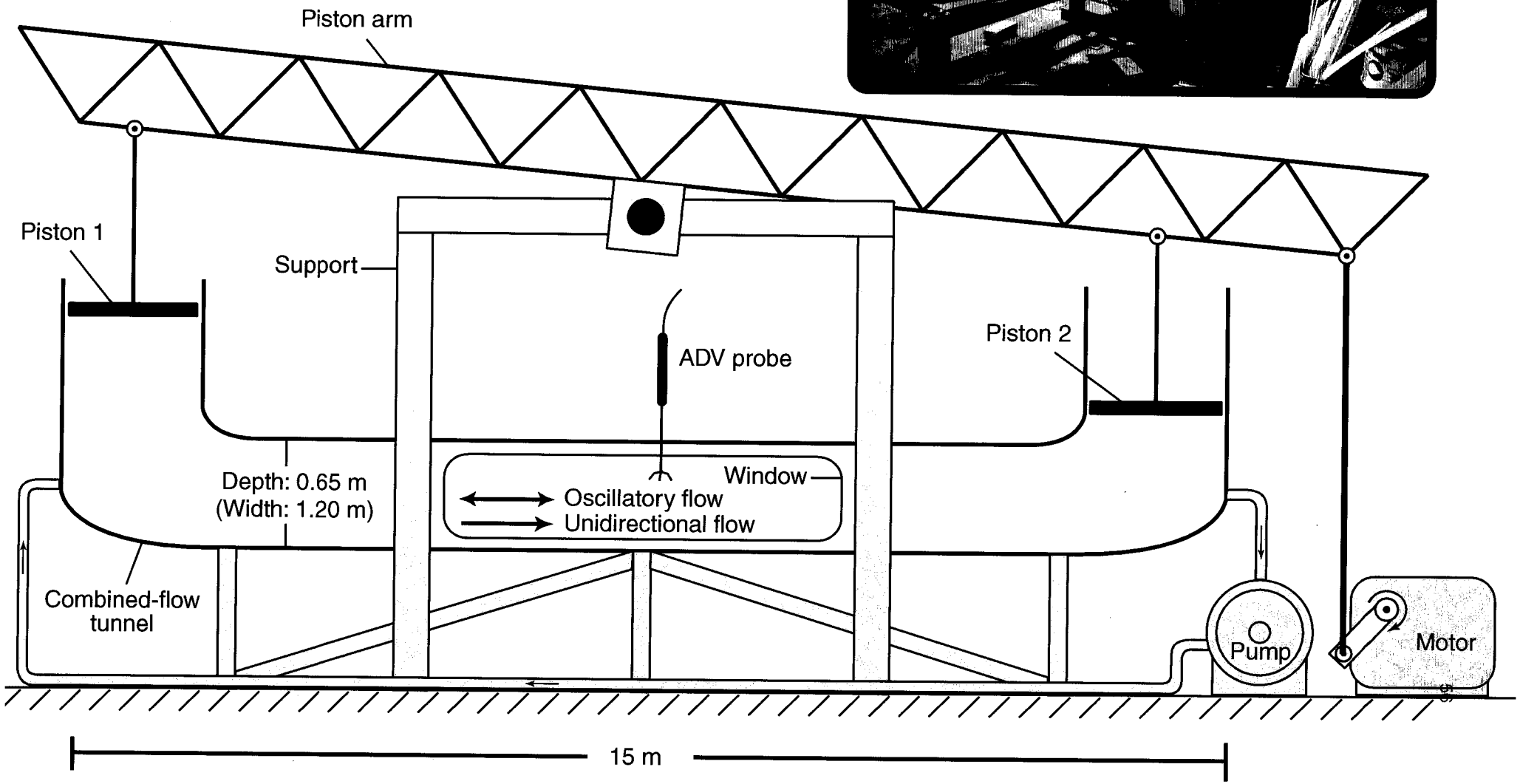
Piston arm
Piston 1
Support
ADV probe
Piston 2
Depth: 0.65 m
(Width: 1.20 m)
Window
Oscillatory flow
Unidirectional flow
Combined-flow
tunnel
Pump
Motor
15 m

Fig. 2.2 Ripple morphology. Terminology used to describe the ripples generated in the combined-tunnel.

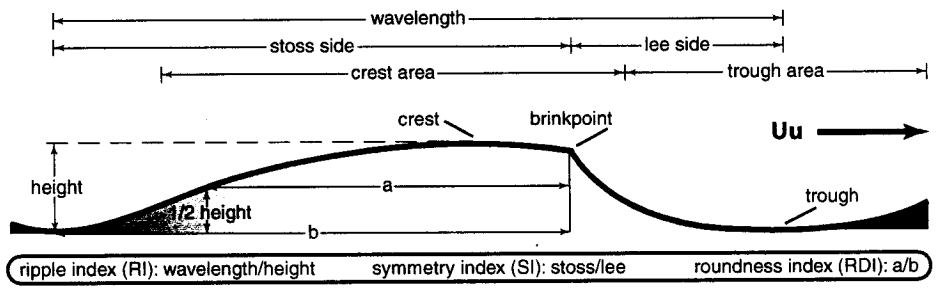
wavelength
stoss side
lee side
crest area
trough area
crest
brinkpoint
Uu
height
a
1/2 height
b
trough
ripple index (RI): wavelength/height
symmetry index (SI): stoss/lee
roundness index (RDI): a/b

Fig. 2.3 Combined-flow phase diagram 1 (ϕ = 0.14 mm, T = 10.5 s) with oscillatory velocity and unidirectional velocity as axes. Solid circles, runs; open circles, hummocky bed form; shaded area, hummocky zone.

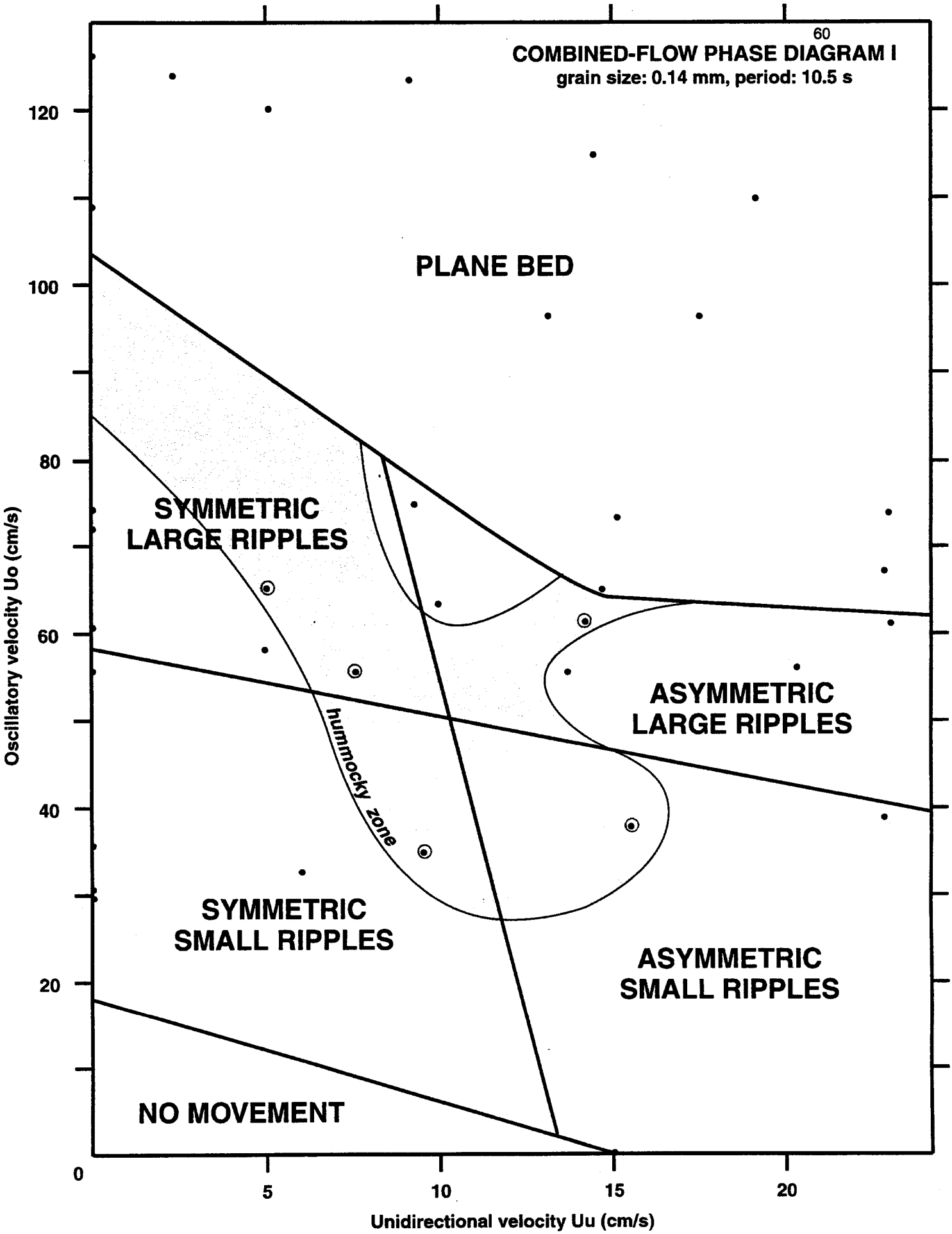
COMBINED-FLOW PHASE DIAGRAM I
grain size: 0.14 mm, period: 10.5 s
PLANE BED
SYMMETRIC
LARGE RIPPLES
ASYMMETRIC
LARGE RIPPLES
hummocky zone
SYMMETRIC
SMALL RIPPLES
ASYMMETRIC
SMALL RIPPLES
NO MOVEMENT
Oscillatory velocity Uo (cm/s)
Unidirectional velocity Uu (cm/s)
0
20
40
60
80
100
120
5
10
15
20

Fig. 2.4 Combined-flow phase diagram 2 (ϕ = 0.14 mm, T = 8.0 s) with oscillatory velocity and unidirectional velocity as axes. Solid circles, runs; open circles, hummocky bed form; shaded area, hummocky zone.

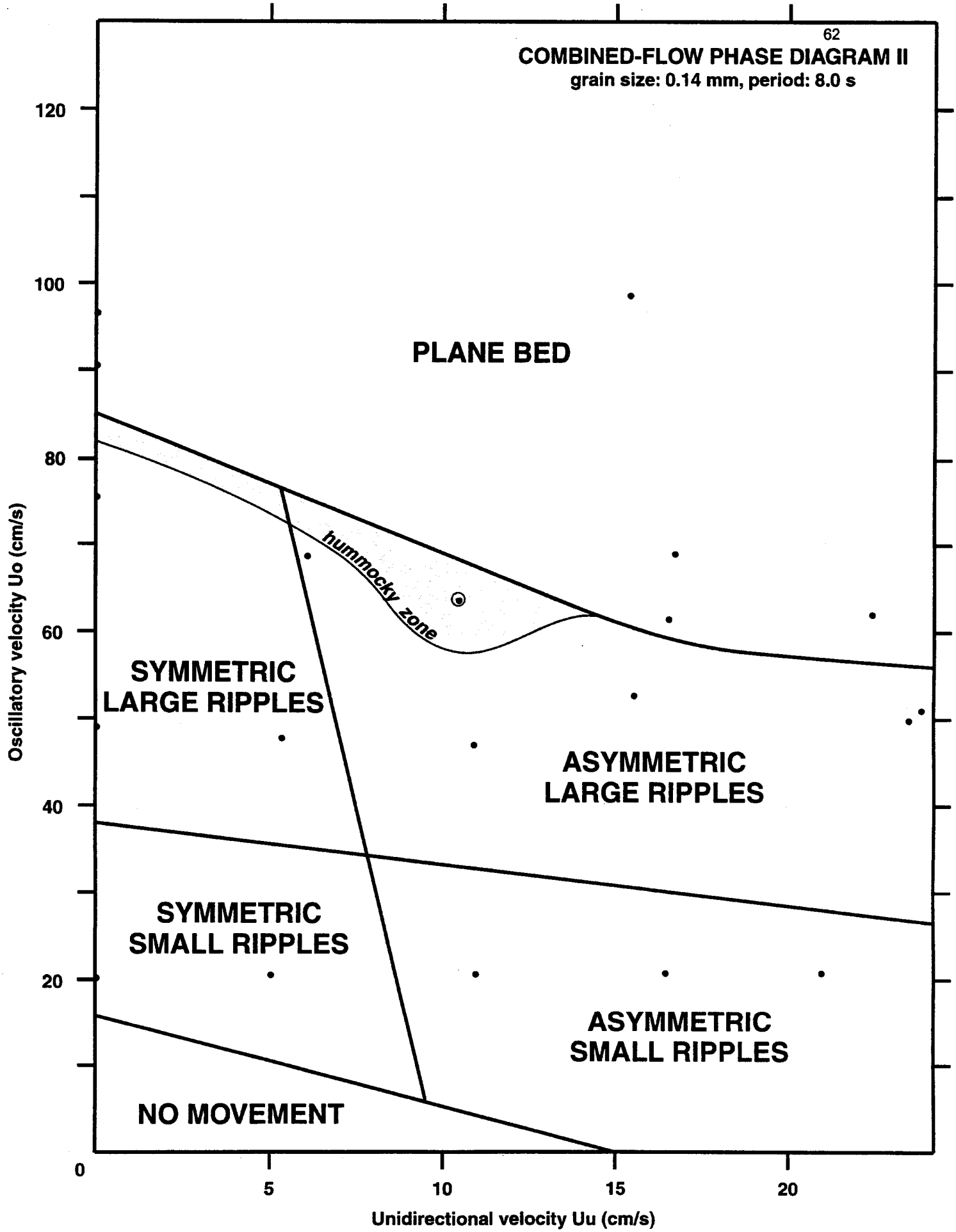
COMBINED-FLOW PHASE DIAGRAM II
grain size: 0.14 mm, period: 8.0 s
PLANE BED
hummocky zone
SYMMETRIC
LARGE RIPPLES
ASYMMETRIC
LARGE RIPPLES
SYMMETRIC
SMALL RIPPLES
ASYMMETRIC
SMALL RIPPLES
NO MOVEMENT
Oscillatory velocity Uo (cm/s)
Unidirectional velocity Uu (cm/s)
0
20
40
60
80
100
120
5
10
15
20

Fig. 2.5 Combined-flow phase diagram 3 (ϕ = 0.22 mm, T = 10.5 s) with oscillatory velocity and unidirectional velocity as axes. Solid circles, runs; solid triangles, additional runs (see text); open circles, hummocky bed form; shaded area, hummocky zone.

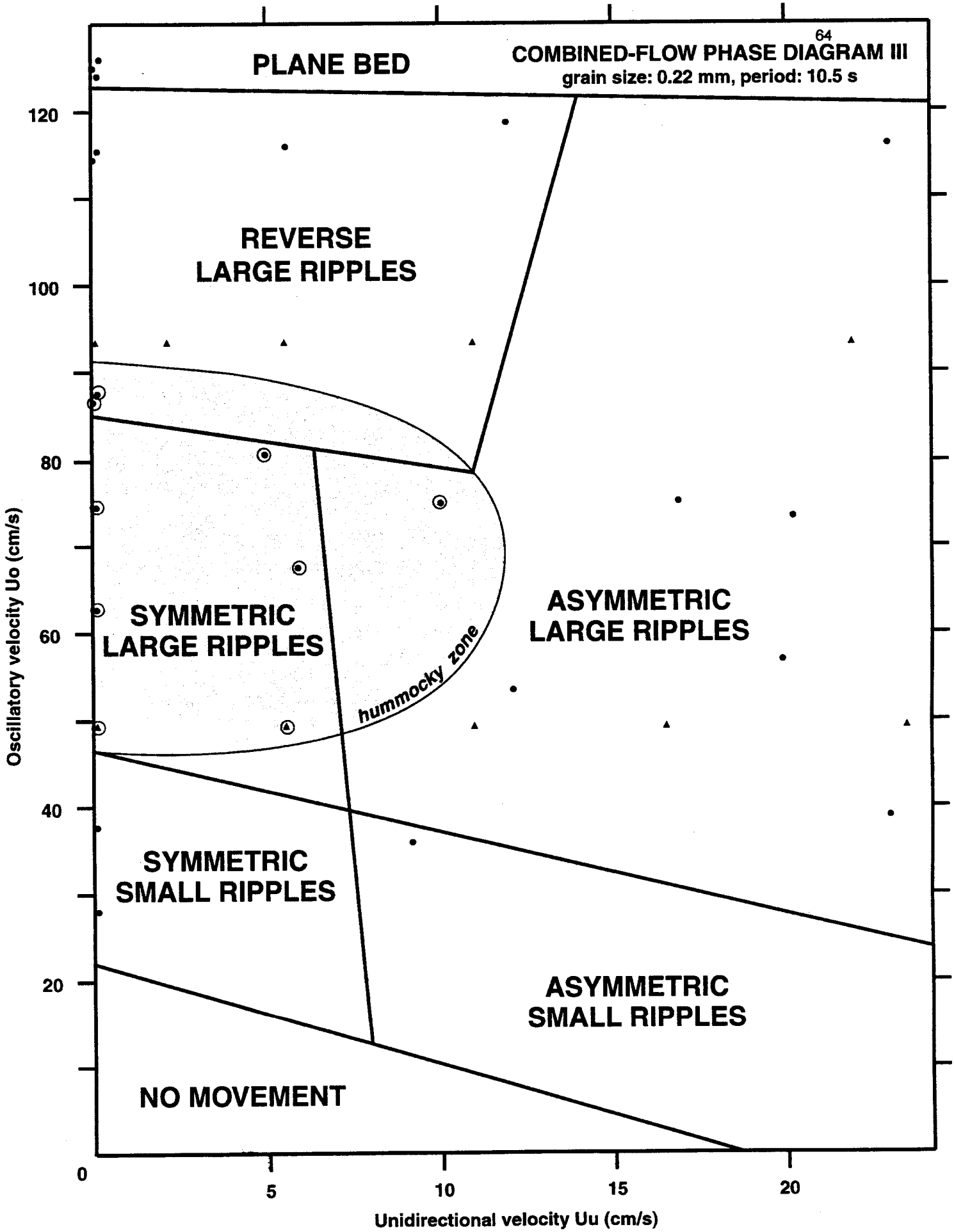
PLANE BED
COMBINED-FLOW PHASE DIAGRAM III
grain size: 0.22 mm, period: 10.5 s
REVERSE
LARGE RIPPLES
SYMMETRIC
LARGE RIPPLES
hummocky zone
ASYMMETRIC
LARGE RIPPLES
SYMMETRIC
SMALL RIPPLES
ASYMMETRIC
SMALL RIPPLES
NO MOVEMENT
Oscillatory velocity Uo (cm/s)
Unidirectional velocity Uu (cm/s)
0
20
40
60
80
100
120
5
10
15
20

Fig. 2.6 Oscillatory-flow and combined-flow small-scale ripples. Current is from left to right. Scale bar divisions: 10 cm. (A) Small symmetric 2D oscillatory-flow ripples, S12R1, U_0 = 20.1 cm/s, U_u = 0 cm/s. Characterized by straight to concave-up flanks, sharp crests, broad troughs, continuous crestline perpendicular to flow in planform. (B) Small symmetric 2.5D (locally 2D and locally 3D) combined-flow ripples, S12R3, U_0 = 20.6 cm/s, U_u = 10.9 cm/s. Characterized by straight to biconvex flanks, rounder crests, less continuous and bifurcating crestline in planform. (C) Small asymmetric 3D combined-flow ripples, S12R5, U_0 = 20.6 cm/s, U_u = 21.5 cm/s. Characterized by biconvex flanks, rounder crests, local deep scour at lower end of stoss side, discontinuous crestline, and irregular planform.

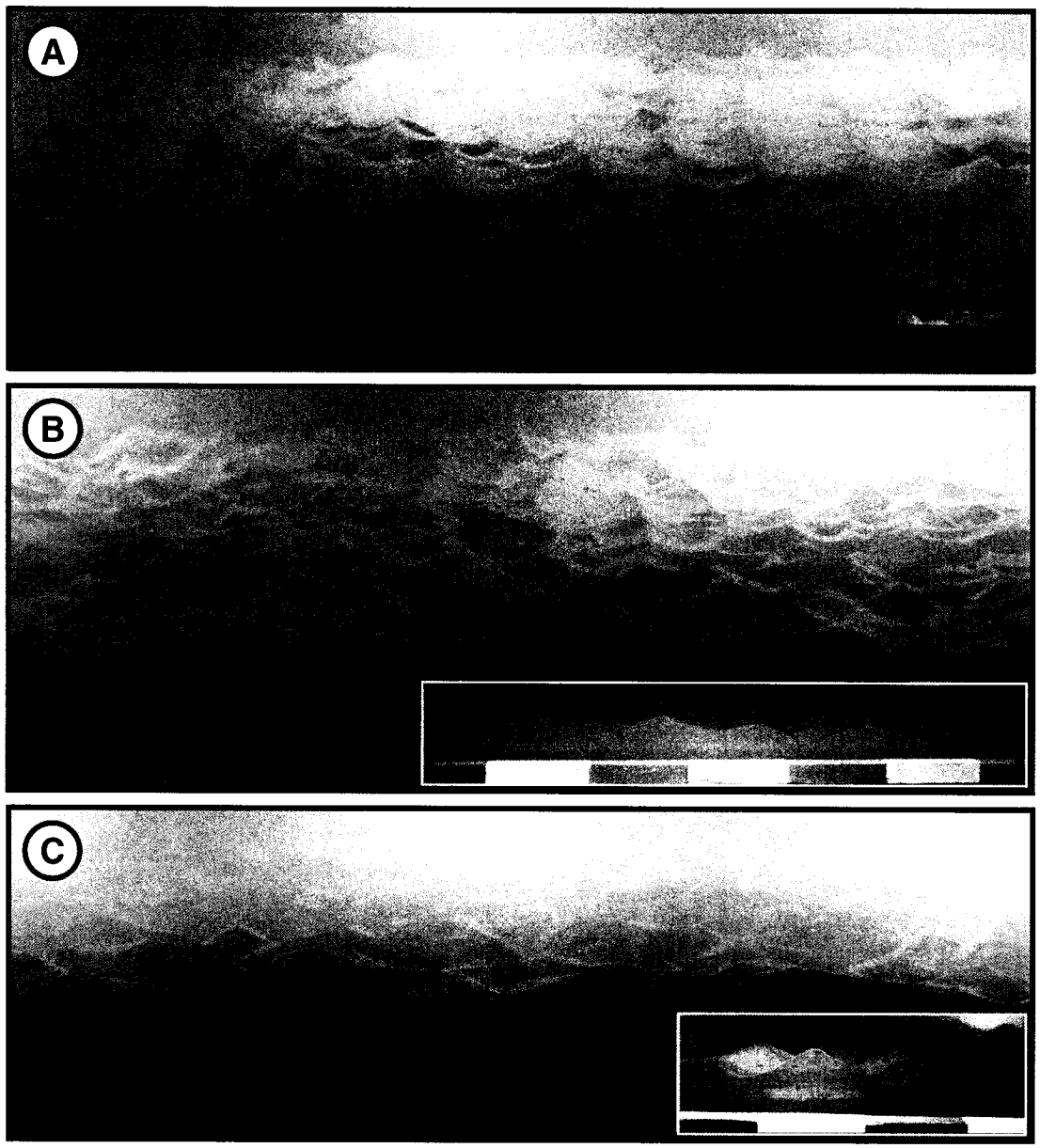
A
B
C

Fig. 2.7 Profile variations in combined-flow asymmetric small-scale ripples. (1) Most common biconvex ripple profile with "normal" scouring resulting in a smooth stoss side. (2) Biconvex but more "boxy" profile from intense, localized, and short-lived turbulent eddy producing a steep-walled scour pit at the lower end of the stoss side (with local overhangs). (3) "Bulging" structure from local deposition at inflection point of lee side. Velocity conditions: $U_0 < \sim 40$ cm/s, $U_u < \sim 12$ cm/s. Unidirectional flow is from left to right.

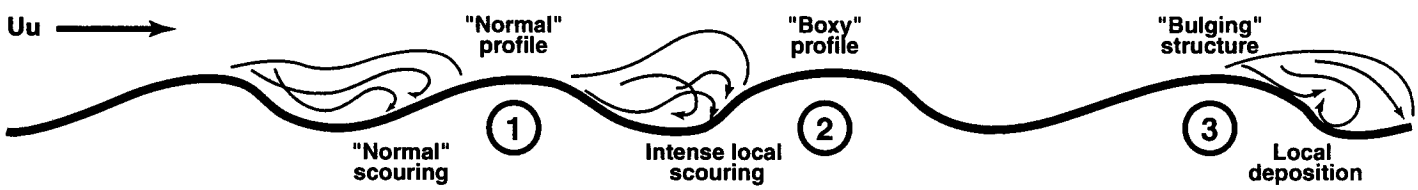
Uu
"Normal" profile
"Boxy" profile
"Bulging" structure
1
2
3
"Normal" scouring
Intense local scouring
Local deposition

Fig. 2.8 Oscillatory-flow and combined-flow large-scale ripples. Current is from left to right. Scale bar divisions: 10 cm. (A) Large symmetric 2D oscillatory-flow ripples, S5R1, U_0 = 60.7 cm/s, U_u = 0 cm/s (scale bar is in back window). Characterized by sharp crests equal to brinkpoint, straight flanks, continuous crestline perpendicular to flow in planform. (B) Reverse large asymmetric 2D combined-flow ripples, S15R3, U_0 = 120.1 cm/s, U_u = 5.6 cm/s. Characterized by round and diffuse crest, long wavelength of 200 cm to > 500 cm, continuous crestline in plan-form. (C) 3D hummocky combined-flow bed forms, S8R1, U_0 = 55.7 cm/s, Uu = 7.6 cm/s. Characterized by broad round crests, no brinkpoint, convex-up flanks, domal planform. (D) Large asymmetric 3D combined-flow ripples, S10R4, U_0 = 52.8 cm/s, U_u = 15.7 cm/s (meter stick is highlighted; field of view is ~ 200 cm). Characterized by separate crest and brinkpoint, round stoss with break in slope, local deep scour at lower end of stoss side, irregular plan form. (E) Large asymmetric 2D combined-flow ripples, S18R3, U_0 = 53.5 cm/s, U_u = 12.2 cm/s. Characterized by, round stoss with break in slope, local deep scour at lower end of stoss side, continuous and regular crestline perpendicular to flow in planform.

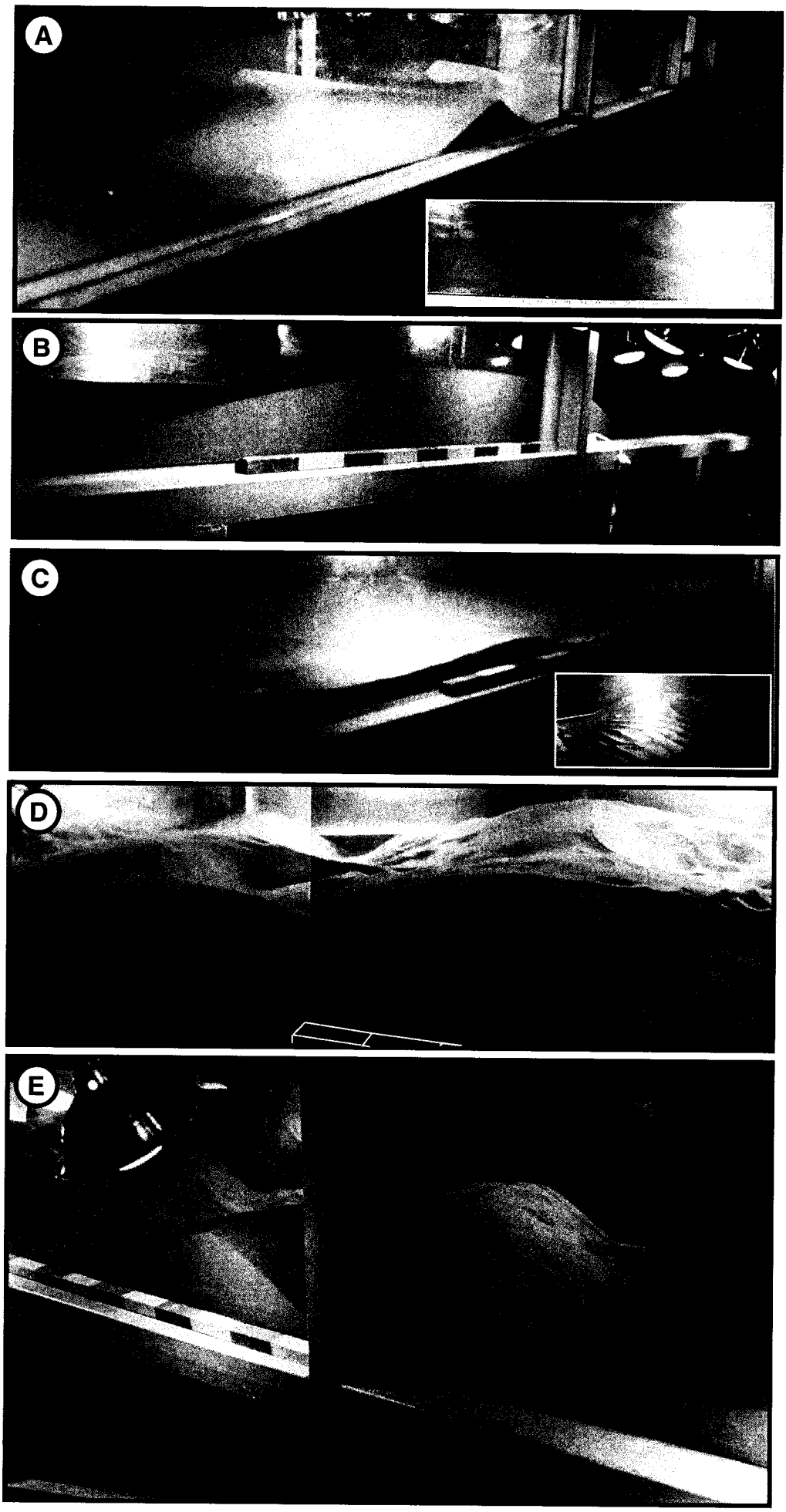
A
B
C
D
E

Fig. 2.9 Sediment dynamics and stratification of reverse large ripples. (1) U_0 and Uu are in the same direction, producing peak flow velocity and a large flow-separation eddy, violent scouring, and a highly concentrated cloud of suspended sediment at the toe of the steep lee side. (2) Flow stalls and reverses, eddying within the sediment cloud slows and the plume lifts. (3) Flow reverses and U_0 opposes U_u, the upstream migration of the cloud of sediment is inhibited by the downstream unidirectional component and deposition occurs just upstream of the brink point and all along the gently sloping stoss. (4) Comparison of the resulting stratification for combined-flow reverse large ripple versus asymmetric large ripple. The reverse large ripple migrates against the unidirectional flow, deposition zone is upstream of the erosion zone, and foreset dip into the current. The asymetric large ripple migrates with the unidirectional flow, deposition zone is dowstream of the erosion zone, and foreset dip away from the current. Under the conditions investigated (grain size = 0.14 mm, period = 10.5 s), the transition between reverse to "normal" large ripples occurred at U_u between 12 and 14 cm/s.

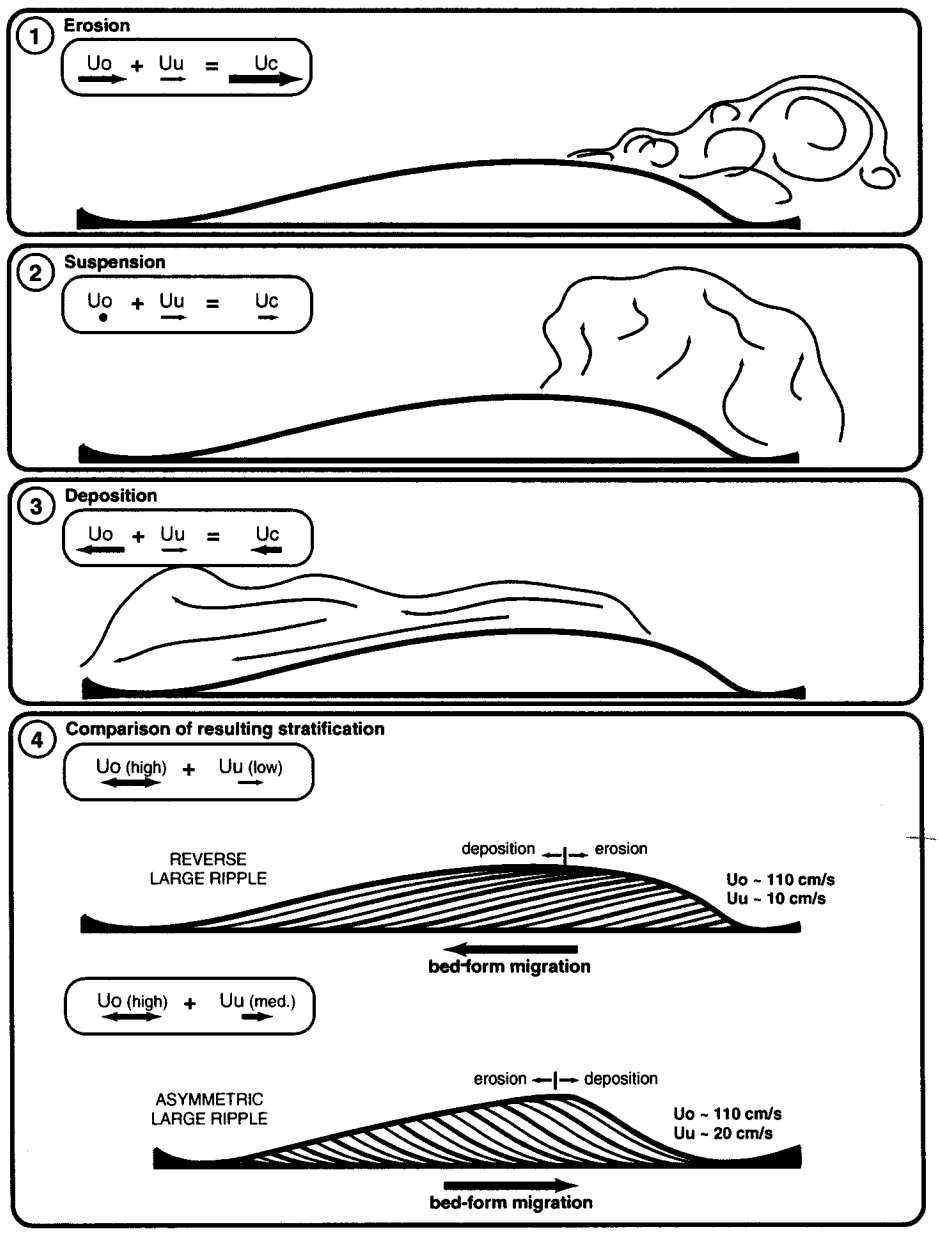
1
Erosion
Uo + Uu = Uc
2
Suspension
Uo + Uu = Uc
3
Deposition
Uo + Uu = Uc
4
Comparison of resulting stratification
Uo (high) + Uu (low)
REVERSE
LARGE RIPPLE
deposition
erosion
Uo ~ 110 cm/s
Uu ~ 10 cm/s
bed-form migration
Uo (high) + Uu (med.)
ASYMMETRIC
LARGE RIPPLE
erosion
deposition
Uo ~ 110 cm/s
Uu ~ 20 cm/s
bed-form migration

Fig. 2.10 Bed-form wavelength (λ) vs orbital diameter (d_o) of the flow. The orbital diameter is the horizontal distance traveled by a flow particle during the oscillation cycle (the maximum distance if the orbital is asymmetric, as in combined flow). Different grain size (ϕ) and oscillation period (T) conditions are represented by symbols (see legend). Small ripples do not scale to flow; wavelength is independent of the flow excursion. Large ripples scale to flow with a d_o/λ of ~ 2. Linear regression yields the following relationship for large ripples $\lambda = 0.52\ d_o + 38.5$ with a correlation coefficient of 0.8.

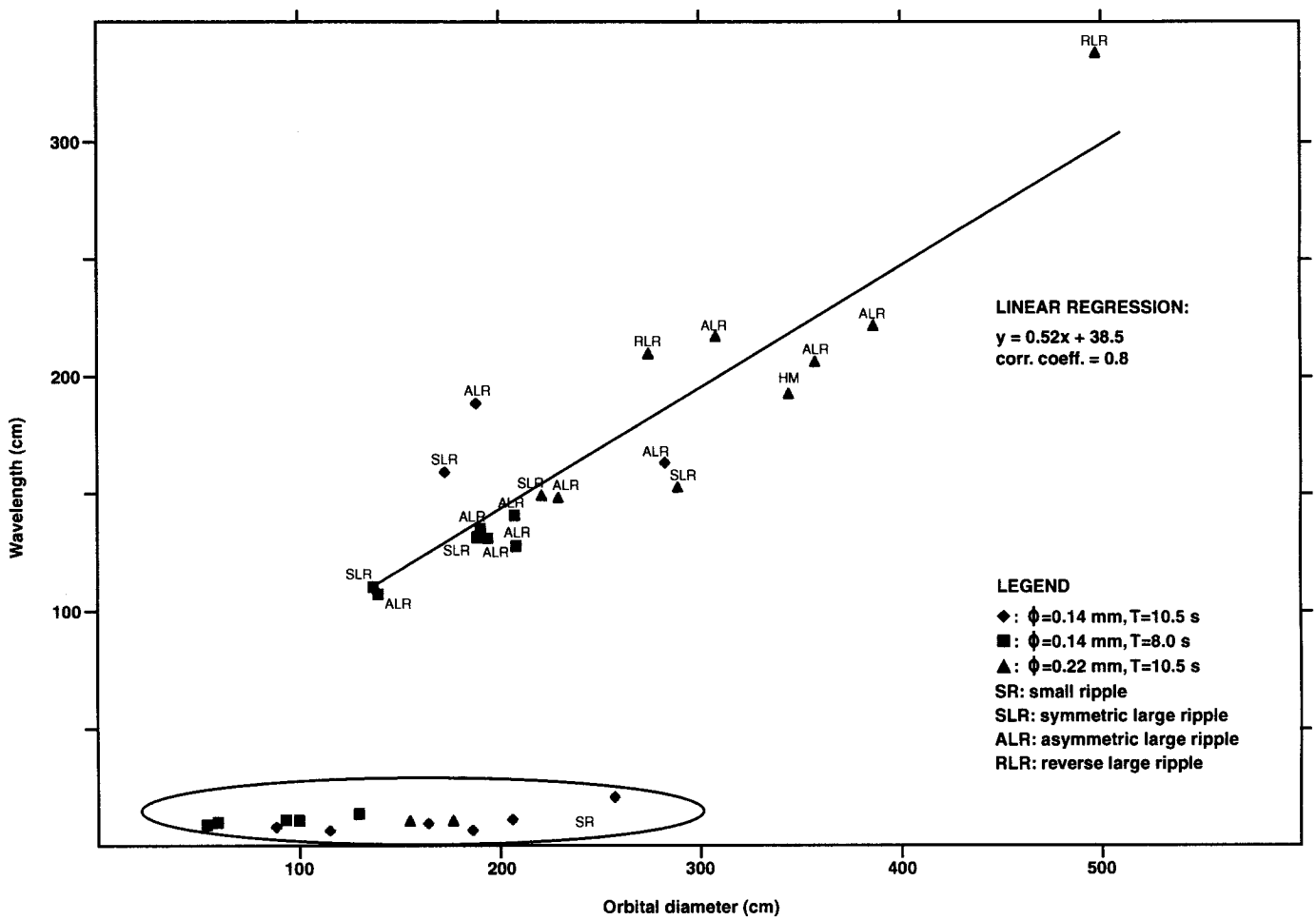
Wavelength (cm)
300
200
100
100
200
300
400
500
Orbital diameter (cm)
RLR
ALR
ALR
RLR
ALR
HM
ALR
SLR
ALR
SLR
SLR
ALR
ALR
ALR
SLR
ALR
SLR
ALR
SR
LINEAR REGRESSION:
y = 0.52x + 38.5
corr. coeff. = 0.8
LEGEND
◆: ϕ=0.14 mm, T=10.5 s
■: ϕ=0.14 mm, T=8.0 s
▲: ϕ=0.22 mm, T=10.5 s
SR: small ripple
SLR: symmetric large ripple
ALR: asymmetric large ripple
RLR: reverse large ripple

Fig. 2.11 Synthetic stratification. Time series of 24 bed profiles taken at five-minute intervals for a total running time of 115 minutes. Vertical and horizontal scales are equal. Current is from left to right. Conditions are scaled to 10° Celsius. Run conditions are listed in diagram. **A.** Purely oscillatory-flow run. **B.** Oscillatory-dominant combined-flow run. The resulting stratifications display many of the diagnostic features of hummocky cross-stratification (HCS) listed by Harms (1975). The characteristic hummocks are preserved when there is: (1) a change in migration direction, (2) climbing conditions, (3) spontaneous growth of a hummock from a swale. (4) truncation surface becomes conformable when traced laterally. (5) thickening and thinning of laminae result in fan-like stratification and fluctuating dips. (6) laminae dips occasionally reach higher value but are mostly in the classic HCS range (< 15°).

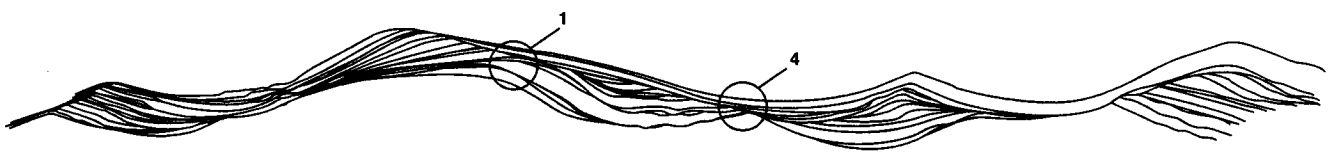

Ⓐ **Pure oscillatory flow**

S18R5
Uo = 75 cm/s
Uu = 0 cm/s
T = 10.8 s

grain size = 0.23 mm
wavelength = 224 cm
aggradation rate = 1.0 mm/min
equilibrium bed forms: SLR and HM

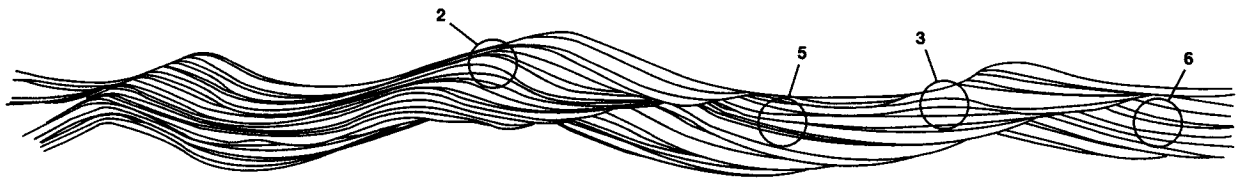

Ⓑ **Oscillatory dominant combined flow**

S13R3
Uo = 80 cm/s
Uu = 5 cm/s
T = 10.8 s

grain size = 0.23 mm
wavelength = 187 cm
aggradation rate = 1.5 mm/min
equilibrium bed forms: SLR and HM

1 meter

Table 2.1 Summary of flow parameters and bed form geometry variables (scaled to 10°C)

* : Run identifier; S refers to the series and R to the run within that series
† : Oscillatory velocity; average of the top 20% of the velocity values recorded during the sampling period
‡ : Unidirectional velocity; velocity measured at the beginning of the run
£ : Ripple index (RI); ripple wavelength/ ripple height
§ : Bed form key: SR, small ripple; PL, plane bed; SLR, symmetric large ripple; ALR, asymmetric large ripple; HM, hummocky bed form; RLR, reverse large ripple (large scale bed form with steeper face dipping away from migration direction); r, superimposed small-scale ripples. *Note:* equilibrium bed configurations were often constituted of several bed forms, but for the sake of simplicity, only the dominant bed form of each run is presented in Table 1.
€ : Number of dimensions of bed form: 2D, two-dimensional; 3D, three-dimensional; 2.5D, locally 2D and locally 3D
¥ : Symmetry of bed form in profile: S, symmetrical; AS, asymmetrical
Ψ : Symmetry index (SI): horizontal lenght of the stoss side/ horizontal length of the lee side
ϑ : Roundness index (RDI): length of the stoss side at half the bed form height/ the full horizontal length of the stoss side
ξ : Note: if only one value is presented it is the dip of the lee side, if two values it is as follows: stoss side dip/lee side dip
ɜ : Orbital diameter of the flow (d_0); x+, downstream portion of the oscillation cycle (in the direction of the unidirectional flow)
Θ : x-, upstream portion of the oscillation cycle (against the unidirectional flow)
Ω : Ratio of the orbital diameter (d_0) to bed form wavelength (λ). $d_0/\lambda \sim 1$ indicate that bed forms scale to flow and are termed "orbital" ripples
ζ : Migration direction, key: u, upstream migration of bed form (against the unidirectional flow; x-); d, dowstream migraton of bed form (with the unidirectional flow; x+); capitalized letters represent dominant migration direction. Note: when two migration directions, migration rates are for the dominant one
€ : Running time to reach equilibrium bed configuration (hours:minutes)
ς : Morphological attributes of the small superimposed ripples of the same run

Table 2.1 Summary of flow parameters and bed form geometry variables (scaled to 10°C)

Run ID*	Oscil. Period (s)	Uo (cm/s)†	Uu (cm/s)‡	Grain Size (mm)	Ripple Wavelength (cm)	Ripple Height (cm)	Ripple Index[c]	Bed Form[§]	"3D"[¶]	S[¥]	SI[¥]	RDI[¤]	Dip (°)[ξ]	d_0 (x+) (cm)[»]	d_0 (x-) (cm)[Θ]	d_0/λ[α]	Migr. speed (cm/h)	Migr. Dir.[ε]	Time[#]
S2R1	10.3	30.7	0.0	0.13	8.0	1.3	6.0	SSR	2D	S	-	-	18	88.0	-	11.1	-	ud	3:00
S2R2	10.3	35.6	0.0	0.13	6.5	0.5	13.5	SSR	2D	S	-	-	10/11.4	114.6	-	17.6	-	ud	14:30
S2R3	10.3	55.7	0.0	0.13	6.5	0.4	18.0	SSR	2D	S	-	-	-	185.7	-	28.5	-	ud	1:00
S2R4	10.3	126.2	0.0	0.13	277.4	4.9	56.1	PL	-	-	-	-	2	422.1	-	1.5	-	ud	3:35
S3R1	10.3	71.3	0.0	0.13	160.4	12.1	13.3	SLR	2D	S	-	-	10-15/20-25	-	-	-	-	-	8:00
S3R2	10.3	61.3	22.9	0.13	139.9	18.1	7.7	ALR	2D	AS	-	-	9.2/26.7	-	-	-	-	-	2:40
S4R1	10.2	124.1	2.3	0.13	-	-	-	PL	-	-	-	-	-	-	-	-	-	ud	17:30
S4R2	9.8	120.1	5.1	0.12	-	-	-	PL	-	-	-	-	-	-	-	-	-	ud	20:45
S4R3	10.1	123.4	9.2	0.13	306.4	17.6	17.4	PL	-	-	0.60	0.69	5-13	-	-	-	-	uD	18:20
S4R4	9.4	115.0	14.4	0.11	217.9	10.3	21.2	PL	-	-	0.51	0.46	6	-	-	-	77.0	d	3:15
S4R5	9.0	110.1	19.2	0.10	-	-	-	PL	-	-	-	-	1-3	-	-	-	-	d	0:40
S4R6	10.5	96.5	17.5	0.14	-	-	-	PL	-	-	-	-	-	-	-	-	-	d	3:25
S4R6b	10.5	96.5	13.2	0.14	274.7	2.5	110.0	PL	-	-	-	-	-	-	-	-	-	d	-
S5R1	9.2	60.7	0.0	0.11	159.4	12.5	12.8	SLRr	2.5D	AS	1.49	0.51	11.3/21.5	172.9	-	1.1	14.7	Ud	16:00
S5R2	9.7	58.3	5.1	0.12	161.3	9.8	16.5	SLRr	2.5D	AS	1.83	0.65	7.2/14.4	-	-	-	40.3	uD	11:30
S5R2b	10.4	65.5	5.3	0.14	169.0	6.4	26.4	HM	2.5D	S	0.91	0.56	4.4/4.8	-	-	-	-	uD	15:00
S5R3	10.7	74.9	9.3	0.14	115.6	11.3	10.2	ALRr	2D	AS	1.22	0.31	16.2/14.1	-	-	-	17.4	u	21:30
S5R3b	10.7	63.4	10.0	0.14	133.3	12.1	11.0	ALR	2.5D	AS	1.73	0.47	9.8/18.7	-	-	-	21.2	uD	16:45
S5R4	10.0	73.4	15.2	0.13	-	-	-	PL	-	-	-	-	-	-	-	-	-	d	2:10
S5R5	10.3	61.3	14.2	0.13	163.0	9.2	17.7	HM	2.5D	AS	-	-	6.8/11.4	-	-	-	130.8	d	4:25
S5R5b	10.3	65.5	14.7	0.13	-	-	-	PL	-	-	-	-	-	-	-	-	-	-	1:35
S5R6	10.5	67.3	22.8	0.14	-	-	-	PL	-	-	-	-	-	-	-	-	-	-	0:30
S5R7	10.6	73.9	0.0	0.14	150.3	7.6	19.9	SLR	2.5D	S	1.24	0.46	16.0/15.0	-	-	-	-	-	6:00
S5R7b	10.6	73.9	22.9	0.14	-	-	-	PL	-	-	-	-	-	-	-	-	292.3	d	1:30
S6R1	10.3	29.8	0.0	0.13	8.1	0.7	11.5	SSR	2D	S	-	-	-	-	-	-	-	-	3:10
S6R2	10.3	32.8	6.0	0.13	7.2	0.6	12.2	SSR	2.5D	S	-	-	-	-	-	-	-	-	5:15
S6R3	10.4	34.9	9.5	0.14	9.5	0.9	10.3	SSR	2.5D	S	-	-	-	163.7	103.4	17.3	14.4	d	5:00
S6R4	10.4	38.0	15.6	0.14	11.2	1.2	9.5	ASR	3D	AS	-	-	-	205.6	43.1	18.4	51.0	d	1:45
S6R5	10.2	38.9	22.8	0.13	20.7	1.9	10.9	ASR	3D	AS	1.56	0.80	10.9/13.8	256.7	37.3	12.4	219.1	d	1:00
S7R1	10.3	109.0	0.0	0.13	-	-	-	PL	-	-	-	-	-	-	-	-	-	-	-
S8R1	10.8	55.7	7.6	0.14	133.6	11.5	11.6	HMr	3D	S	1.87	0.68	11.4/14.9	-	-	-	13.3	d	6:45
S8R2	10.6	55.8	13.7	0.14	188.6	16.6	11.4	ALRr	2D	AS	3.12	0.55	7.0/23.4	188.7	158.3	1.0	-	d	3:30
S8R3	10.7	56.2	20.3	0.14	163.3	15.1	10.8	ALRr	2D	AS	-	-	7.2/27.8	282.8	105.4	1.7	21.3	d	3:30
S9R1	7.9	90.2	0.0	0.14	-	-	-	PL	-	-	-	-	-	-	-	-	-	-	1:45
S9R2	8.0	96.7	0.0	0.14	-	-	-	PL	-	-	-	-	-	-	-	-	-	-	-
S9R3	8.0	94.8	15.7	0.14	-	-	-	PL	-	-	-	-	-	-	-	-	-	-	1:10
S10R1	7.9	49.0	0.0	0.14	114.0	11.2	10.2	SLRr	2.5D	S	1.03	0.45	15/14	-	-	-	-	-	7:15
S10R1[ς]	7.9	49.0	0.0	0.14	8.9	0.5	16.4	SSR	2D	S	-	-	7.1/7.2	-	-	-	-	-	-
S10R2	7.9	47.7	5.3	0.14	110.5	9.8	11.3	SLRr	2.5D	AS	0.82	0.59	15.1/14.2	136.8	133.0	1.2	5.3	ud	4:30
S10R2[ς]	7.9	47.7	5.3	0.14	8.4	0.4	22.0	SSR	2D	S	-	-	-	-	-	-	-	-	"

Run ID*	Oscil. Period (s)	Uo (cm/s)†	Uu (cm/s)‡	Grain Size (mm)	Ripple Wavelength (cm)	Ripple Height (cm)	Ripple Index[ξ]	Bed Form[§]	"3D"[ε]	S[¥]	SI[▼]	RDI[ρ]	Dip (°)[ξ]	d_0 (x+) (cm)[•]	d_0 (x-) (cm)[θ]	d_0/λ[α]	Migr. speed (cm/h)	Migr. Dir.[ι]	Time[◆]
S10R3	7.9	47.1	10.8	0.14	107.5	10.4	10.4	ALRr	2.5D	AS	2.09	0.56	17.2/27.0	139.3	122.9	1.3	31.5	d	5:00
S10R3[ς]	7.9	47.1	10.8	0.14	9.0	0.4	21.5	SSR	2D	S	-	-	7.1/7.0	-	-	-	-	-	"
S10R4	7.9	52.8	15.7	0.14	131.1	13.4	9.8	ALRr	3D	AS	4.09	0.66	4.8-16.3/27	194.1	95.1	1.5	27.2	d	2:35
S10R4[ς]	7.9	52.8	15.7	0.14	9.2	0.4	23.0	ASR	3D	AS	-	-	6.7/8.4	-	-	-	-	-	"
S10R5	8.0	51.3	23.9	0.14	135.3	13.4	10.1	ALRr	2D	AS	3.77	0.69	11.2/25.0	190.5	74.4	1.4	-	d	2:30
S10R5[ς]	8.0	51.3	23.9	0.14	12.8	0.7	18.2	ASR	3D	AS	-	-	8.5/9.8	-	-	-	-		"
S10R6	8.2	49.9	23.5	0.15	127.8	14.6	8.7	ALRr	3D	AS	4.13	0.60	10.3/30.8	208.3	85.5	1.6	31.7	d	4:40
S10R6[ς]	8.2	49.9	23.5	0.15	11.1	0.5	21.8	ASR	3D	AS	-	-	5.4/7.9	-	-	-	-	-	"
S11R1	7.9	75.4	0.0	0.14	131.6	13.0	10.1	SLRr	2.5D	S	1.10	0.38	14.6/14.3	188.7	193.8	1.4		ud	4:15
S11R2	8.0	68.6	6.1	0.14	140.9	15.0	9.4	ALR	2.5D	AS	1.85	0.49	11.0/22.8	207.5	176.2	1.5	18.3	d	4:00
S11R3	8.0	63.6	10.4	0.14	352.4	19.1	18.5	HM	2.5D	AS	9.0	0.95	4/26	211.4	159.2	0.6		d	4:50
S11R4	8.0	69.0	16.7	0.14	301.5	32.6	9.2	PL	2.5D	AS	-	-	-	203.6	160.5	0.7	34.2	d	2:50
S11R5	8.0	62.1	22.3	0.14	-	-	-	PL	-	-	-	-	-	174.9	116.2	-	-	d	1:50
S11R6	8.0	61.7	16.5	0.14	-	-	-	PL	-	-	-	-	-	-	-	-	-	-	2:00
S12R1	8.0	20.1	0.0	0.14	8.9	1.0	9.4	SSR	2D	S	-	-	-	53.5	50.9	6.0	-	ud	2:25
S12R2	7.9	20.7	5.1	0.14	10.2	1.2	8.8	SSR	2.5D	S	-	-	-	59.1	43.7	5.8	1.1	ud	2:45
S12R3	8.1	20.6	10.9	0.15	11.2	1.5	7.5	ASR	3D	AS	1.48	0.50	16.6/23.9	92.8	26.5	8.3	3.4	d	3:00
S12R4	8.1	20.6	16.4	0.15	11.0	2.9	3.8	ASR	3D	AS	1.64	0.58	16.9/27.4	99.4	10.6	9.0	11.5	d	3:00
S12R5	8.0	20.6	21.5	0.14	13.8	1.8	7.8	ASR	3D	AS	1.44	0.51	19.1/25.1	129.2	2.6	9.4	28.5	d	2:10
S13R1	10.7	145.8	0.0	0.22	723.8	53.2	13.6	RLRr	2.5D	AS	-	-	-	-	-	-	-	d	5:00
S13R2	10.5	87.1	0.0	0.21	209.8	28.0	7.5	RLRr	2.5D	AS	1.33	0.55	20.3/29.0	274.7	293.4	1.3/1.4	62.5	Ud	7:30
S13R3	10.8	80.4	4.9	0.23	186.6	19.9	9.4	HMr	3D	AS	1.28	0.48	16/18	orbit.	-	orb.	-	Ud	4:00
S13R4	10.8	75.3	16.8	0.23	221.9	30.1	7.4	ALR	2D	AS	2.41	0.56	4.8-14.8/28.6	387.0	192.2	1.7	39.1	d	2:30
S13R5	10.8	73.5	20.2	0.23	206.5	26.4	7.8	ALR	2D	AS	2.6	0.56	4.7-13/26.2	357.8	172.3	1.7	35.6	d	1.00
S13R6	10.8	75.0	10.1	0.23	192.8	26.2	7.3	HMr	2.5D	AS	2.09	0.60	12.7/24.4	344.6	291.6	1.8/1.5	71.3	u	3:00
S14R1	10.7	165.3	0.0	0.22	-	-	-	PL	-	-	-	-	-	-	-	-	-	-	3:00
S14R2	10.7	127.4	0.0	0.22	-	-	-	PL	-	-	-	-	-	-	-	-	-	-	-
S14R3	10.7	113.7	0.0	0.22	-	-	-	PL	-	-	-	-	-	-	-	-	-	-	-
S15R1	10.7	114.3	0.0	0.22	347.4	41.3	8.4	RLR	2D	AS	0.61	0.46	30/15	-	-	-	39.6	d	2:30
S15R2	10.8	116.0	0.0	0.23	358.1	42.5	8.4	RLR	2D	AS	-	-	-	-	-	-	118.4	d	6:30
S15R3	10.9	120.1	5.6	0.23	337.7	39.9	8.5	RLR	2D	AS	1.38	0.64	4-14/26	498.2	363.5	1.5/1.1	30.1	u	5:20
S15R4	10.9	118.6	11.9	0.23	525.1	41.7	12.6	RLR	2D	AS	-	-	-	-	-	-	79.9	u	1:50
S15R5	10.8	116.4	23.0	0.23	440.7	39.6	11.1	ALR	2D	AS	5.05	0.73	4/29	-	-	-	324.1	d	0:30
S16R1	10.6	37.7	0.0	0.22	10.8	1.2	9.3	SSR	3D	S	0.81	0.44	15.3/11.8	154.5	136.8	14.4	-	ud	4:00
S16R2	10.7	35.9	9.2	0.22	10.9	1.2	9.2	ASR	3D	AS	1.27	0.50	12.3/16.2	176.1	87.4	16.1	21.5	d	4:00
S16R3	11.0	38.7	23.0	0.23	198.6	14.2	14.0	ALRr	3D	AS	3.41	0.76	4-22/31.3	393.6	33.9	1.98	52.3	d	4:45
S17R1	10.6	28.1	0.0	0.22	-	-	-	SSR	2.5D	S	-	-	-	-	-	-	-	-	-
S18R1	10.7	62.8	0.0	0.22	149.4	15.0	9.9	SLRr	3D	AS	0.97	0.47	19/17	221.1	225.0	1.5		ud	4:30
S18R2	11.0	67.8	5.8	0.23	153.0	16.3	9.4	SLRr	2.5D	AS	1.60	0.43	13.7/20.4	289.1	217.2	1.9	46.5	ud	7:00
S18R3	11.0	53.5	12.2	0.23	148.5	34.6	4.3	ALRr	2.5D	AS	2.57	0.46	10.7/26.6	229.4	188.7	1.5/1.3	70.9	Ud	5:00
S18R4	10.7	57.1	19.8	0.22	217.3	26.4	8.2	ALRr	2D	AS	3.79	0.60	9.7/30.6	308.5	84.8	1.4	73.6	d	3:25
S18R5	10.8	74.5	0.0	0.23	224.0	27.2	8.2	HMr	3D	AS	-	-	-	-	-	-	-	-	5:10

Table 2.2 Morphological attributes of small-scale and large-scale oscillatory-flow, combined-flow, and unidirectional-flow bed forms

KEY: U_0, oscillatory velocity; U_u, unidirectional velocity; λ, bed form wavelength; 2D, two-dimensional; 2.5D, locally 2D and locally 3D; 3D, three-dimensional; *, with the exception of one run; fsa, fine sand; N/A, not applicable

NOTES: 1) oscillatory-flow and combined-flow data is compiled from the various grain size and oscillation period conditions explored in this study. Unidirectional-flow data is generalized from the literature or specifically from cited sources.

2) Symmetry, roundness and ripple indices are defined in Figure 2.2.

Table 2. Morphological attributes of small-scale and large-scale oscillatory-flow, combined-flow, and unidirectional-flow bed forms

SMALL-SCALE BED FORMS: λ < 20 cm	< 40 cm/s + ~ 0-4 cm/s 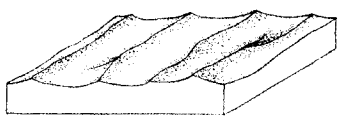 20 cm	< 40 cm/s + ~ 5-10 cm/s 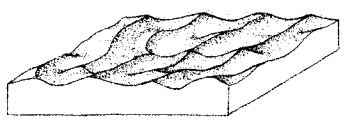 20 cm	< 40 cm/s + > 10 cm/s 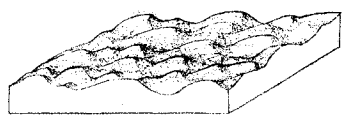 20 cm	0 cm/s + > ~ 10 cm/s 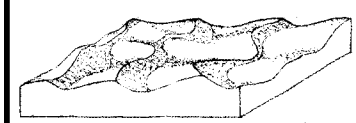 20 cm (adapted from Harms et al. 1982, fig.3.7a)
Bed form	**Symmetric small ripples (SSR)** regular, 2D, symmetrical, sharp crests, straight flanks, broad troughs	**SSR + asymmetric small ripples (ASR)** more irregular, 2-2.5D, still symmetrical rounder crests, some straight and some biconvex flanks	**ASR + asymmetric large ripples** irregular, 3D, asymmetrical, larger λ and height, round biconvex profiles, pronounced scour on lower end of stoss	**Current ripples** very irregular, 3D, sharp crests, steep and straight lee, convex-up stoss
Symmetry index	~1.2	~ 1.5		5-10 (Yokokawa 1995)
Dip of lee side	11-18°		*24-27 ° dip of lee side increases with increasing Uu	~ angle of repose (30-35°)
Roundness index	0.44	~ 0.50	> 0.50	0.5-0.6 (Yokokawa 1995)
Ripple index	generally between 8-12 for all bed forms			12-22 (Harms, 1969) 7-20 (Allen, 1982) 6-11, fsa (Yokokawa 1995) ~ 20, fsa (Boggs, 2000)
Orbital diameter/ wavelength	8-15	~ 8-15	8-15	N/A

LARGE-SCALE BED FORMS: λ > 100 cm	40-100 cm/s + ~ 0-4 cm/s 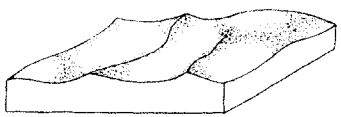 150 cm	40-100 cm/s + ~ 5-10 cm/s 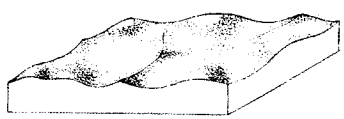 150 cm	40-100 cm/s + > 10 cm/s 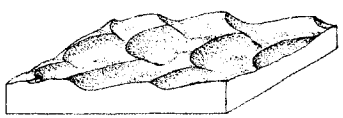 150 cm	0 cm/s + > ~ 40 cm/s 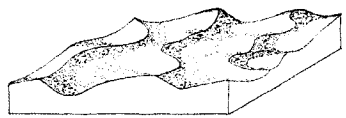 150 cm (adapted from Harms et al. 1982, fig.3.10)
Bed form	**Symmetric large ripples (SLR)** SLR: 2.5D, symmetrical, sharp discontinuous crests = to brink, straight flanks	**Hummocky (HM) + SLR + ALR** HM: 3D, symmetrical, no brink point, broad round crests, domal, convex-up flanks	**Asymmetric large ripples (ALR)** ALR: 2D-3D, asymmetrical, brink not always = to crest, round stoss with break in slope, can have scour pits on lower end of stoss	**Dunes** regular (2D) to irregular (3D), sharp crests, steep and straight lee, straight to convex-up stoss
Symmetry index	~ 1.0 (≤ 1.5)	≤ 2	> 2	–
Dip of lee side	14-24° (SLR), 15-29° reverse large ripples (RLR)		*23-31° dip of lee side increases with increasing Uu	~ angle of repose (30-35°)
Roundness index	~ 0.40-0.50 highest for HM bed forms	~ 0.45-0.60	~ 0.55-0.75 (up to 0.95)	–
Ripple index	generally between 8-12 for all bed forms			12-22 (Harms, 1969) 20-40 (Allen, 1985) ~ 5, fsa (Boggs, 2000)
Orbital diameter/ wavelength	1-2	1-2	1-2	N/A

CHAPTER 3

AGGRADATION RATE AND UNIDIRECTIONAL CURRENT AS CONTROLLING VARIABLES IN THE FORMATION OF HUMMOCKY AND SWALEY CROSS-STRATIFICATION

INTRODUCTION

Hummocky cross-stratification (HCS) and swaley cross-stratification (SCS) have been widely recognized in the shallow marine rock record, and generally are thought to indicate deposition under storm conditions on continental shelves (e.g., Cheel and Leckie 1993; Dott and Bourgeois 1982; Duke 1985; Harms et al. 1982; Leckie and Krystinik 1989; Swift and Figueiredo 1983; Walker et al. 1983). However, a number of important issues regarding the origin of HCS and SCS remain unresolved, namely the mechanism that transports sand into the area of HCS and SCS deposition, where along a shelf profile and under what type of flow do they form, and by what process(es) are they generated? Recent experimental work (Arnott and Southard 1990; Dumas et al., in review) in addition to data on storm sedimentation and flow conditions from modern continental shelves might help gain insight into some of these unresolved issues.

This study proposes to test two hypotheses. First, that an increase in aggradation rate increases the likelihood of forming HCS (vs. SCS). In addition to simple geometric evidence, this is also based on the premise that during a storm depositional rates must increase basinward as sediment-laden flows experience both spatial and temporal deceleration (Snedden et al. 1988). Second, that in the presence of strong oscillatory flows, the addition of a weak unidirectional flow (above a few cm/s) causes a decrease in

the likelihood of forming HCS and SCS, and instead favors the formation of high angle, large-scale trough cross-stratification and planar lamination.

HUMMOCKY AND SWALEY CROSS-STRATIFICATION

HCS was first described by Harms et al. (1975) as gently dipping (< 15°), cross-stratification in coarse silt to fine sand characterized by the presence of both hummocks (convex-up, meter spacing, decimeters high) and swales (convex-down), and by an erosional lower contact. Internal lamination is nearly parallel but can also fluctuate in dip giving a fan-like appearance (Fig. 3.1A and Fig. 3.2A; 3.2B). Low-angle truncation surfaces are common and can become conformable when traced laterally. Cross-strata dip directions are scattered, and the structure is isotropic in three dimensions.

Beyond the general consensus on the storm origin of HCS, opinions differ on the type of flow under which it forms. Some interpret HCS to be the result of wave reworking of previously deposited sediment with subsequent fallout and draping of the erosional topography (e.g., Dott and Bourgeois 1982; Walker et al. 1983). Others, on the other hand, think that unidirectional currents play a dominant role (e.g., Allen 1985; Greenwood and Sherman 1986; Swift and Nummedal 1987), whereas most believe in a combined wave-current origin for HCS (e.g., Allen 1993; Arnott and Southard 1990; Cheel and Leckie 1993; Duke 1987; Duke et al. 1991; Higgs 1990; Leckie and Krystinik 1989; Midtgaard 1996; Molgat and Arnott 2001; Nottvedt and Kreisa 1987). In 1996, Myrow and Southard conceptually unified these different viewpoints by suggesting that HCS could originate from either geostrophic currents, waves, or density currents, or any in combination. Furthermore, the characteristic low-angle stratification has been suggested to indicate conditions of multispectral oscillatory flow, or where unidirectional flows and oscillatory flows are oriented at high angles (Greenwood and Sherman 1986; Swift and Figueiredo 1983), or where deposition occurred under high suspended-sediment concentrations (DeCelles and Cavazza 1992). Another controversial but also pivotal issue is the mechanism by which sand is transported to the area where HCS

forms. Opinion is split between the shore-parallel to shore-oblique geostrophic currents measured in modern environments (e.g., Dott and Bourgeois 1982; Duke et al. 1991; Greenwood and Sherman 1986; Hart et al. 1990; Leckie and Krystinik 1989; Swift and Figueiredo 1983), and the shore-normal shelf turbidity currents inferred from the ancient shallow-marine sedimentary record (e.g., Higgs 1990; Myrow et al. 2002; Walker 1984; Walker et al. 1983). Duke et al. (1991) attempted to reconcile these differences and proposed a model in which the shore-oblique bottom unidirectional current combines with the shore-normal, high-velocity wave component of long-period storm waves to create a shore-normal peak instantaneous bed shear stress responsible for offshore sediment transport. The mechanism by which HCS forms is yet another source of debate. Some believe HCS to be more of a scour and passive drape type of sedimentary structure (e.g., Dott and Bourgeois 1982; Harms et al. 1982; Midtgaard 1996), whereas others envision an equilibrium bed form to be at the origin of HCS (e.g., Arnott and Southard 1990; Duke et al. 1991; Leckie 1988; Nottvedt and Kreisa 1987; Swift and Figueiredo 1983; Walker et al. 1983). Amongst those who believe HCS to originate from a migrating bed form, most consider HCS to form just below the threshold for oscillatory and combined-flow upper plane bed (e.g., Greenwood and Sherman 1986; Nottvedt and Kreisa 1987; Swift and Figueiredo 1983; Dumas et al., in review). Alternatively, others envision HCS to be a wave-influenced equivalent of unidirectional-flow upper plane bed (Dott and Bourgeois 1982). The above suggested genetic conditions help in speculating about potential depositional environments where hummocky cross-stratification could form. HCS was originally proposed to form between fairweather and storm wave bases in open marine environments (Dott and Bourgeois 1982). Since then HCS has been reported in fetch-limited settings (e.g., Eyles and Clark 1986; Greenwood and Sherman 1986), at depths as shallow as the surf zone and foreshore (DeCelles and Cavazza 1992; Greenwood and Sherman 1986, Yang et al., 2002), and even in the non-marine

record (Gibling and Rust 1993). However, the recognition of some of these sedimentary structures as HCS might involve some modifications to the original definition. For example, the introduction of such terms as micro HCS (wavelength ~ 10 cm) and small-scale HCS (wavelength ~ 30 cm) diverge from the original intent of describing a large-scale feature most likely formed by large storm waves.

The term SCS was introduced by Leckie and Walker (1982) to describe "a series of superimposed concave-upward shallow scours about 0.5-2 m wide and a few tens of centimeters deep" found in fine to medium sandstone (Fig. 3.1B and Fig. 3.2C; 3.2D). In addition, basal surfaces are erosive, laminae rarely dip more than 10°, and the structure is isotropic in three dimensions.

Although SCS has been less frequently reported than HCS in the literature, because of their stratigraphic relationship and morphological similarities they are generally thought to be genetically related (Duke 1985; Leckie and Walker 1982; Tillman 1986; Walker 1982). For example, Walker (1982) stated that: "SCS could be described as amalgamated HCS, but without the hummocks". For this reason, the debate surrounding the origin of SCS is much the same as that for HCS. The small number of attempts that do speculate on the environmental significance of SCS generally agree with the original model proposed by Leckie and Walker (1982), where SCS, found above HCS but below beach deposits, is thought to form between fairweather and storm wave bases on storm-dominated shorefaces (e.g., Arnott 1992; Duke 1985; Plint and Walker 1987; Tillman 1986; Walker 1982). However, Allen and Underhill (1989) suggested that SCS is produced primarily by unidirectional flows with high suspended-sediment loads and warn against the use of this sedimentary structure as an indicator of storm conditions on the shoreface.

METHODS

Experiments were conducted in a 15 m long combined-flow tunnel with a 1.20 m wide by 0.65 m deep cross-section (Fig. 3.3) capable of generating long oscillatory period (T = 7 and 9.4 s), high oscillatory velocities (U_0) (up to 125 cm/s), and moderate colinear unidirectional velocities (U_u) (0-25 cm/s) (see Chapter 2). The objective was to study equilibrium oscillatory and oscillatory-dominant combined-flow bed forms, with special interest focused on hummocky bed forms (Fig. 3.4). Flow conditions and sediment size (0.11 and 0.17 mm) were chosen to be representative of conditions observed in the rock record and experienced on continental shelves during storms (see Table 3.1). The dataset consisted of 18 series of experiments each comprising several runs (totaling 76). An experimental series comprised a preselected oscillatory period and oscillatory velocity onto which a progressively higher colinear unidirectional velocity was superimposed; each combination of U_0 and U_u formed a run. The experimental strategy was then repeated twice: first changing the wave period and then the grain size. Because of the limitations of the apparatus, no new sediment was added during a run. As a consequence, to test the effect of a weak unidirectional flow on large-scale (wavelength > 1 m) oscillatory-flow hummocky bed form stratification, the bed was aggraded using a synthetic aggradation technique (Southard et al. 1990). Stratification was generated by sequentially stacking 24 sidewall bed surfaces taken in five-minute intervals, and erasing any segments (truncation) that lay above later bed traces. The total running time was 115 min at an aggradation rate of the order of 1 mm/min. In addition, to test the effect of an increase in simulated aggradation rate, a single representative hummocky bed profile trace was selected from the oscillatory profile described above, and aggraded at rates of 1 mm/min and 4.2 mm/min. Although the aggradation rate varied, the upstream (against the U_u or onshore direction) and

downstream (same direction as U_u or offshore direction) horizontal bed form migration rate was kept constant at 6 mm/min. This migration rate was selected based on observed hummock migration behaviour during oscillatory-flow runs at U_0 = 75 cm/s. Under these conditions hummocks were observed to migrate back and forth about a central position moving ~ 20 cm per half hour (or ~ 6 mm/min) in one direction before reversing and migrating a similar distance in the opposite direction. This horizontal onshore/offshore bed form movement was then combined to the imposed vertical aggradation rates of 1 mm/min and 4.2 mm/min to form vertical sinusoidal paths of migration and aggradation.

EFFECT OF AGGRADATION RATE ON CROSS-STRATIFICATION

Figure 3.5 shows the effect of aggradation rate on cross-stratification. At the lower aggradation rate of 1 mm/min (Fig. 3.5A and 3.5C; top frame), bed form troughs are preferentially preserved and hummocks selectively eroded. The stratification style is similar to SCS with characteristic broad low-angle swales, and uncommon convex-up laminae. However, Fig. 3.5A displays much less of the nearly horizontal, sub-parallel lamination described by Leckie and Walker (1982). This might be explained by the somewhat "unnatural" sinusoidal path of migration and aggradation imposed on the bed form, and accordingly characteristic of deposition. Although the sinusoidal path simulates the movement of a fixed configuration of hummocks and swales, it does not account for cases where hummocks spontaneously grow from swales and vice-versa, a phenomenon commonly observed in the lab (Dumas et al., in review), and associated with a transitional phase of nearly-horizontal, sub-parallel stratification. When the aggradation rate is increased to 4.2 mm/min (Fig. 3.5B and 3.5C; bottom frame),

hummocks are better preserved, and as a consequence the average dip angle of the cross-stratification increases. The resulting stratification bears a striking resemblance to HCS where hummocks and swales are equally represented with meter-scale spacing and decimeter-scale relief. In addition, as is characteristic of HCS, conformable laminae become unconformable when traced laterally, and changes in dip angles give the stratification a fan-like appearance. Average cross-strata dip angles are within the typical HCS range of less than 15°, although locally they can be higher. In addition, although it is not possible to convey in a 2D profile, the stratification (for both aggradation rates) is postulated to have the same aspect regardless of orientation. This is a reflection of the isotropic migration behaviour of hummocks observed in the laboratory.

For both aggradation rates, the best hummock preservation potential is associated with bed forms having biconvex flanks and broad "dome-like" crests (see Fig. 3.5A). For example, in Fig. 3.5A none of the crests of the straight flanked, narrow-crested ripples are preserved and the few hummocks (or portion of hummocks) preserved all originate from the broad-crested bed forms.

EFFECT OF A UNIDIRECTIONAL CURRENT ON CROSS-STRATIFICATION

Figure 3.6 illustrates the effect of a colinear unidirectional flow of 5 cm/s superimposed on an oscillatory flow of 75-80 cm/s. Stratification in both profiles displays many of the diagnostic characteristics of HCS outlined by Harms et al. (1975) (refer to Fig. 3.6). However, the stratification from the oscillatory-flow run (Fig. 3.6A) is isotropic (i.e. it shows no preferred direction of dip), whereas the combined-flow run stratification (Fig. 3.6B) is more anisotropic despite an approximately symmetrical surface morphology. This anisotropy results from preferential deposition on the bed form's lee

side, and as a consequence, the bed form migrates, albeit slowly, downstream. This supports earlier work that suggested that the addition of only a small unidirectional current (a few cm/s) to an intermediate oscillatory flow (~ 50-90 cm/s) causes bed forms to become anisotropic (Arnott and Southard 1990). With further increase in unidirectional velocity bed forms become distinctively asymmetric with a steeper downstream-dipping lee face that generates higher-angle large-scale cross-stratification (compare Fig. 3.4D and 3.4F). For a unidirectional current greater than about 10 cm/s, crests become sharper, foresets straight (rather than sigmoidal) and dip angle of lee face increases to angle-of-repose. The resulting stratification is expected to resemble unidirectional-flow dune cross-stratification rather than hummocky cross-stratification. For this reason, it was judged unnecessary to pursue the synthetic aggradation experiments (Fig. 3.6) beyond a unidirectional current of 5 cm/s.

DEPOSITIONAL MODEL

Figure 3.7 compares idealized flow parameters and depositional features for fairweather and storm conditions on a storm-dominated shelf. It is a highly simplified model with the intention of showing a generalized hypothetical progression of stratification styles across a wave-influenced shelf profile. In the context of this paper, shelf is defined as the portion of the continental margin that is between the shoreline and the continental slope (Jackson 1997) and, therefore, includes the shoreface. During fairweather bottom shear stress is below the threshold for fine sand movement, and as a consequence, sediment movement is limited to depths on the shoreface, commonly about 10 m or less (Snedden et al. 1988). Sand transport is mainly related to the

onshore portion of the asymmetric orbital motion of shoaling waves (Clifton 1976), and near-bottom unidirectional currents are weak to absent.

Near fairweather wave base, small-scale ripple stratification results from the small-diameter, near-symmetric wave orbital motion (Clifton 1976). Shoreward wave orbital asymmetry develops and progressively increases as frictional resistance with the shoaling bottom increases. This asymmetry is indicated by onshore-dipping, high-angle cross-stratification formed under these shoaling waves (Clifton 1976). At the shoreward limit of wave influence, the swash zone, high velocity fluid flow and shear stress associated with breaking waves create sheet-flow conditions forming planar lamination (Clifton 1976). Consequently, suspended-sediment concentration peaks around the wave breaking area of the surf zone and decreases rapidly basinward.

In contrast, during storms, unidirectional currents and waves can combine to transport significant volumes of sediment offshore. Geostrophic flows resulting from the balance between the coastal set-up pressure gradient and Coriolis effects are approximately shore-parallel over much of the flow depth, but due to bottom friction, currents are oriented in a more shore-normal direction very close to the bed (Snedden et al. 1988; Swift and Figueiredo 1983) (see Fig. 1.4). Other unidirectional current generating mechanisms have also been proposed, including rip currents (e.g., Swift and Figueiredo 1983), and density flows (e.g., Myrow et al. 2002; Walker et al. 1983). Also, nearshore tidal currents, although a long period (measured in hours) wave phenomenon, can influence sediment transport as a regularly reversing unidirectional flow. Table 3.1 presents examples of storm sedimentation and flow parameters as measured on modern continental shelves. The data suggest that unidirectional currents can assume a wide range of values and that current speeds do not decrease uniformly with depth. In addition to unidirectional currents, storm events create strong oscillatory flows generated by large, long-period waves that have been reported to affect the bottom up to depth of ~

200 m (Walker 1984); oscillatory velocities of nearly 60 cm/s have been measured in water 80 m deep (see Table 3.1). Furthermore, it is now widely recognized that the addition of a unidirectional current to an oscillatory flow results in greatly enhanced boundary shear stress due to the nonlinear wave-current interaction in the combined-flow bottom boundary layer (e.g., Duke 1990; Grant and Madsen 1979; Li et al. 1997; Manighetti and Carter 1999; Morton 1988; Smith 1977). Strong combined-flow shear stresses associated with storms commonly suspend significant amounts of sediment, with measured sediment concentrations as high as 4 g/l (Table 3.1). According to Swift et al. (1983 based on data from Vincent et al. 1982), up to 20 cm of sand can be deposited during a single storm event. This implies that aggradation rates of 1 mm/min and 4.2 mm/min (as illustrated in Fig. 3.5) deposit a 20 cm thick bed in 3h20min to just under 1h, respectively. These time frames seem plausible in the context of deposition of discrete storm beds on continental shelves where storm influence can last from hours to days (e.g., Hill, personal communication 2003; Madsen et al. 1993; Morton 1988), but where the depositional window of SCS and HSC represents only a fraction of the total storm duration. On shallower parts of the shoreface, however, estimating the duration of deposition from bed thickness (at a given aggradation rate) is made more difficult because of incomplete preservation and bed amalgamation.

During storms, sediment is typically stripped from the upper shoreface, transported offshore, and deposited as sediment-laden flows experience both spatial and temporal deceleration (Swift and Figueiredo 1983). Because of the lag between forces acting at the bed and bed response, areas experiencing the highest shear stress do not necessarily correspond to the areas of highest suspended-sediment concentration (Sherwood et al. 1994). This implies that sedimentation rates are not necessarily highest in areas where combined flows are at their peak (i.e. on the shoreface). Instead maximum sedimentation most probably occurs where flows become

most highly charged with suspended-sediment and start to decelerate (i.e. seaward of the shoreface). Furthermore, although the preservation potential of sedimentary deposits increases basinward and probably reaches a maximum below storm wave base, deposits consisting of sand are most likely thickest between fairweather and storm wave base where suspended-sand concentration levels are high, transport rates relatively low, and reworking during fairweather conditions rather unlikely. As a consequence, given the interplay between sediment supply and likelihood of deposition and preservation, optimal HCS conditions occur just above storm wave base. Here, sediment supply, although lower than further shoreward, is more than compensated by limited reworking and consequent high preservation potential. In contrast, SCS is expected to form shoreward of HCS, where suspended-sediment concentrations are higher but net aggradation rates are lower because of comparatively higher sediment transport rates. In addition, more frequent and extensive reworking, and consequently lower preservation potential is responsible for amalgamated deposits commonly associated with SCS. These conditions are consistent with the depositional setting and thickness of HCS and SCS strata reported in the literature (e.g., Arnott 1992; Duke 1985; Leckie and Walker 1982; Tillman 1986; Walker 1982).

In a transect from the shallow shelf to nearshore, and in light of the above proposed genetic constraints, isotropic HCS would form just above storm wave base under long-period high oscillatory to oscillatory-dominant ($U_u \sim \leq 5$ cm/s) combined flows and under relatively high suspended sediment fall-out rates fueling the high aggradation rates needed for hummock preservation (Fig. 3.5B). In addition to its hummocks and swales, low dip angles, and characteristic truncation surfaces, isotropic HCS could be recognized by its symmetry and its non-preferential dip direction. At slightly shallower depth, the influence of slightly higher near-bottom cross-shore unidirectional current ($\sim \leq$ 10 cm/s) would likely favor the formation of anisotropic HCS (Fig. 3.6B). The asymmetric

nature of the stratification and display of a preferred dip direction could help differentiate anisotropic HCS from isotropic HCS. Further up the shoreface, the lower aggradation rate required for the formation of SCS (see Fig. 3.5C) can be explained by a higher transport to deposition ratio associated with a more shore-proximal location. Note that, for simplicity, the effect of aggradation rate on the likelihood of forming of SCS compared to HCS was studied under conditions of pure oscillatory flow (Fig. 3.5), and consequently, the resulting synthetic stratification was isotropic. However, if the observed effect of aggradation rate holds under conditions of oscillatory-dominant combined-flows observed in nature, and given the effect of even a weak unidirectional current on cross-stratification dip direction and migration (see previous section), SCS generated on a natural shelf setting during a storm event is expected to be anisotropic. As suggested by the values of near-bottom U_u, SCS is likely to be of intermediate anisotropy and also bathymetry between anisotropic HCS and large-scale high-angle cross-stratification (Fig. 3.7). However, genetically, SCS is much closer to HCS, and could be described as truncated anisotropic hummocky cross-stratification. It is possible that upon closer look some of the SCS previously described as isotropic might reveal to be anisotropic. Still higher on the profile, the higher near-bottom offshore U_u (~ > 10 cm/s) would cause large-scale bed forms (if present) to migrate with the current, thus generating angle-of-repose large-scale cross-stratification much like unidirectional dune cross-stratification (Dumas et al., in review). Finally, at the most shoreward position of wave influence, breaking wave conditions in the surf and swash zones would form upper plane bed lamination.

CONCLUSIONS

A hummocky bed configuration was synthetically aggraded under conditions of long-period (~ 8-10 s), oscillatory-dominant combined flows (U_0 ~ 50-90 cm/s). An increase in aggradation rate increased the preservation of hummocks and as a result favored the formation of HCS. Conversely, at lower aggradation rate, swales were preferentially preserved and the resulting stratification was more akin to SCS. Based on experimental results, the addition of a unidirectional current of only ~ 5-10 cm/s to a moderate oscillatory flow (~ 50-90 cm/s) caused bed forms to migrate with the current and generated anisotropic (hummocky) cross-stratification showing a preferential direction of dip. With a further increase in unidirectional current (U_u > 10 cm/s) the low-angle hummocks evolved into downstream migrating asymmetric high-angle ripples generating large-scale angle-of-repose cross-stratification. These results are consistent with the earlier experimental work of Southard et al. (1990) and Arnott and Southard (1990), and suggest that some (much?) of the HCS observed in the rock record was generated by actively aggrading and migrating hummocky bed forms under long period (8-10 s), high oscillatory velocity (U_0 > 50 cm/s) and oscillatory-dominant combined flows ($U_u \leq$ 10 cm/s). Nevertheless, the latter is more likely, because the unidirectional flow component provides a mechanism to advect sediment offshore and into the area of deposition.

A simple depositional model is proposed to illustrate potential stratification style across a continental shelf under storm conditions. In a shoreward direction, isotropic HCS would occur at depth slightly above storm wave base where the near-bottom cross-shore unidirectional-flow component is minimal (~ ≤ 5 cm/s), aggradation rates are moderate, reworking is limited, and preservation potential maximized. Anisotropic HCS would follow under the influence of a slightly higher unidirectional flow (~ ≤ 10 cm/s),

succeeded by SCS at depth above fairweather wave base where higher transport to deposition ratio prevails, high-angle large-scale cross-stratification under more unidirectional-dominant combined flows, and finally planar lamination under sheetflow conditions in the surfzone and the foreshore.

Fig. 3.1 Original block diagrams illustrating the plan and cross-sectional morphology of hummocky cross-stratification and swaley cross-stratification. **A.** Hummocky cross-stratification (Harms et al. 1975). **B.** Swaley cross-stratification (Leckie and Walker 1982).

Ⓐ **Hummocky cross-stratification**

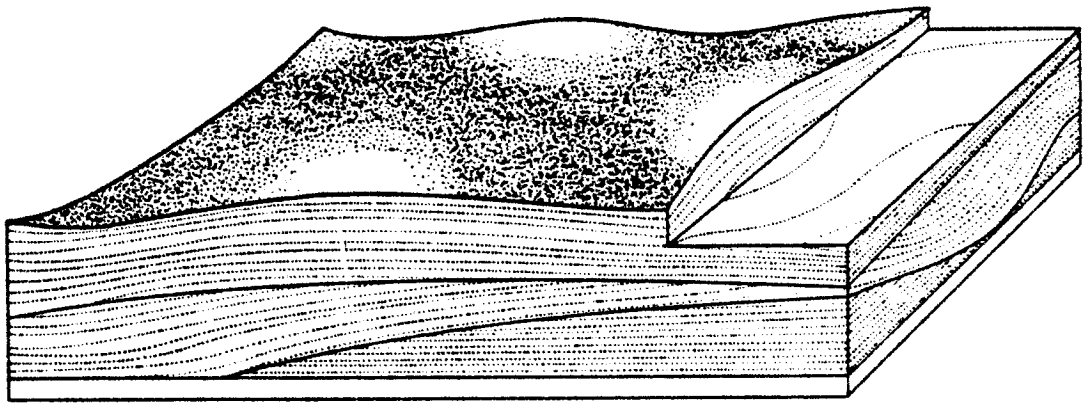

Ⓑ **Swaley cross-stratification**

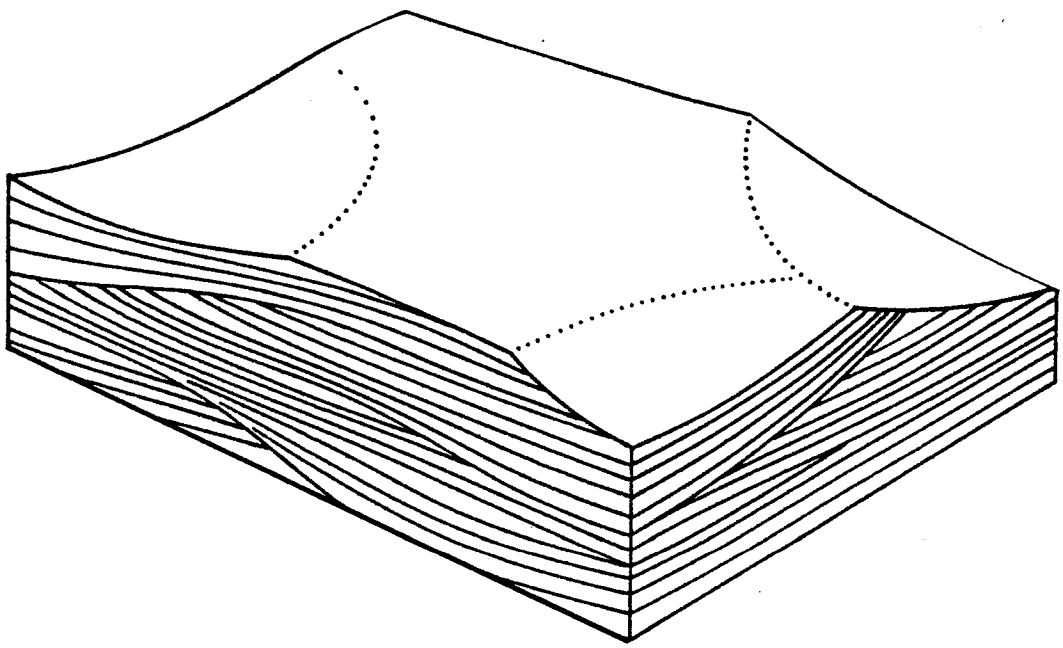

Fig. 3.2 HCS and SCS in outcrop. **A.** HCS, Book Cliffs, Utah, ruler for scale. **B.** HCS in Book Cliffs, Utah, pen for scale. **C.** SCS in Chungo Sandstone of the Wapiabi Formation, Alberta; compass for scale. **D.** SCS in Black Hawk Formation, Utah; ruler for scale.

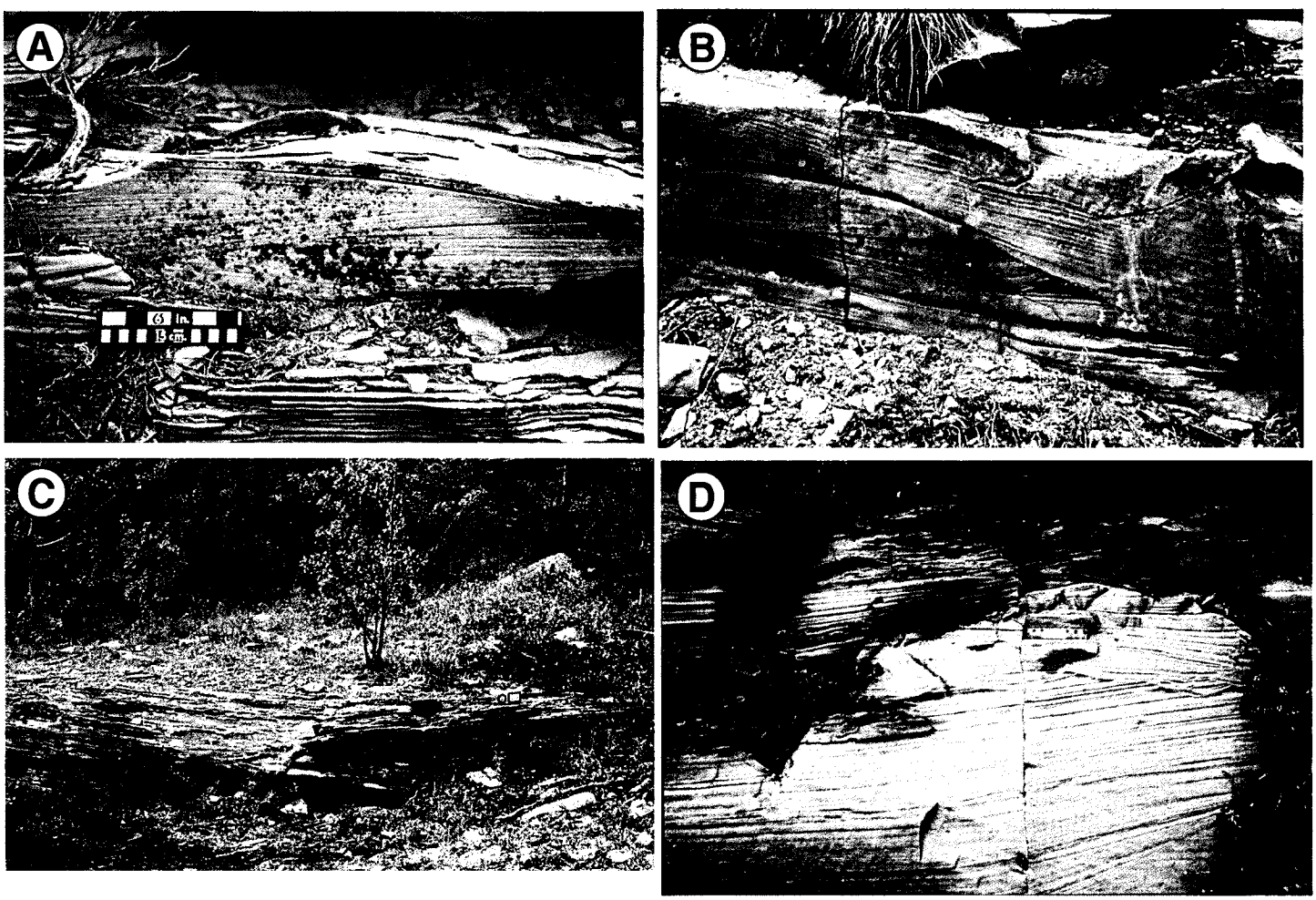
A
B
C
D

Fig. 3.3 Combined-flow tunnel. A bed of fine sand covers the entire horizontal floor of the tunnel. Bed forms are monitored through two observational side windows and from two ceiling openings (after the run is completed and the tunnel drained). Flow velocity was measured with an acoustic Doppler velocimeter (ADV).

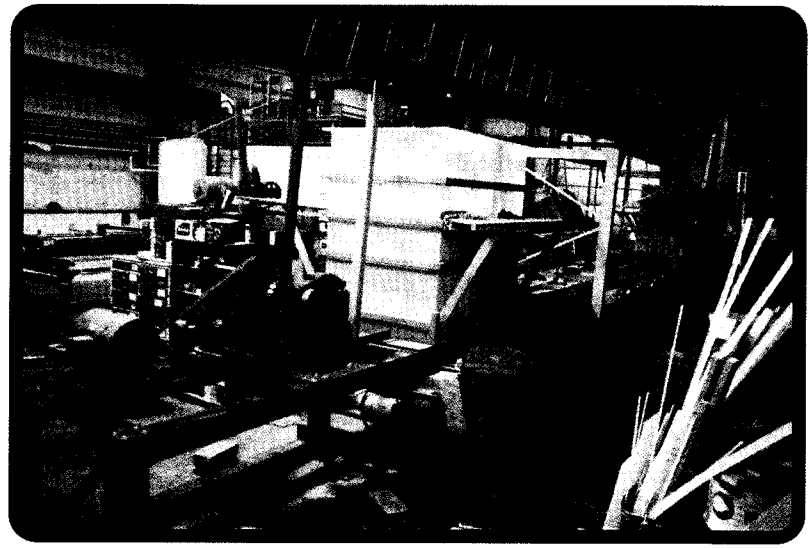

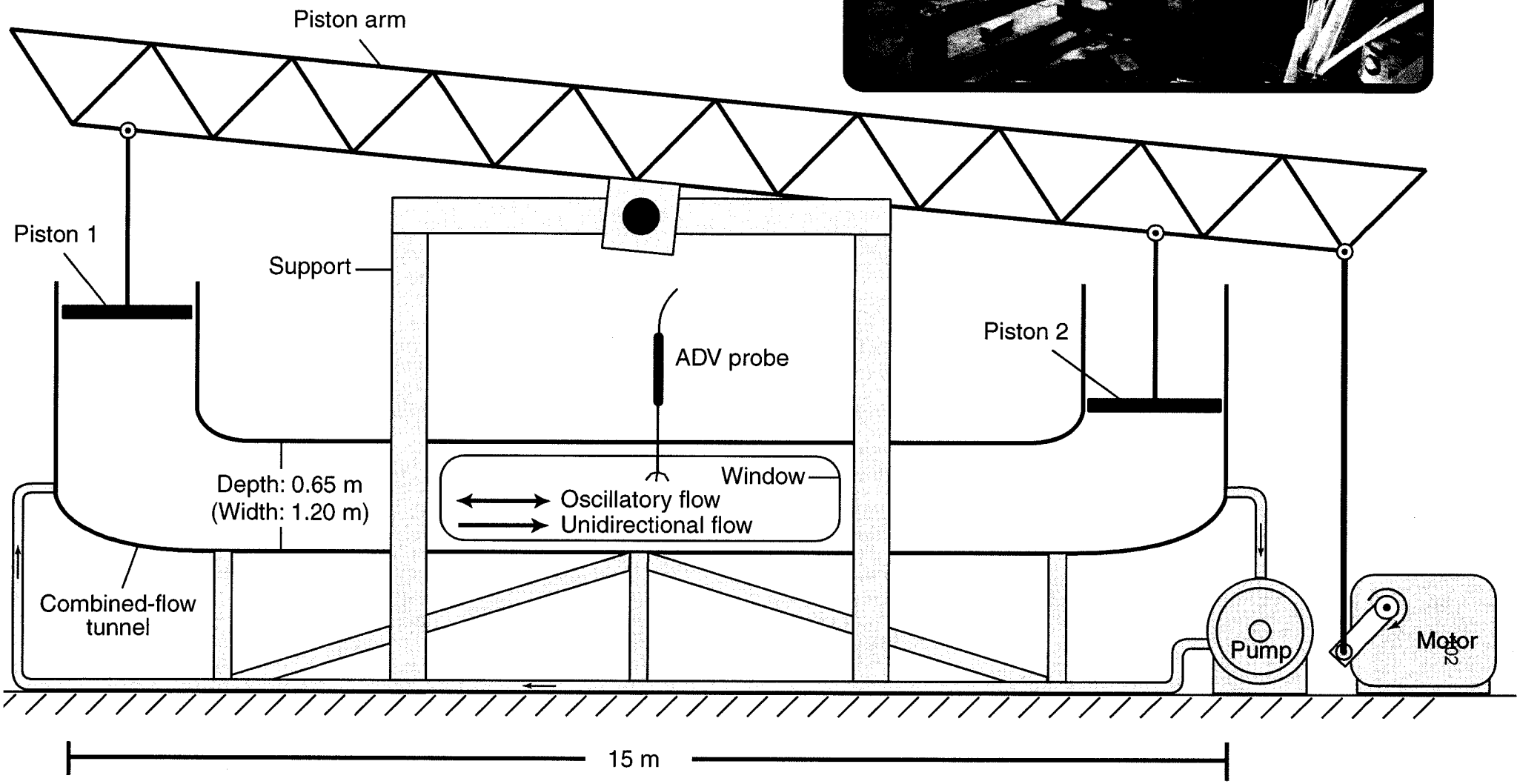
Piston arm
Piston 1
Support
ADV probe
Piston 2
Window
Depth: 0.65 m
(Width: 1.20 m)
Oscillatory flow
Unidirectional flow
Combined-flow
tunnel
Pump
Motor
15 m

Fig. 3.4 Hummocky bed forms generated in the laboratory. Scale bar divisions: 10 cm. Grain size: 0.11 mm (very fine sand). Unidirectional current is from right to left. **A, B.** Oscillatory velocity (U_0) is 45 cm/s, unidirectional velocity (U_u) is 0 cm/s, oscillatory period (T) is 7 s. Note the superimposed small-scale ripples. **C.** U_0 = 65 cm/s, U_u = 5 cm/s, T = 9.4 s. **D.** Close-up view of stratification in C; note the isotropic low-angle cross-stratification and bidirectionality of the dip direction characteristic of low U_u hummocky cross-stratification (HCS). **E.** U_0 = 65 cm/s, U_u = 10 cm/s, T = 9.4 s. **F.** Close-up view of stratification in E; note the anisotropic nature of the cross-stratification and single dip direction indicating migration with the unidirectional current. This stratification style is intermediate between anisotropic HCS (with its sigmoidal foresets and lee-face dip angle below angle-of-repose) and high-angle cross-stratification (with a uniform downstream dip direction).

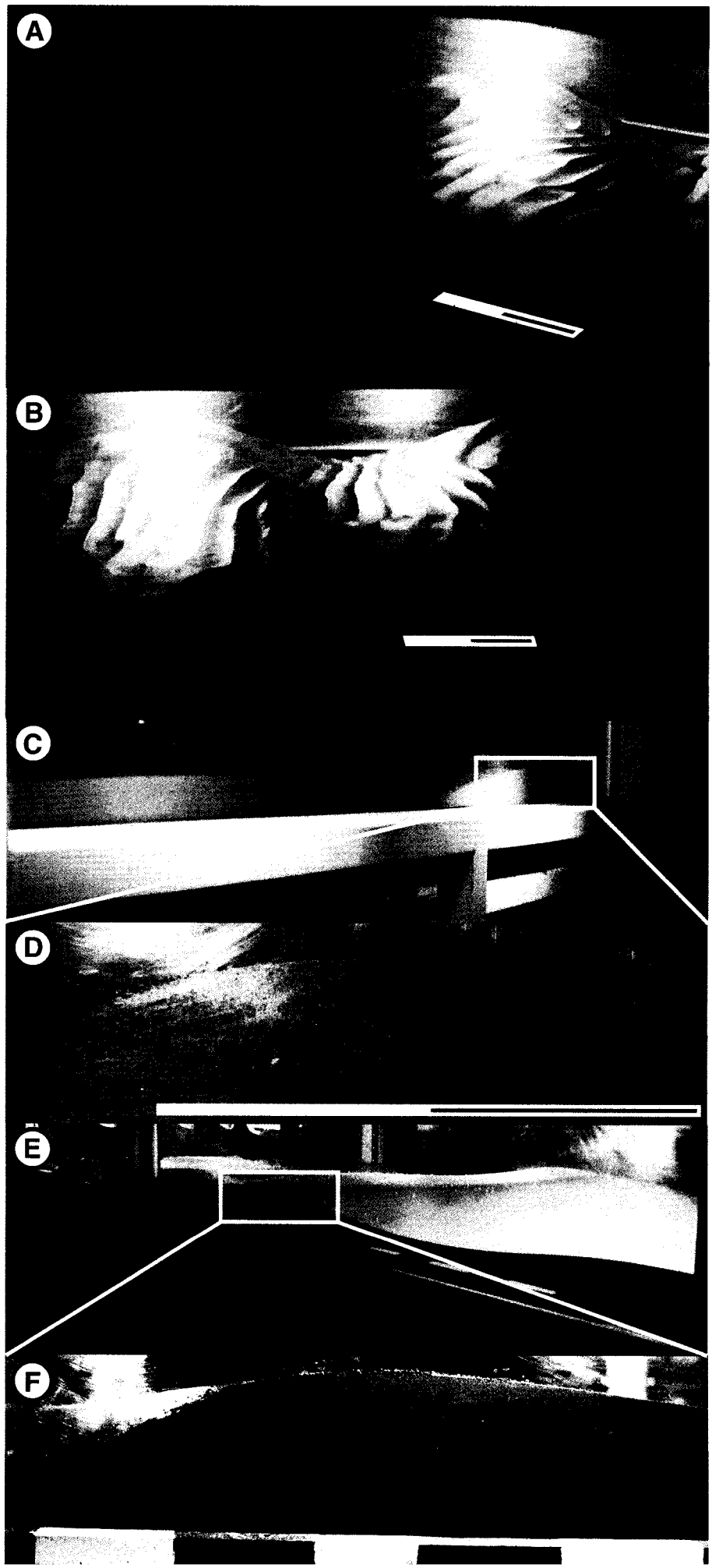
A
B
C
D
E
F

Fig. 3.5 Effect of aggradation rate on preservation potential of hummocks. Stacking of 32 bed profiles following a sinusoidal aggradation and migration path. Vertical and horizontal scales are equal. The profile was taken from an experimental run where oscillatory velocity (U_0) was 75 cm/s and unidirectional velocity (U_u) was 0 cm/s (Dumas et al. in review). Equilibrium bed forms during this run were meter-scale hummocky bed forms (biconvex flanks, round crests) and large ripples (straight flanks, sharper crests). The horizontal migration rate of 6 mm/min was chosen to be representative of the experimentally observed back and forth motion of bed forms when U_0 = 75 cm/s. **A.** 1 mm/min aggradation rate for a total aggradation time of 6h. **B.** 4.2 mm/min aggradation rate for a total aggradation time of 6h. **C.** Close-up views of the stratification generated in A and B highlighting the effect of aggradation rate. Both frames represent 3h of aggradation. Note the thinner deposit, lower average dip angle of cross-lamination, and the preferential preservation of swales with few hummocks at the lower aggradation rate (1mm/min). In contrast, the higher aggradation rate (4.2 mm/min) generates a thicker deposit, steeper average dip of cross-laminae, and good preservation of both hummocks and swales. Compared with sharp-crested straight-flank bed forms, broad-crested biconvex bed forms were associated with better hummock preservation potential and also were responsible for giving the stratification its characteristic domal and fanning appearance. Symmetry (or asymmetry) of a bed form is also reflected in the resulting stratification.

(A) 1mm/min aggradation rate

6h of aggradation following a sinusoidal path; time between each trace is 12 min; Uo = 75 cm/s and Uu = 0 cm/s

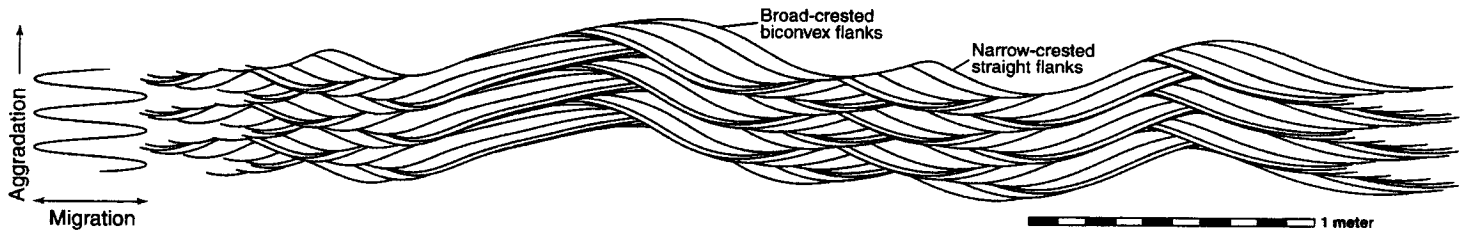

(B) 4.2 mm/min aggradation rate

6h of aggradation following a sinusoidal path; time between each trace is 12 min; Uo = 75 cm/s and Uu = 0 cm/s

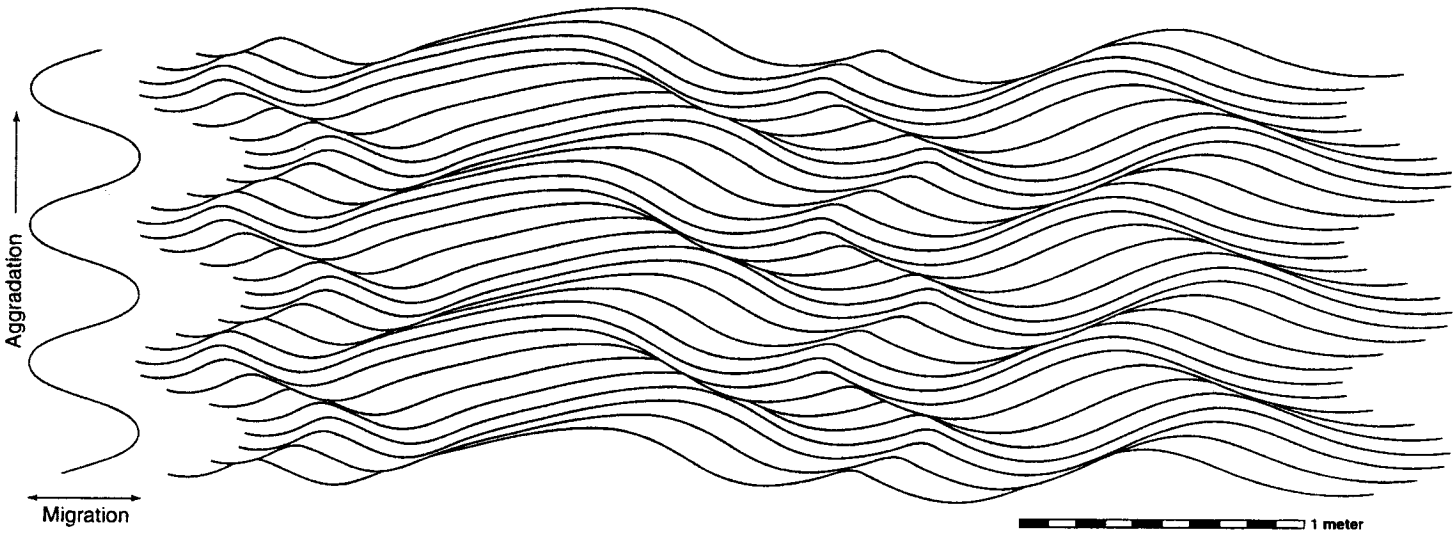

(C) Comparison of resulting stratification

Aggradation rate = 1 mm/min (3h of stratification displayed); swales preferentially preserved

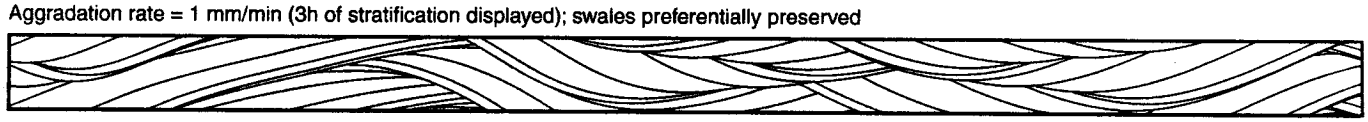

Aggradation rate = 4.2 mm/min (3h of stratification displayed); hummocks and swales equally represented

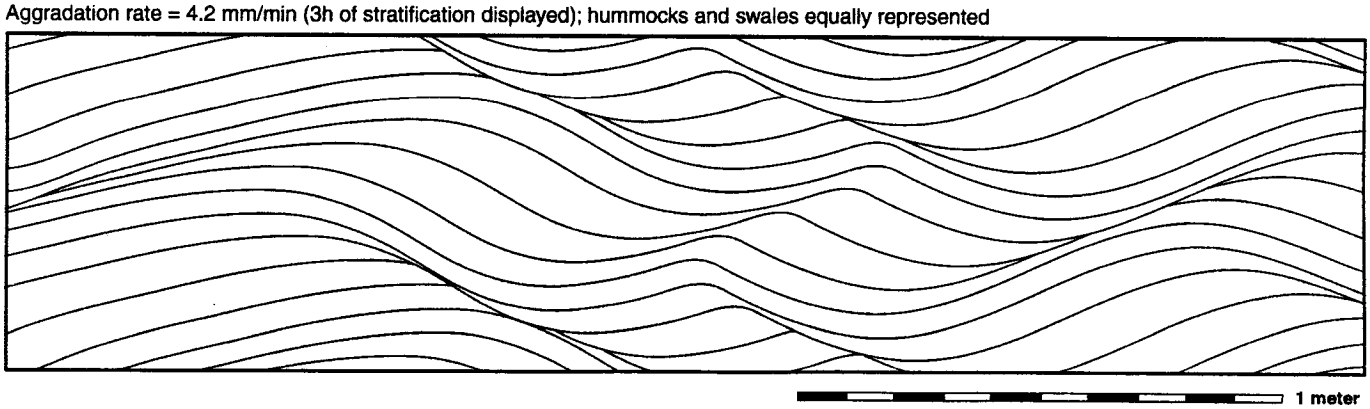

Fig. 3.6 Synthetic stratification. Time series of 24 bed profiles taken at five-minute intervals for a total running time of 115 min. Vertical and horizontal scales are equal. Current is from left to right. Conditions are scaled to 10° C. Run conditions are listed on diagram. The resulting stratification displays many of the diagnostic features of hummocky cross-stratification (HCS) as listed by Harms et al. (1975). (1) hummocks; (2) swales; (3) truncation surface become conformable when traced laterally; (4) thickening and thinning of laminae result in fan-like stratification and fluctuating dip; (5) locally laminae dips more steeply than the typical HCS range (< 15°). **A.** Pure oscillatory-flow run; note the bi-directional dip of the laminae and the common truncation surfaces characteristic of isotropic HCS. **B.** Oscillatory-dominant combined-flow run; note the preferred direction of dip of the cross-stratification related to bed form migration with the unidirectional current characteristic of anisotropic HCS.

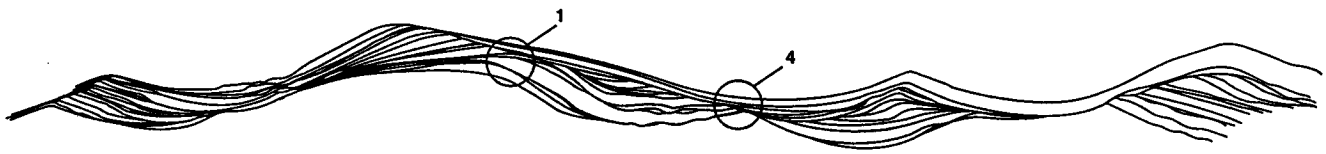

Ⓐ **Pure oscillatory flow**

S18R5
Uo = 75 cm/s
Uu = 0 cm/s
T = 10.8 s

grain size = 0.23 mm
wavelength = 224 cm
aggradation rate = 1.0 mm/min
equilibrium bed forms: SLR and HM

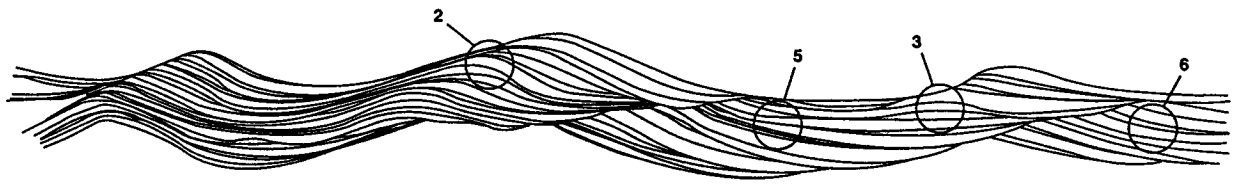

Ⓑ **Oscillatory dominant combined flow**

S13R3
Uo = 80 cm/s
Uu = 5 cm/s
T = 10.8 s

grain size = 0.23 mm
wavelength = 187 cm
aggradation rate = 1.5 mm/min
equilibrium bed forms: SLR and HM

1 meter

Fig. 3.7 Onshore-offshore shallow marine depositional profile contrasting sedimentation and flow parameters during fairweather and storm conditions. **A.** Fairweather conditions. Sediment transport is shoreward with short-period, low oscillatory velocity affecting the bottom from the shoreline to fairweather wave base. Both cross-shore and longshore near-bottom currents are weak. Suspended sediment concentrations are low and peak in area of breaking waves. From wave base to the swash zone stratification style ranges from: small-scale wave ripple stratification, large-scale high-angle cross-stratification, to planar lamination. **B.** Storm conditions. Sediment transport is basinward with long-period, high oscillatory velocity waves affecting the bottom from the shoreline to storm wave base. Unidirectional currents are significantly stronger, with geostrophically balanced flow assuming a shore-parallel direction for most of the flow depth but becoming shore-oblique (offshore direction) near the bottom. Suspended-sediment concentrations are high and peak under breaking waves but remain high toward the offshore. From wave base to the swash zone stratification style changes from: isotropic hummocky cross-stratification, anisotropic hummocky cross-stratification, swaley cross-stratification, large-scale high-angle cross-stratification, to planar lamination.

(A) Fairweather conditions

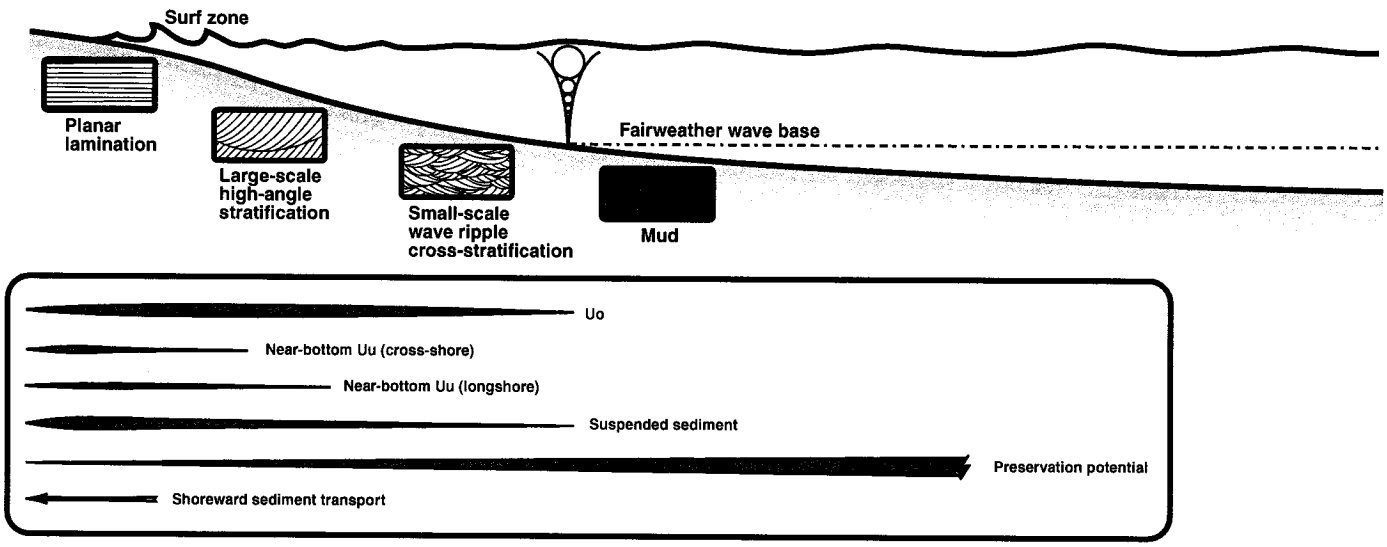

(B) Storm conditions

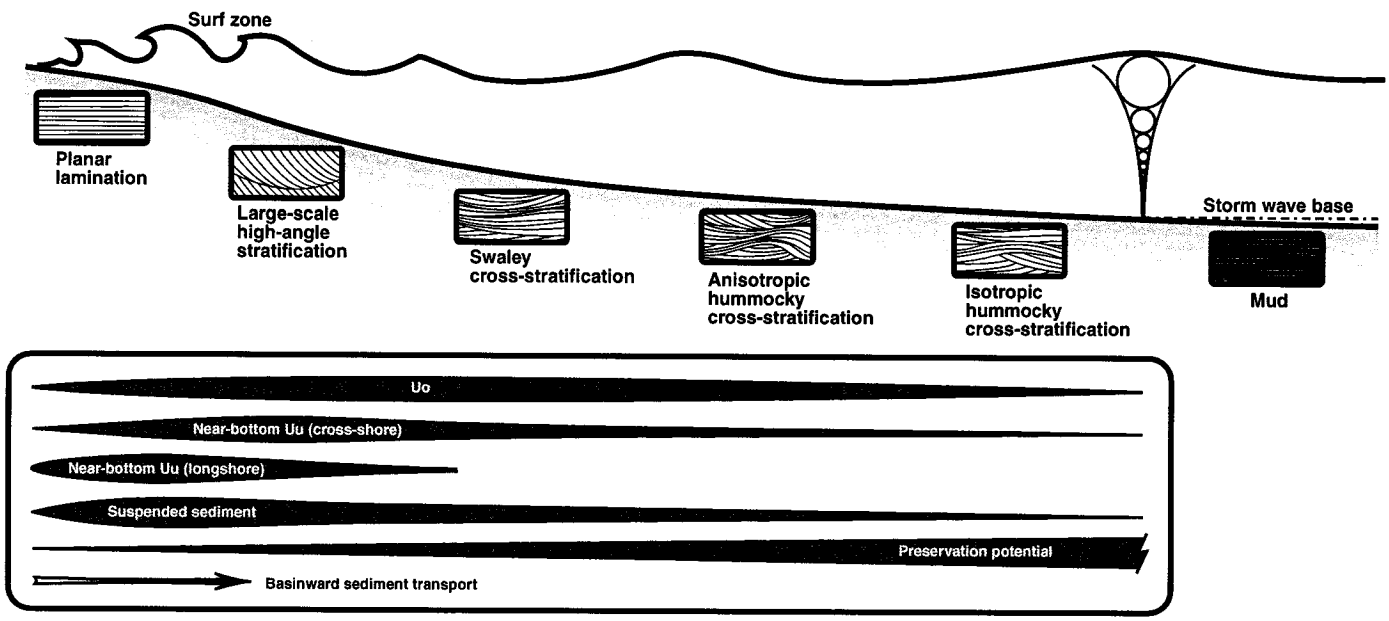

Table 3.1 Examples of storm sedimentation and flow parameters from modern continental shelves.

φ : Values displayed have different units
† : Oscillatory velocity
ς : Oscillation period
‡ : Unidirectional velocity
* : Compiled from various sources
ψ: From Vincent et al. 1982
¥ : In one storm event (from Beardley and Butman 1974)

Table 3.1 Examples of storm sedimentation and flow parameters from modern continental shelves

Author (date)	Aggradation rates	Suspended sediment concentration (g/l)	Sediment transport rate$^{\Psi}$	$U_0^{\dagger}$ (cm/s)	T^{ς} (s)	$U_u^{\ddagger}$ (cm/s)	Height above bed (m)	Depth (m)	Location	Storm type
Cacchione and Drake (1982)		0.075 (ave)		26.9 >45	8.9	28.9 13.6	1 0.2 2	18	Norton Sound (Alaska)	
Duke et al. (1991)				100		50	0.5 1		Inner shelf, North hemisphere	
Forristall et al. (1977)						>200	3	20	Texas Shelf	Tropical storm Delia
Grant and Madsen (1986)					12 6			112 28	-	
Héquette and Hill (1993)				>90	> 9	49	1.1	3.4	Beaufort Sea	
Hill et al. (2003)		1.25		150	6-7	50		10	Hudson Bay	
Lavelle et al. (1978)				39	10	80	1	10.5	New York	
Li et al. (1997)			9.5 g/ms						Scotian shelf	
Li and Amos (1999a)				55.6	14.2	10.9		39.1	Scotian shelf	
Li and Heffler (2002)			0.1-10 g/ms						Scotian shelf	
Madsen et al. (1993)		1 (lower 1m) ~3.75		60-100	9-14	≤ 45	1 0.27	13	Northern Atlantic	Halloween storm (1991)
Myrow and Fisher (2002)*		≤ ~ 1.4					1.2	13	Various locations	
Sherwood et al. (1994)				24 31 37 21 30 46	12.7 12.7 12.7 12.7 12.7 12.7	 58 	1 1 1 near-bottom near-bottom near-bottom	120 90 59 120 90 59	Californian shelf	
		≤ 0.056 ≤ 0.074 ≤ 0.093	4.54 g/m^{2}s 11.6 g/m^{2}s 9.7 g/m^{2}s	19 26 30		14 32 20		90 90 90		Swell event Southerly storm Northerly storm
Smith and Hopkins (1972)			1.83 g/ms	80 58			3 3 3	50 80	Shelf off Oregon and Washington	
Snedden et al. (1988)	< 10 cm discrete bed				11 9	~ 70 ~ 20		70 74	Texas shelf	1980 storm 1984 storm
Swift et al. (1983)	few cm to <20 cm$^{\Psi}$	0.04-0.05	2.65-265 g/ms			20-30 10	near-bottom near-bottom 1	10 (3km offshore)	Northern Atlantic	
Swift and Nummedal (1987)$^{\Psi}$						85 100 42 60		70 6.3 40 12	Texas shelf Mid-Altantic	hurricane hurricane mid-lat. storm mid-lat. storm
Washburn et al. (1993)			1.93·10^5 g/s (in 60 days)			50 7		10 150	Northern California	
Wright et al. (1994)		> 1		50-100	≤ 22	12	~ 1	13	Northern Atlantic	Halloween storm (1991)

CHAPTER 4

CONCLUSIONS

The thesis investigated long-period oscillatory and combined-flow equilibrium bed forms generated in the laboratory. The main contributions of the thesis are listed in relation to the objective to which they are associated:

Objective 1. Construct phase diagrams representing the equilibrium bed phase for the range of oscillatory and unidirectional velocities, oscillation periods, and grain sizes explored.

Three equilibrium bed phase diagrams were constructed. All three diagrams present equilibrium bed phases on a graph of oscillatory velocity versus unidirectional velocity. The first phase diagram presents bed form data for runs using the finer grain size (ϕ = 0.14 mm) and longer oscillation period (T = 10.5 s) (Fig. 2.3). The second phase diagram showed the data for the finer grain size and shorter oscillation period (T = 8.0 s) (Fig. 2.4). The third diagram displays data for the coarser grain size (ϕ = 0.22 mm) and longer oscillation period (Fig. 2.5). With increasing purely oscillatory flow, the bed phases were: small-scale ripples, large-scale ripples, and plane bed. When the unidirectional flow increased, bed forms became progressively more asymmetric, and the bed was eventually planed flat.

Objective 2. Describe in detail the morphological characteristics of the different bed forms and provide diagnostic criteria to facilitate the differentiation of unidirectional, oscillatory, and combined-flow bed forms.

Based on wavelength, the ripples generated form two distinct populations. Small-scale ripples have wavelength < 20 cm, whereas large-scale ripples have wavelength > 100 cm. There were no intermediate-sized ripples; the dynamical reason for this is not yet understood. Small and large-scale ripples could be further differentiated by how their wavelength scaled to the orbital diameter of the oscillating flow. Small-scale ripples were anorbital, as their spacing did not scale to flow. Large-scale ripples, on the other hand, were orbital and had orbital diameter/wavelength ratios of 1 to 2 (Fig. 2.10). Data also suggest that symmetry, as expressed by the symmetry index, can be used to differentiate symmetric ripples (symmetry index ≤ 2) from asymmetric ripples (symmetry index > 2). In addition, combined-flow ripples could be differentiated form oscillatory-flow ripples by their convex-up sigmoidal profile, round crest area, and more 3D planform geometry.

Objective 3. Study the effect of unidirectional current velocity and bed aggradation rate on 3D symmetric large-scale bed forms (hummocky bed forms) and associated stratification.

Three-dimensional bed forms with broad dome-like crests and gently dipping convex-up flanks were generated under conditions of moderate oscillatory flow (50-90 cm/s), low unidirectional flow (0-12 cm/s) and long oscillation period (8.0-10.5 s) (Fig. 3.4). These bed forms were termed hummocky bed forms, and interpreted to form

hummocky cross-stratification in the ancient sedimentary record. Hummocky bed forms were not observed to develop over the entire bed surface. Rather, the hummocky bed forms coexisted with other bed forms (mainly large-scale ripples), and for this reason, they were not considered a distinct bed phase. In addition, they were better developed under the longer oscillation period and in the finer sediment, and would presumably cease to develop if the oscillation period was futher shortened and grain size further increased

The effects of increases of unidirectional current velocity and bed aggradation rate on stratification were studied by "synthetically" migrating and aggrading a hummocky bed profile. The superimposition of a small unidirectional flow (5-10 cm/s) on a moderate, purely oscillatory flow caused bed forms to preferentially migrate with the current and generated anisotropic cross-stratification showing a preferred direction of dip. More elevated unidirectional flow components formed high-angle cross-stratification resembling that formed by unidirectional dunes. It was also found that an increase in aggradation rate favored the preservation of hummocks and formed stratification not unlike hummocky cross-stratification. In contrast, a decrease in aggradation rate caused a decrease in hummock preservation and generated stratification resembling swaley cross-stratification. Finally, a depositional model for storm conditions on continental shelves was proposed. Hummocky cross-stratification was suggested to form above (but near) storm wave base under oscillatory-dominant combined-flows and moderate aggradation rates. Swaley cross-stratification is also interpreted to form under oscillatory-dominant combined-flows, but at shallower depth and under lower sediment deposition/transport ratios resulting in lower aggradation rates and the preferential erosion of convex-upward hummocks.

Our experimental results therefore provide interpretative tools to geologists who whish to infer paleohydraulic conditions from observed oscillatory and combined-flow

bed forms and associated stratification in order to interpret shallow marine sedimentary deposits. Furthermore, our results indicate that hummocky cross-stratification and swaley cross-stratification are most likely genetically related and that these sedimentary structures may serve as useful indicators of deposition under high-energy, long-period waves in unrestricted basins.

REFERENCES

Allen, J.R.L., 1979, A model for the interpretation of wave ripple-marks using their wavelength, textural composition, and shape: J. Geol. Soc. London, v. 136, p. 673-682.

Allen, J.R.L., 1984, Sedimentary structures, their character and physical basis: Developments in sedimentology, v. 30: Amsterdam, Elsevier, 663 p.

Allen, J.R.L., 1985, Principles of physical sedimentology: London, George Allen and Unwin, 272 p.

Allen, J.R.L., 1993, Sedimentary structures: Sorby and the last decade: J. Geol. Soc., v. 150, p. 471-425.

Allen, P.A., 1985, Hummocky cross-stratification is not produced purely under progressive gravity waves: Nature, v. 313, p. 562-564.

Allen, P.A., and Underhill, J.R., 1989, Swaley cross-stratification produced by unidirectional flows, Bencliff Grit (Upper Jurassic), Dorset, UK: J. Geol. Soc. London, v. 146, p. 241-252.

Arnott, R.W.C., 1992, Ripple cross-stratification in swaley cross-stratified sandstones of the Chungo Member, Mount Yamnuska, Alberta: Can. J. Earth Sci., v. 29, p. 1802-1805.

Arnott, R.W.C., and Southard, J.B., 1990, Exploratory flow-duct experiments on combined-flow bed configurations, and some implications for interpreting storm-event stratification: J. Sed. Petrol., v. 60, p. 211-219.

Ashley, G.M., 1990, Classification of large-scale subaqueous bedforms: a new look at an old problem: J. Sed. Petrol., v. 60, p. 160-172.

Bagnold, R.A., 1946, Motion of waves in shallow water interaction between waves and sand bottoms: Proc. Royal Soc. London, A, v. 187, p. 1-15.

Bagnold, R.A., 1963, Mechanics of marine sedimentation, *in* Hill, M.N., ed., The Sea; Ideas and observations on progress in the study of the seas - Vol. 3: New York, John Wiley and Sons, p. 507-528.

Banerjee, I., 1996, Populations, trends, and cycles in combined-flow bedforms: J. Sed. Res., v. 66, p. 868-874.

Beardley, R.C., and Butman, B., 1974, Circulation on the New England continental shelf: response to strong winter storms: Geo. Res. Let., v. 1, p. 181-184.

Brebner, A., and Riedel, P.H., 1973, A new oscillating water tunnel: J. Hydraul. Res., v. 11, p. 107-121.

Bridge, J.S., and Best, J.L., 1988, Flow, sediment transport and bedform dynamics over the transition from dunes to upper-stage plane beds: implications for the formation of planar laminae: Sedimentology, v. 35, p. 753-763.

Bridge, J.S., 2003, Rivers and floodplains - forms, processes, and sedimentary record: Oxford, UK, Blackwell Publishing, 491 p.

Bucher W.H., 1919, On ripples and related sedimentary surface forms and their paleogeopraphic interpretation - Part I. The origin of ripples and related sedimentary surface forms.: Am. J. Sci., v. 47., p. 241-269.

Cacchione, D.A., and Drake, D.E., 1982, Measurements of storm-generated bottom stresses on the continental shelf: J. Geophys. Res., v. 87, p. 1952-1960.

Campbell, C.V., 1966, Truncated wave-ripple laminae: J. Sed. Petrol., v. 36, p. 825-828.

Carstens, M.R., Neilson, F.M., and Altinbilek, H.D., 1969, Bed forms generated in the laboratory under an oscillatory flow: analytical and experimental study: , U.S. army corps of engineers, coastal engineering research center, 39 p.

Cheel, R.J., and Leckie, D.A., 1993, Hummocky cross-stratification, Sedimentology review: Oxford, Blackwell Scientific Publications, p. 103-122.

Clifton, H.E., 1976, Wave-formed sedimentary structures - a conceptual model, *in* Davis, R., and Ethington, R., eds., SEPM special publication: Tulsa, Oklahoma, p. 126-148.

Clifton, H.E., and Dingler, J.R., 1984, Wave-formed structures and paleoenvironmental reconstruction: Marine Geol., v. 60, p. 165-198.

Clifton, H.E., Hunter, R.E., and Phillips, R.L., 1971, Depositional structures and processes in the non-barred high-energy nearshore: J. Sed. Petrol., v. 41, p. 651-670.

Davidson-Arnott, R.G.D., and Greenwood, B., 1976, Facies relationships on a barred coast, Kouchibouguac Bay, New Brunswick, Canada, *in* Davis, R.A.J., and Ethington, R.L., eds., Beach and neashore sedimentation: Special publication No.24: Tulsa, Oklahoma, SEPM, p. 149-168.

Davies, A.G., Soulsby, R.L., and King, H.L., 1988, A numerical model of the combined wave and current bottom boundary layer: J. Geophys. Res., v. 93, p. 491-508.

De Raaf, J.F.M., Boersma, J.R., and Van Gelder, A., 1977, Wave-generated structures and sequences from a shallow marine succession, Lower Carboniferous, County Cork, Ireland: Sedimentology, v. 24, p. 451-483.

DeCelles, P.G., and Cavazza, W., 1992, Constraints on the formation of Pliocene hummocky cross-stratification in Calabria (Southern Italy) from consideration of hydraulic and dispersive equivalence, grain-flow theory, and suspended-load fallout rate: J. Sed. Petrol., v. 62, p. 555-568.

Dingler, J.R., 1979, The treshold of grain motion under oscillatory flow in a laboratory wave channel: J. Sed. Petrol., v. 49, p. 287-294.

Dott, R.H.Jr., and Bourgeois, J., 1982, Hummocky stratification: significance of its variable bedding sequences: Geol. Soc. Am. Bull., v. 93, p. 663-680.

Duke, W.L., 1985, Hummocky cross-stratification, tropical hurricanes, and intense winter storms: Sedimentology, v. 32, p. 167-194.

Duke, W.L., 1987, Hummocky cross-stratification, tropical hurricanes, and intense winter storms - Reply: Sedimentology, v. 34, p. 344-359.

Duke, W.L., 1990, Geostrophic circulation or shallow marine turbidity currents ? The dilemma of paleoflow patterns in storm-influenced prograding shoreline systems: J. Sed. Petrol., v. 60, p. 870-883.

Duke, W.L., Arnott, R.W.C., and Cheel, R.J., 1991, Shelf sandstones and hummocky cross-stratification: new insight on a stormy debate: Geology, v. 19, p. 625-628.

Dumas, S., Arnott, R.W.C., and Southard, J.B., in review, Experimental investigation of equilibrium oscillatory- and combined-flow bed forms: J. Sed. Res.

Eyles, N., and Clark, B.M., 1986, Significance of hummocky and swaley cross stratification in late Pleistocene lacustrine sediments of the Ontario basin, Canada: Geology, v. 14, p. 679-682.

Forristall, G.Z., Hamilton, R.C., and Cardonne, V.J., 1977, Continental shelf currents in tropical storm Delia: observations and theory: J. Phys. Ocean., v. 7, p. 532-546.

Fredsoe, J., 1984, Turbulent boundary layer in wave-current motion: J. Hydraul. Eng., v. 110, p. 1103-1120.

Gallagher, E.L., 2003, A note on megaripple in the surf zone: evidence for their relation to steady flow dunes: Marine Geol., v. 192, p. 171-176.

Gibling, M.R., and Rust, B.R., 1993, Alluvial ridge-and-swale topography: a case study from the Morien Group of Atlantic Canada: Spec. Publs. Int. Ass. Sediment., v. 17, p. 133-150.

Grant, W.D., and Madsen, O.S., 1979, Combined wave and current interaction with rough bottom: J. Geophys. Res., v. 84, p. 1797-1808.

Grant, W.D., and Madsen, O.S., 1986, the continental-shelf bottom boundary layer: Ann. Rev. Fluid Mech., v. 18, p. 265-305.

Greenwood, B., and Sherman, D.J., 1986, Hummocky cross-stratification in the surf zone: flow parameters and bedding genesis: Sedimentology, v. 33, p. 33-45.

Harms, J.C., 1969, Hydraulic significance of some sand ripples: Geol. Soc. Am. Bull., v. 80, p. 363-396.

Harms, J.C., Southard, J.B., Spearing, D.R., and Walker, R.G., 1975, Depositional environments as interpreted from primary sedimentary structures and stratification sequences, *in* SEPM, ed.: Binghampton, 161 p.

Harms, J.C., Southard, J.B., and Walker, R.G., 1982, Structures and sequences in clastic rocks: Tulsa, Oklahoma, SEPM, 249 p.

Hart, B.S., Vantfoort, R.M., and Plint, G.A., 1990, Is there evidence for geostrophic currents preserved in the sedimentary record of the inner to middle shelf deposits ? - Discussion: J. Sed. Petrol., v. 60, p. 633-635.

Hayes, M.O., 1967, Hurricanes as geological agents, South Texas coast: AAPG Bull., v. 51, p. 937-956.

Héquette, A., and Hill, P.R., 1993, Storm-generated currents and offshore sediment transport on a sandy surface, Tibjak Beach, Canadian Beaufort Sea: Marine Geol., v. 113, p. 283-304.

Higgs, R., 1990, Is there evidence for geostrophic currents preserved in the sedimentary record of the inner to middle shelf deposits ? -Discussion: J. Sed. Petrol., v. 60, p. 630-632.

Hill, P.R., Meulé, S., and Longuépée, H., 2003, Combined-flow processes and sedimentary structures on the shoreface of the wave-dominated Grande-Rivière-de-la-Baleine: J. Sed. Res., v. 73., p. 217-226

Inman, D.L., and Bowen, A.J., 1963, Flume experiments on sand transport by waves and currents: 8th conference on coastal engineering, p. 137-150.

Jackson, J.A., 1997, Glossary of geology: Alexandria, Virginia, American Geological Institute, 769 p.

Kennedy, J.F., and Falcon, M.F., 1965, Wave-generated sediment ripples: Cambridge, MIT, department of civil engineering, hydrodynamics laboratory, 55 p.

Khelifa, A., and Ouellet, Y., 2000, Prediction of sand ripple geometry under waves and currents: Journal of waterways, port, coastal, and ocean engineering, v. 126, p. 14-22.

Klein, G.deV., and Marsaglia, K.M., 1987, Hummocky cross-stratification, tropical hurricanes, and intense winter storms - Discussion: Sedimentology, v. 34, p. 333-338.

Komar, P.D., 1974, Oscillatory ripple marks and the evaluation of ancient wave conditions and environments: J. Sed. Petrol., v. 44, p. 169-180.

Komar, P.D., and Miller, M.C., 1973, The threshold of sediment movement under oscillatory water waves: J. Sed. Petrol., v. 43, p. 1101-1110.

Komar, P.D., and Miller, M.C., 1975, Sediment threshold under oscillatory waves: 14th conference on coastal engineering, p. 772.

Lavelle, J.W., Young, R.A., Swift, D.J.P., and Clarke, T.L., 1978, Near-bottom sediment concentration and fluid velocity measurements on the inner continental shelf, New York: J. Geophys. Res., v. 83, p. 6052-6062.

Leckie, D.A., 1988, Wave-formed, coarse-grained ripples and their relationship to hummocky cross-stratification: J. Sed. Petrol., v. 58, p. 607-622.

Leckie, D.A., and Krystinik, L.F., 1989, Is there evidence for geostrophic current preserved in the sedimentary record of inner to middle-shelf deposits ?: J. Sed. Petrol., v. 59, p. 862-870.

Leckie, D.A., and Walker, R.G., 1982, Storm- and tide-dominated shorelines in Cretaceous Moosebar-Lower Gates interval - outcrop equivalents of deep basin gas trap in Western Canada: AAPG Bull., v. 66, p. 138-157.

Lee Young, J.S., and Sleath, J.F.A., 1990, Ripple formation in combined transdirectional steady and oscillatory flow: Sedimentology, v. 37, p. 509-516.

Li, M.Z., and Amos, C.L., 1998, Predicting ripple geometry and bed roughness under combined waves and currents in a continental shelf environment: Continental Shelf Res., v. 18, p. 941-970.

Li, M.Z., and Amos, C.L., 1999a, Field observations of bedforms and sediment transport thresholds of fine sand under combined waves and currents: Marine Geol., v. 158, p. 147-160.

Li, M.Z., and Amos, C.L., 1999b, Sheet flow and large wave ripples under combined wave and currents: field observations, model predictions and effects on boundary layer dynamics: Continental Shelf Res., v. 19, p. 637-663.

Li, M.Z., Amos, C.L., and Heffler, D.E., 1997, Boundary layer dynamics and sediment transport under storm and non-storm conditions on the Scotian Shelf: Marine Geol., v. 141, p. 157-181.

Li, M.Z., and Heffler, D.E., 2002, Continental shelf sediment transport studies in Canada: theories and recent technology advances: Geoscience Canada, v. 29, p. 35-48.

Li, M.Z., and Heffler, D.E., 2002, Continental shelf sediment transport studies in Canada: principal scientific advances and future directions: Geoscience Canada, v. 29, p. 53-68.

Li, Z., and Davies, A.G., 1996, Towards predicting sediment transport in combined wave-current flow: Journal of waterways, port, coastal, and ocean engineering, v. 122, p. 157-164.

Lofquist, K.E.B., 1978, Sand ripple growth in a oscillatory-flow water tunnel: Fort Belvoir, VA, U.S. army corps of engineering research center, 101 p.

Madsen, O.S., Wright, L.D., Boon, J.D., and Chisholm, T.A., 1993, Wind stress, bed roughness and sediment suspension on the inner shelf during an extreme storm event: Continental Shelf Res., v. 13, p. 1303-1324.

Manighetti, B., and Carter, L., 1999, Across-shelf sediment dispersal, Hauraki Gulf, New Zealand: Marine Geol., v. 160, p. 271-300.

McKee, E.D., 1965, Experiments on ripple lamination, *in* Middleton, G., ed., Primary sedimentary structures and their hydrodynamic interpretation: Special publication No.12: Tulsa, Oklahoma, SEPM, p. 66-83.

Middleton, G.V., and Southard, J.B., 1978, Mechanics of sediment movement: Binghampton, SEPM, 161 p.

Midtgaard, H.H., 1996, Inner-shelf to lower-shoreface hummocky sandstone bodies with evidence for geostrophic influenced combined flow, Lower Cretaceous, West Greenland: J. Sed. Res., v. 66, p. 343-353.

Miller, M.C., and Komar, P.D., 1980a, A field investigation of the relationship between oscillation ripple spacing and the near-bottom water orbital motions: J. Sed. Petrol., v. 50, p. 183-191.

Miller, M.C., and Komar, P.D., 1980b, Oscillation sand ripples generated by laboratory apparatus: J. Sed. Petrol., v. 50, p. 173-183.

Molgat, M., and Arnott, R.W.C., 2001, Combined tide and wave influence on sedimentation patterns in the Upper Jurassic Swift Formation, sout-estern Alberta: Sedimentology, v. 488, p. 1353-1369.

Morton, R.A., 1981, Formation of storm deposits by wind-forced currents in the Gulf of Mexico and the North Sea, *in* Nio, S.D., Shuttenhelm, R.T.E., and Van Weering, T.C.E., eds., Holocene marine sedimentation in the North Sea: Special publication No.5: Oxford, Blackwell Scientific Publications, p. 385-396.

Morton, R.A., 1988, Nearshore responses to great storms: Geol. Soc. Am. Special Paper, v. 229, p. 7-22.

Murray, P.B., Davies, A.G., and Soulsby, R.L., 1991, Sediment pick-up in wave and current flows, *in* Soulsby, R., and Betess, R., eds., Sand transport in rivers, estuaries, and the sea: Rotterdam, A.A. Balkema, p. 37-49.

Myrow, P.M., Fischer, W., and Goodge, J., 2002, Wave-modified turbidites; combined-flow shoreline and shelf deposits, Cambrian, Antartica: J.Sed.Res., v. 72, p. 641-656.

Myrow, P.M., and Southard, J.B., 1990, Combined-flow model for vertical stratification sequences in shallow marine strom-deposited beds: J. Sed. Petrol., v. 61, p. 202-210.

Myrow, P.M., and Southard, J.B., 1996, Tempestite deposition: J. Sed. Res., v. 66, p. 875-887.

Nottvedt, A., and Kreisa, R.D., 1987, Model for the combined-flow origin of hummocky cross-stratification: Geology, v. 15, p. 357-361.

Paphitis, D., Velegrakis, A.F., Collins, M.B., and Muirhead, A., 2001, Laboratory investigations into the threshold of movement of natural sand-sized sediments under unidirectional, oscillatory and combined flows: Sedimentology, v. 48, p. 645-659.

Plint, A.G., and Walker, R.G., 1987, Cardium Formation 8. Facies and environments of the Cardium shoreline and coastal plain in the Kakwa field and adjacent areas, Northwestern Alberta: Bull. Can. Petrol. Geol., v. 35, p. 48-64.

Sherwood, C.R., Butman, B., Cacchione, D.A., Drake, D.E., Gross, T.F., Sternberg, R.W., Wiberg, P.L., and Williams, A.J.III., 1994, Sediment-transport events on the northern California continental shelf during 1990-1991 STRESS experiment: Continental Shelf Res., v. 14, p. 1063-1099.

Sleath, J.F.A., 1976, On rolling-grain ripples: J. Hydraul. Res., v. 14, p. 69-81.

Smith, J.D., 1977, Modeling of sediment transport on continental shelves, *in* Goldberg, E., McCave, I., O'Brien, J., and Steele, J., eds., The sea - ideas and observations in progress in the study of the seas: New York, John Wiley & Sons; Wiley-Interscience, p. 539-577.

Smith, J.D., and Hopkins, T.S., 1972, Sediment transport on the continental shelf off Washington an Oregon in light of the recent current measurements, *in* Swift, D.J.P., Duane, D.B., and Pilkey, O.H., eds., Shelf sediment transport; process and pattern: Stroudsburg, Pennsylvania, Dowden, Hutchinson and Ross, p. 143-180.

Southard, J.B., and Boguchwal, L.A., 1990, Bed configurations in steady unidirectional water flows. Part 2. Synthesis of flume data: J. Sed. Petrol., v. 60, p. 658-679.

Southard, J.B., Lambie, J.M., Federico, D.C., Pile, H.T., and Weidman, C.R., 1990, Experiments on bed configurations in fine sands under bidirectional purely oscillatory flow, and the origin of hummocky cross-stratification: J. Sed. Petrol., v. 60, p. 1-17.

Snedden, J.W., Nummedal, D., and Amos, A.F., 1988, Storm- and fair-weather combined flow on the central texas continental shelf: J. Sed. Petrol., v. 58, p. 580-595.

Swift, D.J.P., and Figueiredo, A.G.Jr., 1983, Hummocky cross-stratification and megaripples: a geological double standard ?: J. Sed. Petrol., v. 53, p. 1995-1317.

Swift, D.J.P., Han, G., and Vincent, C.E., 1986, Fluid processes and sea-floor response on a modern storm-dominated shelf: middle Atlantic Shelf of North America. Part 1. The storm-current regime, *in* Knight, J.R., and McLean, J.R., eds., Shelf sands and sandstones: CSPG Memoir 11: Calgary, Alberta, CSPG, p. 99-119.

Swift, D.J.P., and Nummedal, D., 1987, Hummocky cross-stratification, tropical hurricanes, and intense winter storms - Discussion: Sedimentology, v. 34, p. 338-344.

Tanaka, H., 1986, Turbulence structure and bed friction under waves and current interacted motion: 3rd international symposium on river sedimentation, p. 334-343.

Tanaka, H., Yoshitake, T., and Shuto, N., 1991, Bedload transport of non-uniform sand due to waves and current, *in* Soulsby, R., and Betess, R., eds., Sand transport in rivers, estuaries, and the sea: Rotterdam, A.A. Balkema, p. 45-49.

Tillman, R.W., 1986, Swaley cross-stratification and associated features, Upper Cretaceous Western Interior Seaway of United States - (abstract): AAPG Bull., v. 5, p. 656.

Trowbridge, J.H., and Nowell, A.R.M., 1994, An introduction to the sediment transport events on shelves and slopes (STRESS) program: Continental Shelf Res., v. 14, p. 1057-1061.

Van Rijn, L.C., and Havinga, F.J., 1995, Transport of fine sands by currents and waves. II: Journal of Waterways, Port, Coastal, and Ocean Engineering, v. 121, p. 123-133.

Van Rijn, L.C., Nieuwjaar, M.W.C., van der Kaay, T., Nap, E., and van Kampen, A., 1993, Transport of fine sands by currents and waves: Journal of Waterways, Port, Coastal, and Ocean Engineering, v. 119, p. 123-143.

Vincent, C.E., 1986, Processes affecting sand transport on storm-dominated shelf, *in* Knight, J.R., and McLean, J.R., eds., Shelf sands and sandstones: CSPG Memoir 11: Calgary, Alberta, CSPG, p. 121-132.

Vincent, C.E., Young, R.A., and Swift, D.J.P., 1982, On the relationship between bedload and suspended sand transport on the inner shelf, Long Island, New York: J. Geoph. Res., v. 87, p. 4163-4170.

Walker, R.G., 1979, Facies Model 7: Shallow marine sands, *in* Walker, R.G., ed., Facies Model: Geoscience Canada Reprint Series 1: , p. 75-80.

Walker, R.G., 1982, Hummocky and swaley cross-stratification: 11th International congress on sedimentology, p. 22-30.

Walker, R.G., 1984, Facies model: St-John's, Geological Association of Canada, 317 p.

Walker, R.G., Duke, W.L., and Leckie, D.A., 1983, Hummocky stratification: significance of its variable bedding sequences: discussion and reply: Geol. Soc. Am. Bull., v. 94, p. 1245-1251.

Walker, R.G., and Plint, A.G., 1992, Chapter 12. Wave- and storm-dominated shallow marine systems, *in* Walker, R.G., and James, N.P., eds., Facies Model - response to sea level change: St-John's, Geological Association of Canada, p. 219-238.

Washburn, L., Swenson, M.S., Largier, J.L., Kosro, P.M., and Ramp, S.R., 1993, Cross-shelf sediment transport by anticyclonic eddy off Northern California: Science, v. 261, p. 1560-1564.

Wiberg, P., 1995, A theoretical investigation of boundary layer flow and bottom shear stress for smooth, transitional, and rough flow under waves: J. Geophys. Res., v. 100, p. 22667-22679.

Wright, L.D., 1987, Shelf-surfzone coupling: diabathic shorefce transport: Coastal sediment '87, p. 25-80.

Wright, L.D., Xu, J.P., and Madsen, O.S., 1994, Across-shelf benthic transports on the inner shelf of the middle Atlantic Bight during the "Halloween storm" of 1991: Marine Geol., v. 118, p. 61-77.

Yokokawa, M., 1995, Combined-flow ripples: genetic experiments and applications for geologic records: Fukuoka, Japan, Faculty of science, Earth and planetary sciences, Kyushu University, Japan, 38 p.

Yang, B.C., Chun, S.S., and Dalrymple, R.W., 2002, Intertidal sedimentation on a wave-dominated, open coast tidal flat, SW Korea: Summer tidal flat and winter shoreface: Advances in Earth Sciences Research Conference 2002: Sedimentology and Stratigraphy, p.56-58

APPENDICES

Appendix A – Sand characteristics and grain size data

(A) Very fine sand used in experimental Series 1 to 12

Provenance: Sand and gravel pit in New York State (Ottawa Sand ?)

Color: pinkish buff

Average roundness: sub-angular

Mineralogy: No petrographic analysis was done but based on a hand-held sample it was estimated that the light-colored portion of this sand is quartz-dominated while dark grains most likely consists of heavy minerals and micas. In addition, there were plenty of organic particles that had accumulated during outdoor storage. This sand was also, at one time, host to a family of squirrels that also contributed to its heterogeneous nature. This heterogeneity was greatly appreciated when attempting to visualize stratification.

Size: very fine sand; mean grain size of 0.11mm (see following grain size analysis)

Sorting: moderately sorted (std dev = 0.725ϕ)

(B) Fine sand used in experimental Series 13 to 18

Provenance: Sand and gravel pit in Slatersville, Rhode Island (generously donated by the Holliston Sand Company)

Color: whitish buff

Average roundness: sub-angular

Mineralogy: No petrographic analysis was done. Sand appeared quartz-rich with more abundant micas than the finer sand described above.

Size: fine sand; mean grain size of 0.17mm (see following grain size analysis)

Sorting: very well sorted (std dev = 0.342ϕ)

GRAIN SIZE ANALYSIS- 0.11 mm (very fine sand)

Finer sand: sand used in experimental Series 1-12

SAND	arith. mean	std. dev.
very fine	0.104 mm	0.076

"X" axis (mm)	cumul. %	weigth %	m - midpoint	f - weight %	fm	m-x bar	(m-x bar)2	f(m-x bar)2
2-1.4	0.000	0.000	1.700					
1.4-1	0.005	0.005	1.200	0.005	0.006	1.096	1.201	0.006
1-.71	0.186	0.181	0.855	0.181	0.155	0.751	0.564	0.102
.71-.50	1.005	0.819	0.605	0.819	0.495	0.501	0.251	0.205
.50-.35	1.344	0.339	0.425	0.339	0.144	0.321	0.103	0.035
.35-.25	2.761	1.417	0.300	1.417	0.425	0.196	0.038	0.054
.25-.18	7.310	4.549	0.215	4.549	0.978	0.111	0.012	0.056
.18-.12	19.703	12.393	0.150	12.393	1.859	0.046	0.002	0.026
.12-.088	49.415	29.712	0.104	29.712	3.090	0.000	0.000	0.000
.088-.063	76.836	27.421	0.076	27.421	2.070	-0.029	0.001	0.023
.063-.044	97.322	20.486	0.054	20.486	1.096	-0.051	0.003	0.053
.044-.031	99.999	2.677	0.038	2.677	0.100	-0.067	0.004	0.012
.031-.016	100.000	0.000	0.024					
.016-.008	100.000	0.000	0.012					
.008-.004	100.000	0.000	0.006					
.004-.002	100.000	0.000	0.003					
.002-.001	100.000	0.000	0.002					
< .001	100.000	0.000						
					mean =			std dev. =
					0.104			0.076

weight % - 0.11mm (very fine sand)

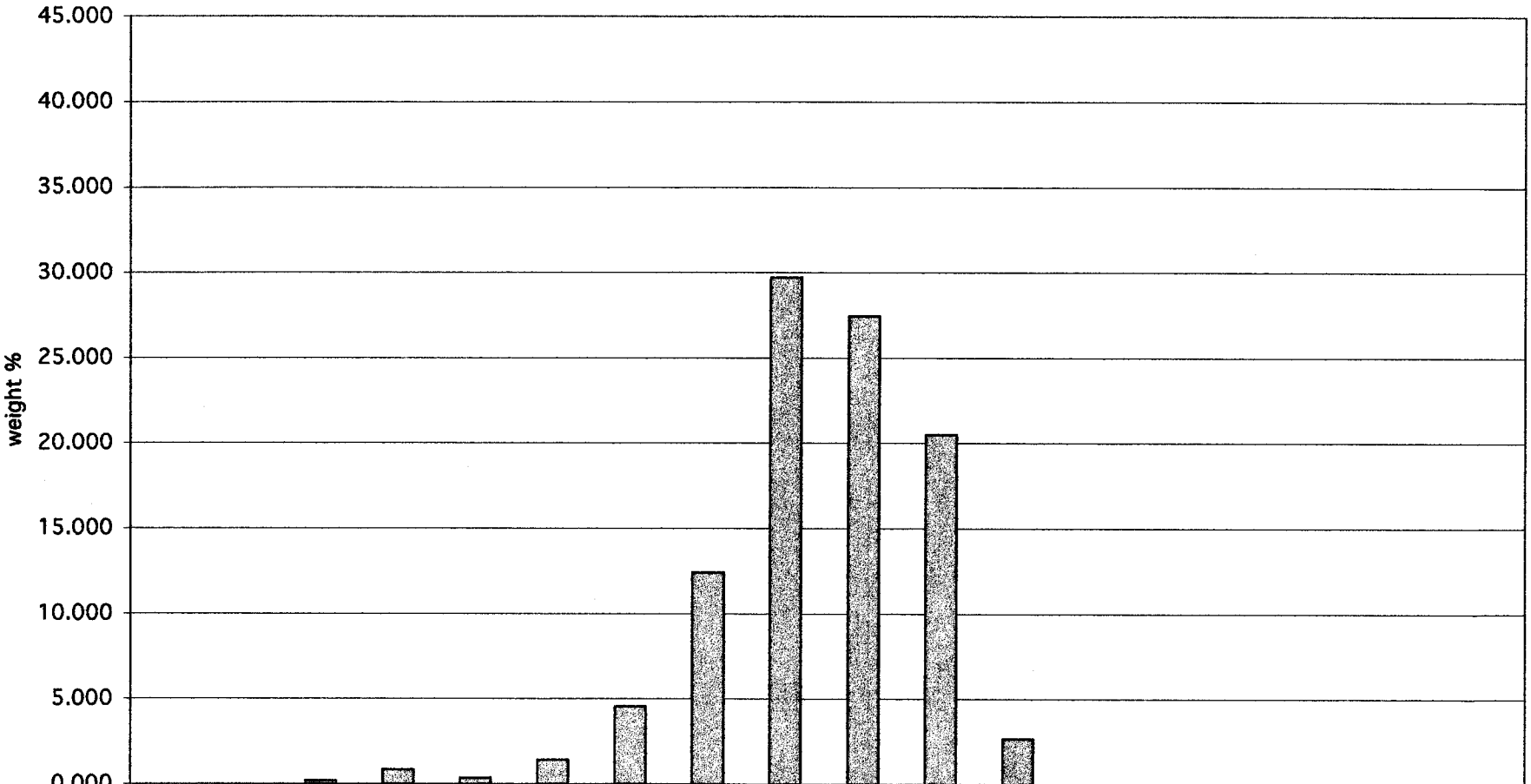

	2-1.4	1.4-1	1-.71	.71-.50	.50-.35	.35-.25	.25-.18	.18-.12	.12-.088	.088-.063	.063-.044	.044-.031	.031-.016	.016-.008	.008-.004	.004-.002	.002-.001	< .001
Series1	0.000	0.005	0.181	0.819	0.339	1.417	4.549	12.39	29.71	27.42	20.48	2.677	0.000	0.000	0.000	0.000	0.000	0.000

size (mm)

cumulative weight % - 0.11 mm (very fine sand)

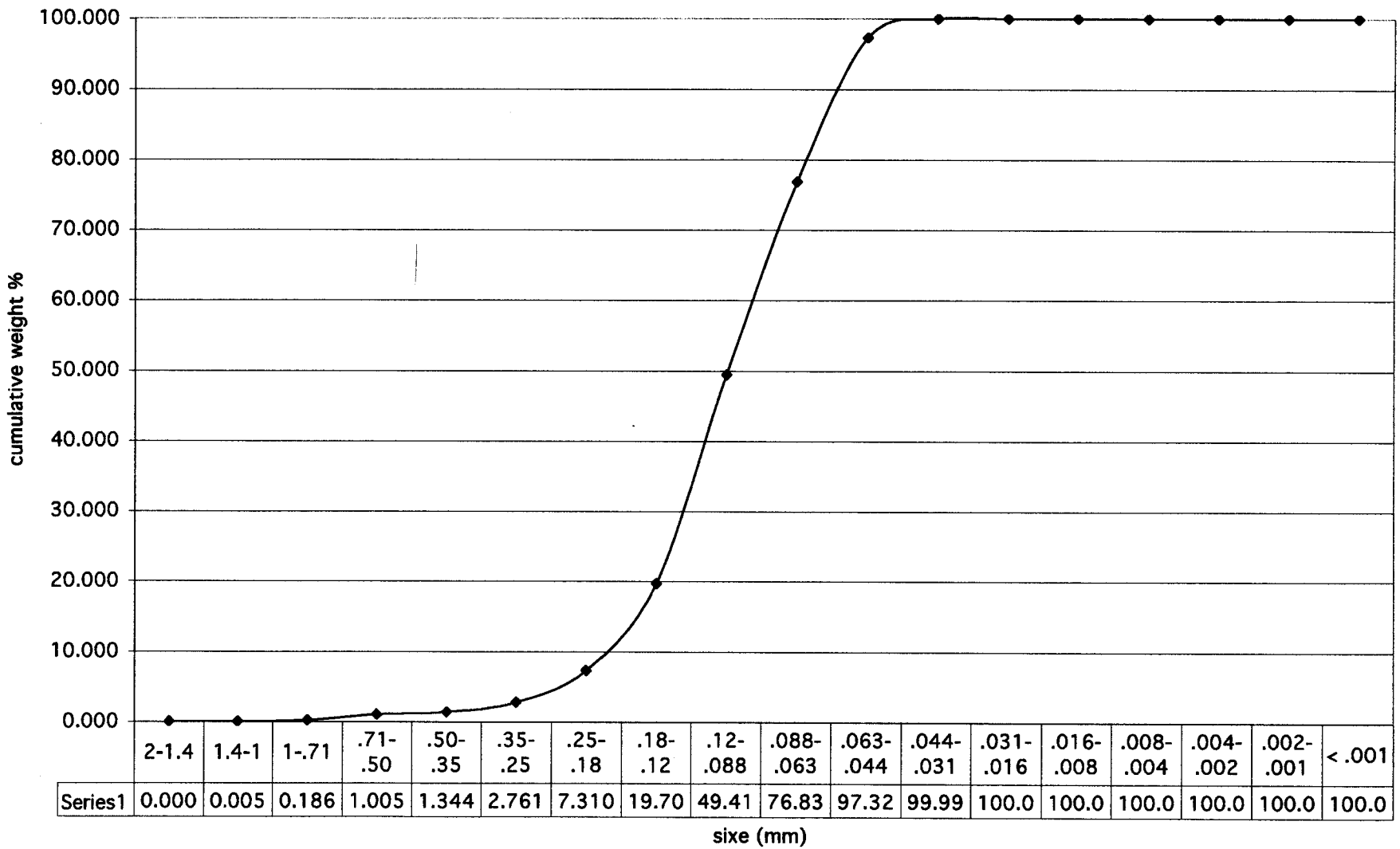

	2-1.4	1.4-1	1-.71	.71-.50	.50-.35	.35-.25	.25-.18	.18-.12	.12-.088	.088-.063	.063-.044	.044-.031	.031-.016	.016-.008	.008-.004	.004-.002	.002-.001	< .001
Series1	0.000	0.005	0.186	1.005	1.344	2.761	7.310	19.70	49.41	76.83	97.32	99.99	100.0	100.0	100.0	100.0	100.0	100.0

sixe (mm)

GRAIN SIZE ANALYSIS - 0.17 mm sand (fine sand)

Coarser sand: sand used in experimental Series 13-18

SAND	arith. mean	std. dev.
fine	0.172	0.059

"X" axis (mm)	cumul. %	weigth %	m - midpoint	f - weight %	fm	m-x bar	(m-x bar)2	f(m-x bar)2
2-1.4	0.001	0.001	1.700	0.001	0.002	1.528	2.336	0.002
1.4-1	0.005	0.004	1.200	0.004	0.005	1.028	1.058	0.004
1-.71	0.008	0.003	0.855	0.003	0.003	0.683	0.467	0.001
.71-.50	0.078	0.070	0.605	0.070	0.042	0.433	0.188	0.013
.50-.35	0.855	0.777	0.425	0.777	0.330	0.253	0.064	0.050
.35-.25	6.017	5.162	0.300	5.162	1.549	0.128	0.016	0.085
.25-.18	39.077	33.060	0.215	33.060	7.108	0.043	0.002	0.062
.18-.12	80.125	41.048	0.150	41.048	6.157	-0.022	0.000	0.019
.12-.088	96.957	16.832	0.104	16.832	1.751	-0.068	0.005	0.077
.088-.063	99.461	2.504	0.076	2.504	0.189	-0.096	0.009	0.023
.063-.044	99.914	0.453	0.054	0.453	0.024	-0.118	0.014	0.006
.044-.031	99.952	0.038	0.038	0.038	0.001	-0.134	0.018	0.001
.031-.016	100.000	0.048	0.024	0.048	0.001	-0.148	0.022	0.001
.016-.008	100.000	0.000	0.012					
.008-.004	100.000	0.000	0.006					
.004-.002	100.000	0.000	0.003					
.002-.001	100.000	0.000	0.002					
< .001	100.000	0.000						

mean = 0.172

std dev. = 0.059

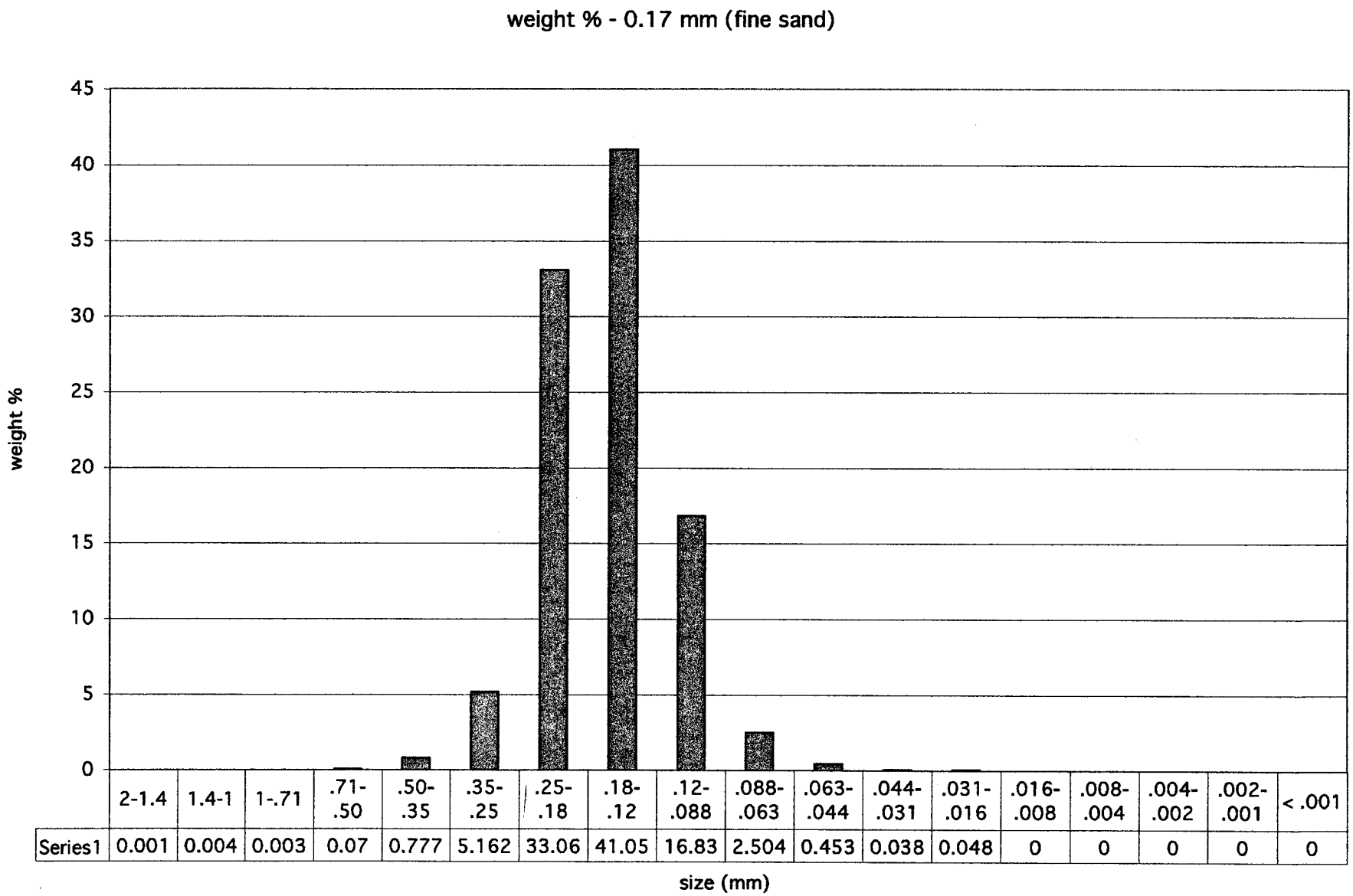

	2-1.4	1.4-1	1-.71	.71-.50	.50-.35	.35-.25	.25-.18	.18-.12	.12-.088	.088-.063	.063-.044	.044-.031	.031-.016	.016-.008	.008-.004	.004-.002	.002-.001	< .001
Series1	0.001	0.004	0.003	0.07	0.777	5.162	33.06	41.05	16.83	2.504	0.453	0.038	0.048	0	0	0	0	0

cumulative weight % - 0.17 mm (fine sand)

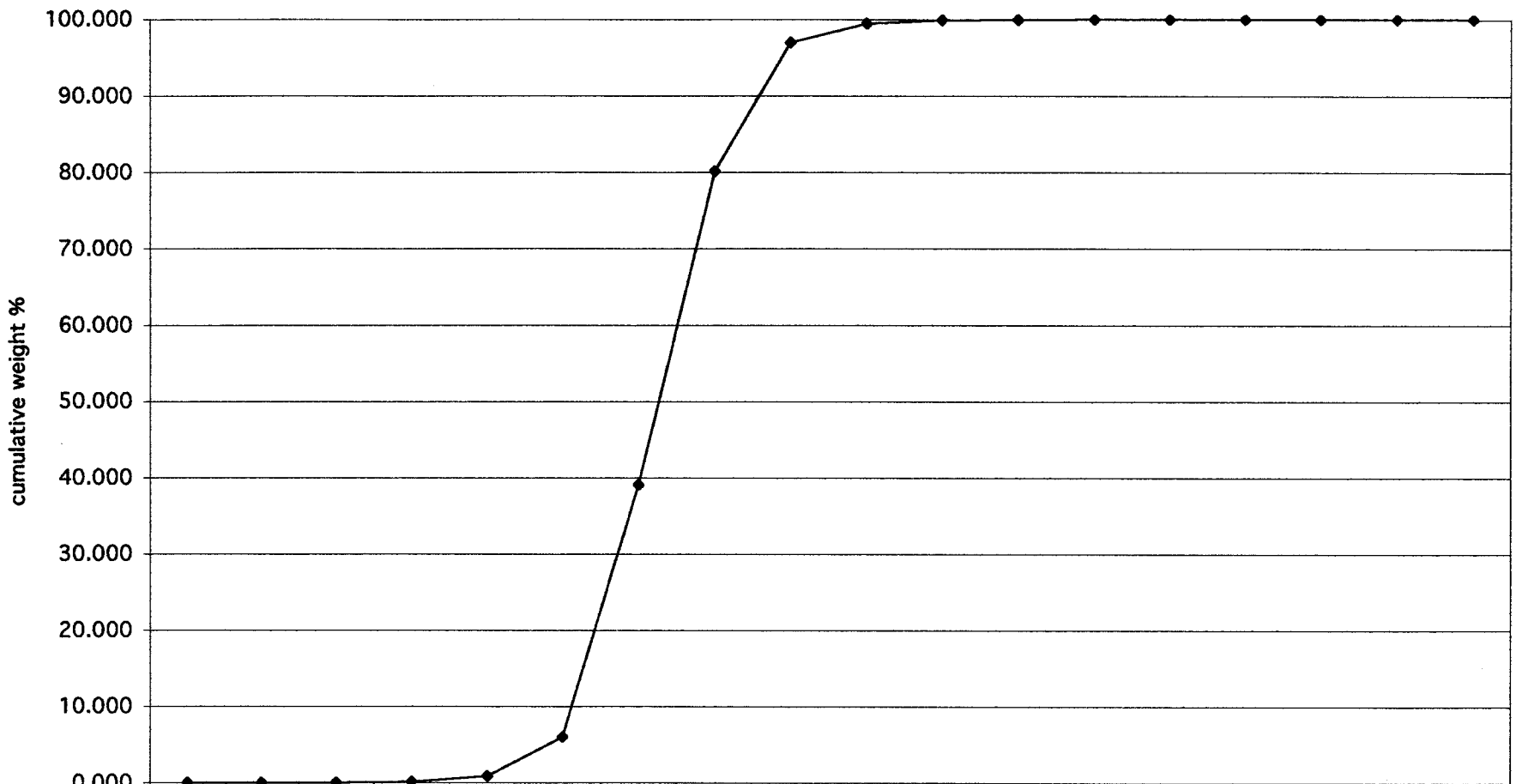

	2-1.4	1.4-1	1-.71	.71-.50	.50-.35	.35-.25	.25-.18	.18-.12	.12-.088	.088-.063	.063-.044	.044-.031	.031-.016	.016-.008	.008-.004	.004-.002	.002-.001	< .001
Series1	0.001	0.005	0.008	0.078	0.855	6.017	39.07	80.12	96.95	99.46	99.91	99.95	100.0	100.0	100.0	100.0	100.0	100.0

size (mm)

Appendix B – Scaling of flow, sediment, and bed form geometry variables

Viscosity and density of water fluctuate according to temperature. In the context of experimental sedimentology, these changes in water viscosity and density are reflected in the nature of the interaction bewteen the fluid and the bed of sediment. For example, warmer water is less dense and less viscous than colder water, it therefore be less efficient at transporting sediment. In order to correct for variation in water temperature between runs, variables were scaled using the Reynolds-Froude scale modeling technique described in Boguchwal and Southard (1990) and Southard et al. (1990).

The scale modeling equations are the following:

(A) Viscosity (μ) for a given water temperature was first determined by:

Eq. 1 $\quad$ viscosity $= (a + bT)^{-1/c}$

where $a = 0.0063676135$, $b = 0.00015647499$, $c = 0.6746423$

(B) Water density (ρ) at given temperatures were found in a physics handbook

e.g.: $\rho_{20°C} = 0.9982$, while $\rho_{10°C} = 0.9997$

(C) The various flow, sediment, and bed form variables were then scaled to 10°C.

To scale oscillation period (T) measured in seconds:

Eq. 2 $\quad T_{10°C} = T_{\text{run temp°C}} (\mu_{10°C} / \mu_{\text{run temp°C}})^{1/3} (\rho_{10°C} / \rho_{\text{run temp°C}})^{1/3}$

To scale velocity (U) measured in centimeters/second:

Eq. 3 $\quad U_{10°C} = U_{\text{run temp°C}} (\mu_{10°C} / \mu_{\text{run temp°C}})^{1/3} (\rho_{\text{run temp°C}} / \rho_{10°C})^{2/3}$

To scale length variables (L) measured in centimeters:

Eq. 4 $\quad L_{10°C} = L_{\text{run temp°C}} (\mu_{10°C} / \mu_{\text{run temp°C}})^{2/3} (\rho_{\text{run temp°C}} / \rho_{10°C})^{1/3}$

References

Boguchwal, L.A., and Southard, J.B., 1990, Bed configuration in steady unidirectional water flow. Part 1. Scale model study using fine sands: J. S. R., v. 60, p. 649-657.

Southard, J.B., Lambie, J.M., Federico, D.C., Pile, H.T., and Weidman, C.R., 1990, Experiments on bed configurations in fine sands under bidirectional purely oscillatory flow, and the origin of hummocky cross-stratification: J. Sed. Petrol., v. 60, p. 1-17.

Appendix C – Velocity profile analysis and boundary layer characterization

In an attempt to characterize the oscillatory and combined flow boundary layers, velocity profiles were measured during four of the runs (two oscillatory flow runs and two combined flow runs). Theoretically, boundary shear stress and boundary layer thickness can be calculated by estimating the apparent hydraulic roughness from velocity profile (Mathisen and Madsen 1996b). Unfortunately, due to the short length of its stem, the acoustic Doppler velocimeter probe (ADV) used to measure flow velocity had a maximum flow penetration distance of ~ 38 cm (vertical distance between the wave tunnel ceiling and the velocity sampling volume when the ADV is at its deepest position). For this reason, velocity profiles could only be measured during runs where the bed of sediment aggraded to a height sufficient to reach the ADV sampling volume area (i.e. when the crests of the largest bed forms migrated underneath the ADV). Under these extreme bed heights, it is apparent from the velocity profiles measured that the combined wave-current boundary layer did not fully develop because of flow depth limitations (our plots do not show the expected logarithmic region within the combined-flow boundary layer – see Mathisen and Madsen 1996b). These very large bed forms (heights ~ 25-27 cm), or at the very least the crest areas of these bed forms, are therefore most certainly affected by the presence of the tunnel ceiling and incapable of fully developing. We believe that this tunnel height limitation only challenges the experimental existence of reverse large ripples (heights > 25 cm). All other large-scale bed forms generated (symmetric and asymmetric ripples, hummocky bed forms) were more modest in heights (~ 15-20 cm) and many of these have been documented in natural environments (Li 2002, personal communication).

The following details: 1) velocity profile data, and 2) plots showing flow velocity as a function of the distance from the bed of sediment.

All of the velocity profiles were taken above a bed of fine sand (0.17 mm) and under an oscillation period (T) of 9.4 s. Explanation of the notation is as follows:

- S18R4: series 18, run 4
- Uo: oscillatory velocity (cm/s)
- Uu: unidirectional velocity (cm/s)

- Uc: combined flow velocity (cm/s)
- ave +20%: average of the positive (in x+ direction; same direction as the unidirectional current) top 20% of the 1500 velocity values sampled (cm/s)
- probe-bed distance: distance between the bed of sediment and the measured velocity (cm)
- distance ("y" axis of plots): distance away from the bed of sediment (cm)

References

Mathisen, P.P. and Madsen, O.S., 1996a, Waves and currents over a fixed rippled bed – 1. Bottom roughness experienced by waves in the presence and absence of currents: J. Geophys. Res., v. 101, No C7, p. 16533-16542.

Mathisen, P.P. and Madsen, O.S., 1996b, Waves and currents over a fixed rippled bed – 2. Bottom and apparent roughness experienced by currents in the presence of waves: J. Geophys. Res., v. 101, No C7, p. 16543-16550.

Velocity profile data - S15R2

S15R2 - (Uo = 100, Uu = 0); reverse large ripples

Uo (ave +20%	probe-bed distance		stem length	sand height
91.07	7.9	a	0	7.4
94.73	8.4	b	0.5	7.4
92.74	8.8	c	0.9	7.4
92.64	9.2	d	1.5	7.6
92.7	9.7	e	2	7.6
91.41	10.2	f	2.5	7.6
92.2	10.7	g	3	7.6
95.73	11.2	h	3.6	7.7
95.06	11.7	I	4.4	8
95.8	12.2	j	5.1	8.2
96.52	12.7	k	5.9	8.5
95.02	13.2	l	6.6	8.7
95.58	13.7	m	7.3	8.9
98.16	14.2	n	7.8	8.9
97.95	14.7	o	8.1	8.7
100.99	14.9	p	8.6	9
101.64	15.3	q	9.1	9.1
100.83	15.8	r	9.6	9.1
99.58	16.3	s	10.4	9.4
100.64	17.3	t	11.3	9.3
100	18.3	u	12.4	9.4
100.06	19.3	v	13	9
98.78	20.3	w	13.7	8.7

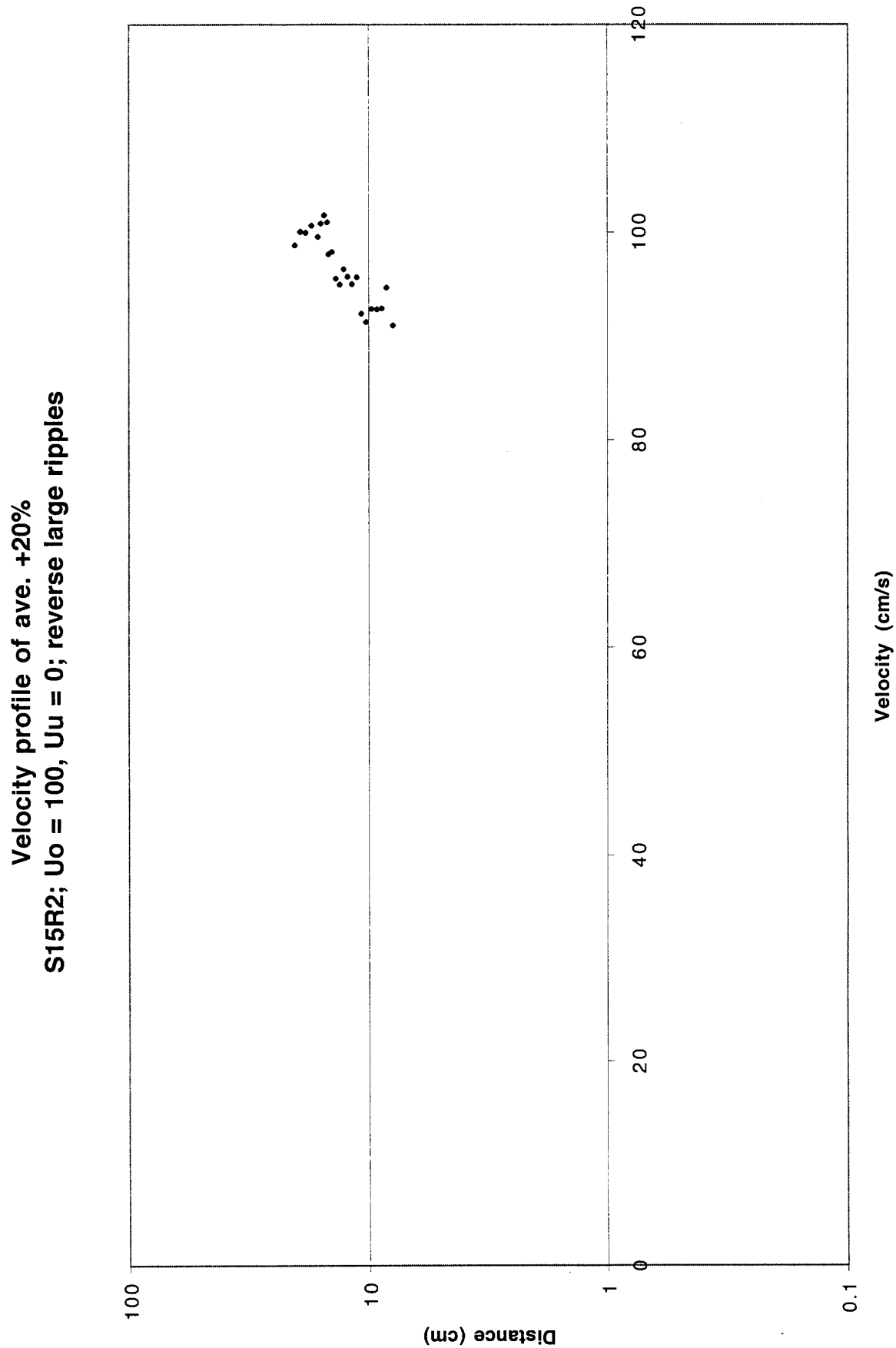
Velocity profile of ave. +20%
S15R2; Uo = 100, Uu = 0; reverse large ripples
Distance (cm)
100
10
1
0.1
0
20
40
60
80
100
120
Velocity (cm/s)

Velocity profile data - S14R1

S14R1 - (Uo = 120, Uu = 0), plane bed (higher sand)

Uo (ave +20%	probe-bed distance	stem length	sand height
146.02	4	0	15.3
148.04	4.7	1	15.6
147.57	5.3	2	16
147.62	6.3	3	16
148.21	6.8	4	16.5
149.53	7.5	5	16.8
150.75	8.4	6	16.9
156.68	8.9	7	17.4
154.06	9.2	8	18.1
155.84	10.1	9	18.2
153.8	10.8	10	18.5
155.83	11.6	11	18.7
159.46	12.5	12	18.8
156.75	13.3	13	19
154.87	14.4	14	18.9
155.02	15.4	15	18.9

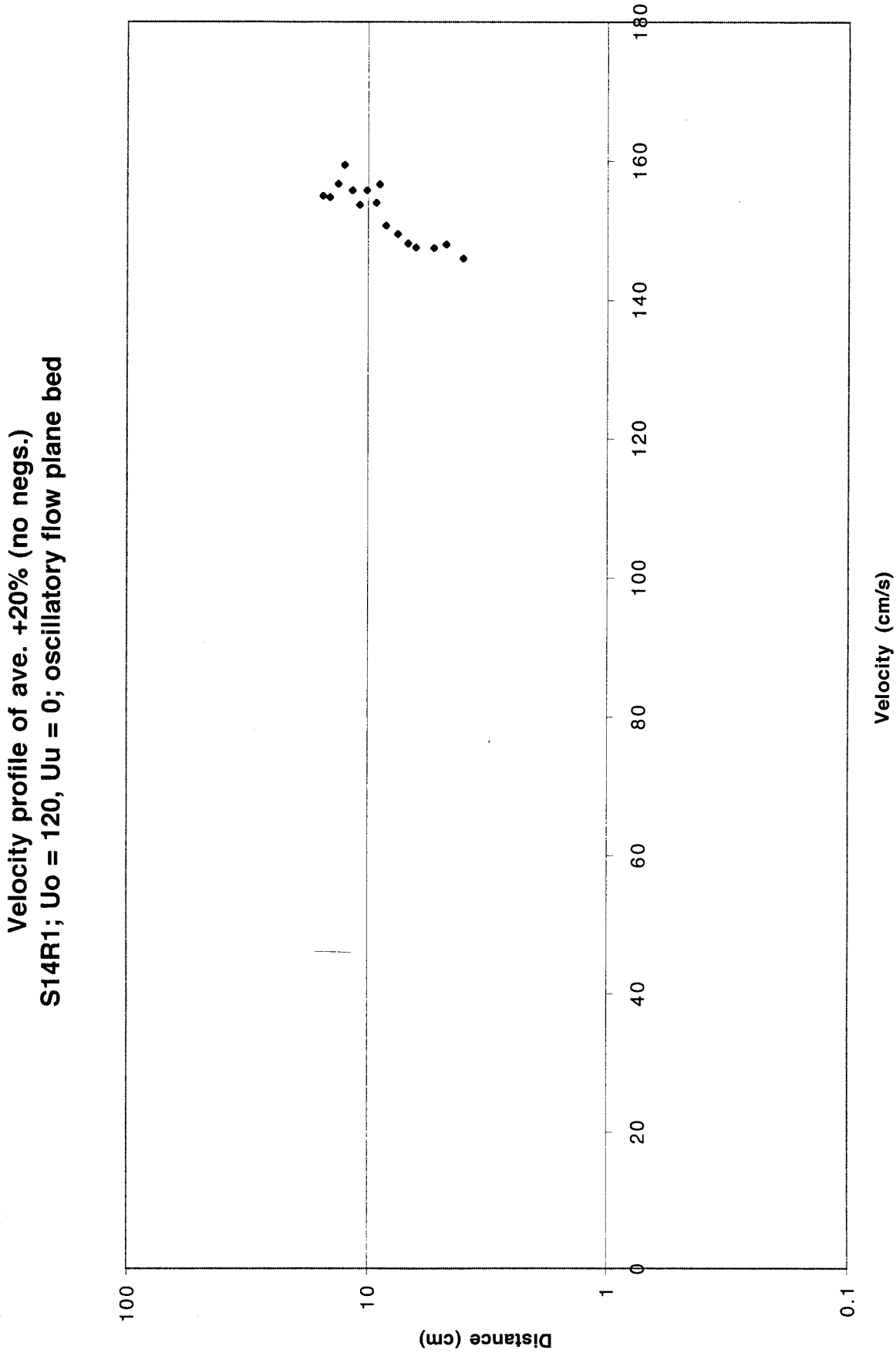
Velocity profile of ave. +20% (no negs.)
S14R1; Uo = 120, Uu = 0; oscillatory flow plane bed
Distance (cm)
100
10
1
0.1
0
20
40
60
80
100
120
140
160
180
Velocity (cm/s)

Velocity profile data - S18R4

S18R4 - (Uo = 60, Uu = 20), asymmetric large ripples

Uc (ave +20%	probe-bed distance		stem length
83.13	1.8	a	0
72.08	4.3	b	0.5
66.65	9.0	c	1
82.37	15.8	d	1.5
86.30	32.8	f	20.5
90.61	27.3	g	19
78.71	-2.8	h	2
76.69	-2.6	I	2.5
74.00	-2.0	j	3.3
61.54	-1.3	k	3.9
80.63	-0.7	l	4.6
89.54	-0.2	m	5
96.33	0.3	n	5.5
98.79	0.7	o	6
103.15	1.2	p	6.5
99.23	1.7	q	7
98.66	2.2	r	7.5
99.96	2.7	s	7.9
99.06	3.3	t	8.4
98.29	3.9	u	8.9
96.80	4.4	v	9.3
96.72	4.9	w	9.8
96.97	5.4	x	10.3
97.34	6.0	y	10.8
98.49	6.9	z	11.2
94.55	7.4	za	11.7
94.82	7.9	zb	12.1
95.40	8.4	zc	12.5
92.76	8.9	zd	13
92.87	9.4	ze	13.4
92.42	9.9	zf	13.9
93.35	10.3	zg	14.3
94.59	10.7	zh	14.7
92.36	11.2	zi	15.2

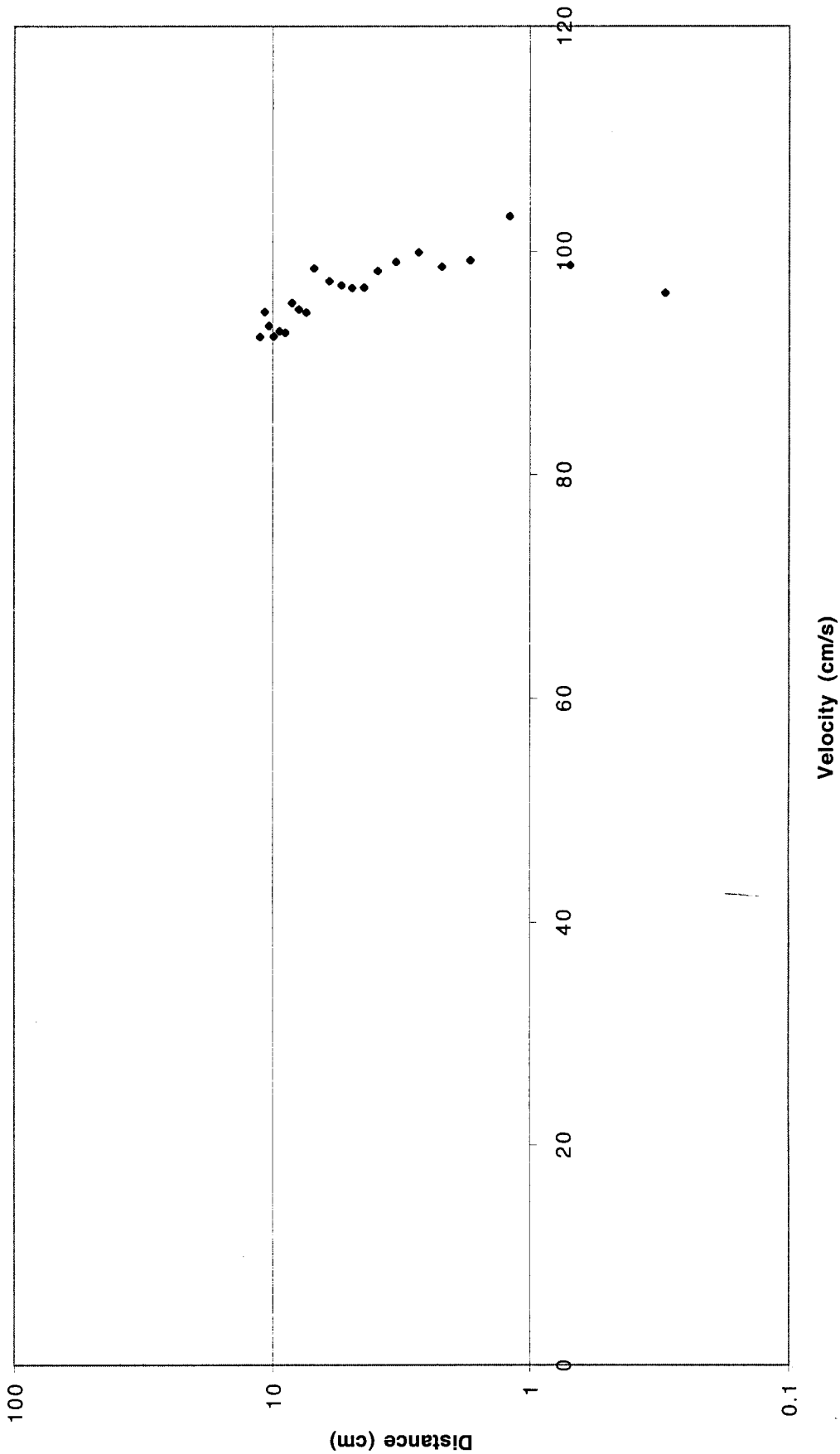
Velocity profile of ave. +20% (no negs.)
S18R4; Uo = 60, Uu = 20; combined flow large asymmetric ripples
Distance (cm)
100
10
1
0.1
0
20
40
60
80
100
120
Velocity (cm/s)

Velocity profile data - S15R5

S15R5 - (Uo = 100, Uu = 20); combined flow asymmetric large ripples

Uc (ave +20%	probe-bed distance		stem length	sand height
135.61	-5.1	a	4.5	24.9
114.42	-4.6	b	4.8	24.7
154.25	-4.1	c	5.2	24.6
138.113	-3.6	d	5.2	24.1
133.44	-3.1	e	5.7	24.1
135.66	-2.6	f	6	23.9
132.67	-2.1	g	6.1	23.5
138.11	-1.6	h	6.4	23.3
136.65	-1.1	I	6.8	23.2
145.89	-0.6	j	7.1	23
145.6	-0.1	k	7.4	22.8
147.4	0.4	l	7.5	22.4
151.13	0.9	m	8	22.4
148.98	1.4	n	8.7	22.6
152.16	1.9	o	8.6	22
149.09	2.4	p	8.8	21.7
149.73	2.9	q	9.1	21.5
148.24	3.4	r	9.6	21.5
146.54	3.9	s	9.8	21.2
144.83	4.4	t	9.8	20.7
145.64	4.9	u	10.1	20.5
143	5.4	v	10.6	20.5
142.79	5.9	w	10.6	20
144.61	6.4	x	10.9	19.8
142.76	6.9	y	11.1	19.5
142.12	7.4	z	11.3	19.2
142.73	7.9	za	11.7	19.1
141.1	8.4	zb	12.1	19
138.92	8.9	zc	12.6	19
141.43	9.4	zd	12.9	18.8
139.18	9.9	ze	13.2	18.6
137.2	10.4	zf	13.6	18.5
136.91	10.9	zg	14.1	18.5
139.25	11.4	zh	14.6	18.5
137.21	16.1	zi	19	18.2
134.56	1.8	zj	4.5	18

Velocity profile of ave. +20% (+only)
S15R5; Uo = 100, Uu = 20; combined flow asymmetric large ripples

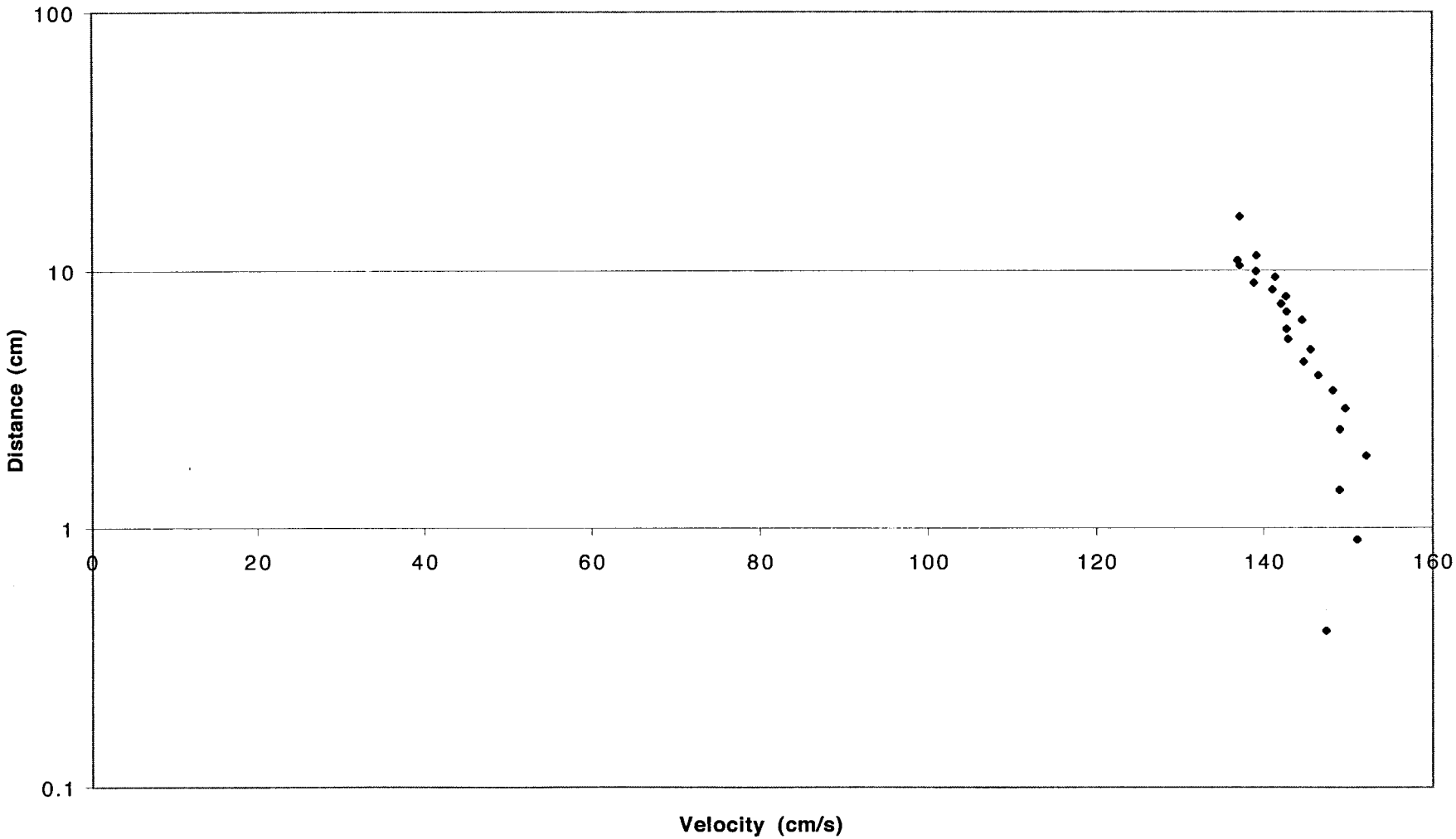

Appendix D – Ripple measurements

The following files contain the transcriptions of all ripple height, wavelength, dip angle, roundness index, and symmetry index measurements for each of the 76 runs summarized in Table 2.1. Ripple measurements that appear in Table 2.1 are simply the average values of the measurements presented in the following pages.

Ripples were measured along the 5 m long viewing windows located on either side of the wave tunnel (see Fig. 2.1). For runs where large-scale bed forms were the equilibrium bed forms, all ripples were measured. For runs where small scale ripples were the equilibrium bed forms, all ripples of the right downstream window and left upstream window were measured. For the preliminary runs of Series 2 and 3, measurements are limited to estimates of average wavelength, height and dip.

Appendix D provides the following information:

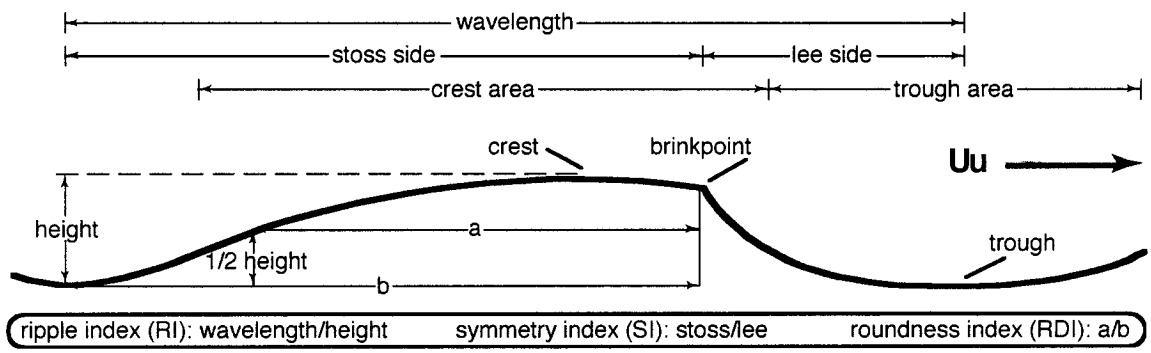

1. stoss side length: horizontal distance from the deepest point of the upstream trough (the ripple's trough that is the closest to the source of unidirectional flow) to the ripple's brink point.

2. les side length: horizontal distance from the brink point to the deepest point of the downstream trough (the ripple's trough farthest away from the source of unidirectional flow)

Note: the ripple wavelength is then calculated by adding both the stoss and lee side lengths.

3. Height of stoss side: vertical distance from deepest point of upstream trough to highest point of ripple crest.

4. Height of lee side: vertical distance from deepest point of downstream trough to highest point of ripple crest.

Note: the ripple height is then calculated by averaging the height of the stoss and lee sides. The ripple index (RI) is calculated by dividing ripple wavelength by ripple height.

5. Dip angle of stoss side: angle of dip of the stoss side (in degrees). If the dip angle fluctuates along the face, a range of values may be indicated.

6. Dip angle of lee side: angle of dip of the lee side (in degrees). Usually taken as the steepest part of the face. If the dip angle fluctuates along the face, a range of values may be indicated.

7. Roundness index (RDI): ratio of the horizontal length of the stoss side at half the ripple height to the full-horizontal length of the stoss side (a/b in the above figure).

8. Symmetry index (SI): ratio of the horizontal length of the stoss side to the horizontal length of the lee side.

Ripple measurements

S2R1

HEIGHT (cm)	WAVELENGTH (cm)	DIP ANGLE		ROUNDNESS	SYMMETRY
		stoss	*lee*	*RDI*	*SI*
1.3	8.0		18	/	/

S2R2

HEIGHT (cm)	WAVELENGTH (cm)	DIP ANGLE		ROUNDNESS	SYMMETRY
		stoss	*lee*	*RDI*	*SI*
0.5	6.5	10	11	/	/

S2R3

HEIGHT (cm)	WAVELENGTH (cm)	DIP ANGLE		ROUNDNESS	SYMMETRY
		stoss	*lee*	*RDI*	*SI*
0.4	6.5			/	/

S2R4
Plane bed

HEIGHT (cm)		WAVELENGTH (cm)		DIP ANGLE		ROUNDNESS	SYMMETRY
stoss	*lee*	*stoss*	*lee*	*stoss*	*lee*	*RDI*	*SI*
n/a	n/a	n/a	n/a	n/a	n/a	n/a	n/a

S3R1

HEIGHT (cm)	WAVELENGTH (cm)	DIP ANGLE		ROUNDNESS	SYMMETRY
		stoss	*lee*	*RDI*	*SI*
12.1	160.4	10 to 15	20 to 25	/	/

S3R2

HEIGHT (cm)	WAVELENGTH (cm)	DIP ANGLE		ROUNDNESS	SYMMETRY
		stoss	*lee*	*RDI*	*SI*
18.1	139.9	9	27	/	/

S4R1
Plane bed

HEIGHT (cm)		WAVELENGTH (cm)		DIP ANGLE		ROUNDNESS	SYMMETRY
stoss	*lee*	*stoss*	*lee*	*stoss*	*lee*	*RDI*	*SI*
n/a	n/a	n/a	n/a	n/a	n/a	n/a	n/a

S4R2
Plane bed

HEIGHT (cm)		WAVELENGTH (cm)		DIP ANGLE		ROUNDNESS	SYMMETRY
stoss	*lee*	*stoss*	*lee*	*stoss*	*lee*	*RDI*	*SI*
n/a	n/a	n/a	n/a	n/a	n/a	n/a	n/a

S4R3
Plane bed

HEIGHT (cm)		WAVELENGTH (cm)		DIP ANGLE		ROUNDNESS	SYMMETRY
stoss	*lee*	*stoss*	*lee*	*stoss*	*lee*	*RDI*	*SI*
n/a	n/a	n/a	n/a	n/a	n/a	n/a	n/a

S4R4
Plane bed

HEIGHT (cm)		WAVELENGTH (cm)		DIP ANGLE		ROUNDNESS	SYMMETRY
stoss	*lee*	*stoss*	*lee*	*stoss*	*lee*	*RDI*	*SI*
n/a	n/a	n/a	n/a	n/a	n/a	n/a	n/a

S4R5
Plane bed

HEIGHT (cm)		WAVELENGTH (cm)		DIP ANGLE		ROUNDNESS	SYMMETRY
stoss	*lee*	*stoss*	*lee*	*stoss*	*lee*	*RDI*	*SI*
n/a	n/a	n/a	n/a	n/a	n/a	n/a	n/a

S4R6
Plane bed

HEIGHT (cm)		WAVELENGTH (cm)		DIP ANGLE		ROUNDNESS	SYMMETRY
stoss	*lee*	*stoss*	*lee*	*stoss*	*lee*	*RDI*	*SI*
n/a	n/a	n/a	n/a	n/a	n/a	n/a	n/a

S4R6b
Plane bed

HEIGHT (cm)		WAVELENGTH (cm)		DIP ANGLE		ROUNDNESS	SYMMETRY
stoss	*lee*	*stoss*	*lee*	*stoss*	*lee*	*RDI*	*SI*
n/a	n/a	n/a	n/a	n/a	n/a	n/a	n/a

S5R1

HEIGHT (cm)	WAVELENGTH (cm)	DIP ANGLE		ROUNDNESS	SYMMETRY
		stoss	*lee*	*RDI*	*SI*
8.0	140.0	10	14	0.43	1.72
12.0	156.0	11	25	0.75	1.14
18.5	173.0	11	26	0.72	1.67
17.3	183.0	11	24	0.28	0.99
13.5	154.0	2	25	0.36	1.91
10.5	200.0	9	22		
13.0	188.0	14	16	n = 5	
16.8	132.0	19	20		
12.5	158.0	15			
7.5			n = 8		
	n = 9				
n = 10					

S5R2

HEIGHT (cm)	WAVELENGTH (cm)	DIP ANGLE		ROUNDNESS	SYMMETRY
		stoss	*lee*	*RDI*	*SI*
3.0	137.0	1	5	0.46	1.05
4.1	173.0	1	3	0.88	1.41
8.0	151.0	7	9	0.73	2.58
11.6	155.0	5	15	0.44	1.49
11.6	204.0	5	18	0.72	2.62
15.2	143.0	2	5		
17.0	154.5	4	25	n = 5	
9.4	150.3	5	20		
9.7	145.0	19	20		
7.5	130.5	18	20		
4.5	132.6	14	25		
		7	12		
n = 11		8	10		
		5			
			n = 13		
		n = 14			

S5R2b

HEIGHT (cm)		WAVELENGTH (cm)	DIP ANGLE		ROUNDNESS	SYMMETRY
stoss	*lee*		*stoss*	*lee*	*RDI*	*SI*
		75.0	0	2	0.51	0.86
9.5	6.5	175.0	8	4	0.70	0.98
2.0	3.2	116.0	3	10	0.47	0.85
5.2	6.0	183.0	9	4	0.54	0.94
4.0	5.0		2	5		
		n = 4		4	n = 4	
n = 5			n = 5			
				n = 6		

S5R3

HEIGHT (cm)		WAVELENGTH (cm)	DIP ANGLE		ROUNDNESS	SYMMETRY
stoss	*lee*		*stoss*	*lee*	*RDI*	*SI*
2.5	5.6	61.5	4	12	0.15	0.81
7.1	3.7	72.0	15	9	0.36	2.21
13.1	12.0	176.0	9	15	0.35	1.13
17.7	13.9	148.0	30	7	0.38	1.01
11.4	11.0	89.5	23	20	0.33	0.95
10.5	11.1	75.5	20	20		
8.6	8.4	84.0	17	17	n = 5	
7.9	7.8	76.0	17	14		
7.2	6.9	63.5	11	13		
4.0	4.6	53.0				
			n = 9			
n = 10						

S5R3b

HEIGHT (cm)		WAVELENGTH (cm)	DIP ANGLE		ROUNDNESS	SYMMETRY
stoss	*lee*		*stoss*	*lee*	*RDI*	*SI*
3.5	8.5	118.0	6	5	0.55	1.53
14.0	15.0	147.0	11	26	0.54	1.90
15.5	11.0	121.0	9	24	0.45	1.49
13.5	13.0	129.0	7	26	0.45	2.77
9.5	9.5	89.0	12	20	0.38	1.63
7.5	5.5	59.0	14	20	0.45	1.04
5.0	5.0	63.0	10	15		
5.0				13	n = 6	
	n = 7			19		
n = 8						
				n = 9		

S5R4
Plane bed

HEIGHT (cm)		WAVELENGTH (cm)		DIP ANGLE		ROUNDNESS	SYMMETRY
stoss	*lee*	*stoss*	*lee*	*stoss*	*lee*	*RDI*	*SI*
n/a	n/a	n/a	n/a	n/a	n/a	n/a	n/a

S5R5

HEIGHT (cm)		WAVELENGTH (cm)	DIP ANGLE		ROUNDNESS	SYMMETRY
stoss	*lee*		*stoss*	*lee*	*RDI*	*SI*
5.0	10.0	155.0	10	24	/	/
11.4	12.5	250.0	3	4		
3.5	6.4	67.0	5	5		
5.7	7.5	76.0	6	11		
			7	14		
n = 4			10	11		
				11		
			n = 6			
				n = 7		

S5R5b
Plane bed

HEIGHT (cm)		WAVELENGTH (cm)		DIP ANGLE		ROUNDNESS	SYMMETRY
stoss	*lee*	*stoss*	*lee*	*stoss*	*lee*	*RDI*	*SI*
n/a	n/a	n/a	n/a	n/a	n/a	n/a	n/a

S5R6
Plane bed

HEIGHT (cm)		WAVELENGTH (cm)		DIP ANGLE		ROUNDNESS	SYMMETRY
stoss	*lee*	*stoss*	*lee*	*stoss*	*lee*	*RDI*	*SI*
n/a	n/a	n/a	n/a	n/a	n/a	n/a	n/a

S5R7

HEIGHT (cm)		WAVELENGTH (cm)	DIP ANGLE		ROUNDNESS	SYMMETRY
stoss	*lee*		*stoss*	*lee*	*RDI*	*SI*
0.8	3.4	122.0	7	8	0.24	1.40
14.0	2.0	158.0	23	18	0.69	1.07
2.7	7.0	76.0	23	16		
	12.0		18	20		
n = 3		n = 3	8	12		
	n = 4					
			n = 5			

S5R7b
Plane bed

HEIGHT (cm)		WAVELENGTH (cm)		DIP ANGLE		ROUNDNESS	SYMMETRY
stoss	*lee*	*stoss*	*lee*	*stoss*	*lee*	*RDI*	*SI*
n/a	n/a	n/a	n/a	n/a	n/a	n/a	n/a

S6R1

HEIGHT (cm)		WAVELENGTH (cm)		DIP ANGLE		ROUNDNESS	SYMMETRY
stoss	*lee*	*stoss*	*lee*	*stoss*	*lee*	*RDI*	*SI*
1.1	0.3	3.3	4.0	11	2	/	/
0.2	0.7	2.0	2.0	3	14		
0.2	0.2	2.5	1.5	2	14		
0.5	0.9	1.7	2.5	15	2		
0.9	0.2	5.0	3.2	16	14		
0.5	0.6	2.8	4.5	2	20		
0.1	1.4	3.6	2.4	10	12		
1.0	0.1	3.0	5.2	14.0	4		
1.0	0.1	3.6	1.7	14	11.0		
0.5	2.1	3.2	7.7	19	15		
0.6	0.3	3.8	3.7	13	1		
0.2	0.2	3.2	3.0	2	17		
0.1	0.2	6.6	4.7	10	21		
0.7	1.5	2.2	3.3	8	6		
0.6	0.6	2.0	1.4	25	9		
0.4	0.1	2.9	4.5	22	22		
1.2	0.4	5.0	3.5	10	30		
0.1	1.8	4.1	4.0	20	1		
0.5	0.8	5.3	2.9	2	19		
0.5	0.2	3.7	3.5	5	7		
0.3	0.3	3.1	2.2	13	10		
2.3	1.6	4.6	2.9	21	6		
0.2	0.2	3.2	3.7	9	12		
0.9	0.1	3.2	2.4	0	16		
0.1	0.4	2.7	3.1	14	21		
0.1	0.3	3.0	2.6	4	24		
1.0	1.3	2.5	3.0	8	1		
1.2	0.2	2.0	2.9	9	0		
0.2	1.1	3.7	3.6	9	28		
0.6	1.1	3.2	5.0	6	14		
1.3	0.1	3.1	3.6	14	7		
0.1	0.2	2.1	3.1	12	24		
0.1	1.6	1.8	4.0	10	19		
0.2	0.3	7.5	6.1	22	5		
0.2	0.1	2.1	2.2	5	5		
		2.1	2.3	2	29		
n = 35		5.2	5.0	14	2		

2.3	2.5	4	14
3.5	3.7	2	12
4.3	4.1	8	12
2.5	4.0	9	9
3.5	4.2	10	18
4.5	3.2	9	11
3.1	4.0	10	6
4.0	3.5	13	9
3.5	2.4	5	32
2.5	2.0		
2.5	4.0	n = 46	
4.5	3.5		
3.0	3.0		

n = 50

S6R2

HEIGHT (cm)		WAVELENGTH (cm)		DIP ANGLE		ROUNDNESS	SYMMETRY
stoss	*lee*	*stoss*	*lee*	*stoss*	*lee*	*RDI*	*SI*
0.3	0.7	3.1	4.5	7	12	/	/
0.8	0.3	4.0	3.4	13	7		
0.7	0.7	4.6	3.2	10	13		
0.4	0.2	3.2	1.6	11	5		
0.5	0.4	2.6	3.0	14	5		
0.2	0.3	2.2	2.1	7	7		
0.7	0.4	3.0	2.4	12	9		
0.5	0.2	2.6	2.2	12.0	3		
0.2	0.9	3.1	3.1	4	15.0		
0.1	0.1	2.2	1.8	5	4		
1.1	0.2	4.3	2.9	17	5		
0.2	0.6	2.5	2.4	6	19		
0.8	0.2	3.5	1.8	16	8		
0.7	0.9	3.7	2.5	11	22		
0.1	0.8	2.0	2.2	2	24		
0.8	0.2	4.1	2.9	16	4		
0.5	0.7	3.1	2.9	15	15		
0.1	1.0	3.1	3.0	4	27		
0.3	0.3	1.7	1.7	13	13		
1.9	0.4	3.7	3.7	26	6		
0.2	0.2	1.7	1.4	8	10		
0.3	0.9	3.3	3.2	6	22		
1.1	0.5	4.9	4.5	13	6		
0.3	0.3	2.3	2.3	7	13		
0.7	0.7	4.0	3.8	9	13		
0.2	0.4	2.4	1.8	6	14		
0.6	0.2	3.5	2.9	8	7		
0.1	1.0	2.7	3.1	1	23		
0.8	0.3	4.1	2.5	11	12		
0.2	0.7	2.9	4.2	4	10		
0.7	0.3	4.1	2.1	13	8		
0.2	0.1	2.8	3.2	3	24		

n = 32

S6R3

HEIGHT (cm)		WAVELENGTH (cm)		DIP ANGLE		ROUNDNESS	SYMMETRY
stoss	*lee*	*stoss*	*lee*	*stoss*	*lee*	*RDI*	*SI*
0.1	1.1	2.0	3.7	7	20	/	/
0.2	0.5	2.3	2.5	6	17		
0.4	0.5	4.9	3.0	7	12		
2.7	0.7	8.2	3.3	19	13		
0.1	3.9	2.2	3.9	4	9		
0.5	1.3	4.3	4.9	7	17		
0.2	0.4	4.1	5.5	5	4		
0.4	1.1	5.4	4.5	7.0	19		
1.0	0.1	3.2	2.3	17	3.0		
2.2	1.1	5.0	8.0	32	25		
0.6	0.2	2.3	3.4	19	5		
3.1	1.3	10.1	7.4	18	18		
2.8	1.5	6.3	4.9	24	19		
0.7	1.4	5.0	4.4	6	22		
1.5	0.3	4.9	2.6	18	8		
0.8	0.1	3.2	2.5	13	4		
0.4	0.4	3.0	7.8	10	10		
0.6	0.2	3.4	3.1	9	3		
0.6	0.5	3.3	3.7	11	8		
0.7	0.2	3.6	4.5	14	4		
0.9	0.1	2.5	4.2	22	1		
0.1	0.1	0.6	2.0	8	6		
0.2	1.2	3.3	3.5	7	21		
1.2	0.6	5.4	4.7	14	9		
0.1	0.4	1.5	2.1	2	12		
0.1	0.7	4.0	3.0	2	16		
0.2	0.6	3.5	2.6	5	15		
0.3	0.5	3.5	2.4	6	12		
0.1	0.3	2.5	2.2	3	9		
0.1	0.4	2.2	2.3	6	9		

n = 30

S6R4

HEIGHT (cm)		WAVELENGTH (cm)		DIP ANGLE		ROUNDNESS	SYMMETRY
stoss	*lee*	*stoss*	*lee*	*stoss*	*lee*	*RDI*	*SI*
0.1	0.9	2.5	3.2	5	21	/	/
2.2	0.5	10.9	2.8	16	14		
1.0	1.5	6.4	5.0	10	22		
0.9	0.6	7.2	3.1	9	14		
-0.1	1.3	5.0	5.1	-3	21		
3.9	0.8	20.0	12.3	13	6		
1.1	1.7	4.4	5.0	13	19		
5.0	0.6	9.9	3.4	30	7		
0.5	1.6	4.7	3.9	7	27		
0.3	0.6	4.1	1.7	5	18		
0.9	0.7	6.0	2.4	9	20		
1.8	1.2	7.4	3.7	8	23		
0.8	1.9	11.4	5.2	6	25		
0.2	0.7	4.3	2.4	2	18		
6.3	1.1	14.1	3.2	30	18		
0.3	1.5	2.6	6.4	5	12		
1.7	1.0	4.1	4.1	25	19		
1.2	0.8	9.2	4.2	15	13		
1.0	0.5	6.1	2.5	9	9		
0.1	0.4	4.3	1.8	2	12		
0.1	0.4	2.4	1.3	2	17		
0.9	0.5	4.1	2.9	17	11		
0.2	0.2	1.9	2.2	5	7		
0.2	0.8	2.7	3.4	5	13		
2.9	1.8	8.5	5.0	15	16		
1.7	0.5	7.9	3.4	14	8		
1.8	1.0	9.7	3.5	9	14		
0.1	0.4	3.3	2.1	1	15		
-0.2	0.5	1.5	2.0	-4	18		
-0.1	0.9	2.1	2.9	-5	20		
0.3	0.6	3.1	3.0	4	15		
0.1	0.9	2.1	4.1	-4	14		
0.5	0.9	3.4	4.6	9	12		
-0.2	0.4	2.4	1.5	-7	13		
0.4	1.5	3.4	3.9	13	27		
0.4	0.5	3.6	2.1	8	8		
1.0	0.6	4.4	2.6	14	12		
0.2	0.6	3.0	2.1	3	22		
0.5	1.5	4.3	3.2	6	28		
1.3	0.4	4.5	2.1	20	11		

n = 40

S6R5

HEIGHT (cm)		WAVELENGTH (cm)		DIP ANGLE		ROUNDNESS	SYMMETRY
stoss	*lee*	*stoss*	*lee*	*stoss*	*lee*	*RDI*	*SI*
0.2	1.1	1.5	6.3	12	24	0.49	0.79
0.1	0.2	3.1	4.2	2	6	0.78	0.85
0.1	2.2	2.7	8.0	0	27	1.00	0.68
3.6	0.8	9.6	12.3	32	8	0.93	2.39
0.9	1.6	6.3	7.4	11	25	1.14	3.70
0.4	0.4	2.5	2.6	9	13	4.10	0.50
0.3	0.6	7.9	8.2	4	14	1.76	2.10
3.2	1.2	7.5	6.8	31	19	0.53	1.50
1.1	3.2	6.3	9.3	15	28		
2.0	1.1	14.7	11.9	11	5	n = 8	
0.4	0.8	5.1	5.8	4	8		
5.3	0.8	14.2	10.0	30	7		
2.9	7.7	39.5	16.5	17	30		
0.3	0.4	2.5	3.1	11	10		
0.1	1.7	2.1	4.9	1	25		
3.7	1.0	10.0	4.3	23	16		
0.4	0.7	3.1	3.2	9	14		
2.1	0.3	5.9	3.1	25	7		
0.1	0.4	2.2	2.2	5	12		
1.0	2.0	8.8	8.2	7	18		
3.3	1.8	13.3	19.7	16	14		
2.1	1.0	18.3	4.0	14	17		
2.5	1.1	4.4	2.3	16	16		
-0.1	0.3	2.0	2.2	-2	7		
0.1	0.4	2.4	2.7	0	11		
0.2	0.6	2.4	3.3	10	13		
0.1	1.0	8.7	5.8	2	20		
2.1	2.4	12.7	3.8	18	27		
1.1	0.1	4.6	4.1	8	1		
0.2	0.7	3.9	2.4	3	12		
-0.4	0.7	1.5	2.6	-5	16		
-0.3	0.9	2.5	4.5	-9	9		
-0.3	1.1	3.7	3.8	16	8		
0.1	0.8	5.0	3.4	4	10		
0.1	1.2			2	12		
		n = 34		1	22		
n = 35							
				n = 36			

S7R1
Plane bed

HEIGHT (cm)		WAVELENGTH (cm)		DIP ANGLE		ROUNDNESS	SYMMETRY
stoss	*lee*	*stoss*	*lee*	*stoss*	*lee*	*RDI*	*SI*
n/a	n/a	n/a	n/a	n/a	n/a	n/a	n/a

S8R1

HEIGHT (cm)		WAVELENGTH (cm)		DIP ANGLE		ROUNDNESS	SYMMETRY
stoss	*lee*	*stoss*	*lee*	*stoss*	*lee*	*RDI*	*SI*
8.8	4.3	83.0	25.0	3	16	0.72	1.84
2.1	5.7	46.0	40.0	5	3	0.67	3.60
20.9	13.6	144.0	30.0	10	4	0.80	0.62
5.9	9.3	80.0	35.0	30	23	1.00	0.57
3.3	9.7	20.0	58.0	24	11	0.39	0.85
18.7	5.1	49.0	20.0	5	17	0.50	3.75
0.8	10.2	15.0	36.0	2	30		
1.7	10.5	15.0	40.0			n = 6	
19.5		150.0		n = 7			
	n = 8		n = 8				
n = 9		n = 9					

S8R2

HEIGHT (cm)		WAVELENGTH (cm)		DIP ANGLE		ROUNDNESS	SYMMETRY
stoss	*lee*	*stoss*	*lee*	*stoss*	*lee*	*RDI*	*SI*
17.3	10.1	207.0	39.0	6	30	0.67	5.31
7.3	15.3	43.0	28.0	11	29	0.85	1.54
9.5	4.5	84.0	21.0	6	12	0.15	2.44
4.9	14.4	66.0	27.0	5	30		3.21
11.2	1.7	166.0	14.0	7	6	n = 3	
25.7	17.1	95.0	36.0	14	24		n = 4
18.8	18.2	72.0	33.0	5	28		
	22.7	138.0	43.0	5	30		
n = 7	9.8	196.0	32.0	4	22		
	n = 9						

S8R3

HEIGHT (cm)		WAVELENGTH (cm)		DIP ANGLE		ROUNDNESS	SYMMETRY
stoss	*lee*	*stoss*	*lee*	*stoss*	*lee*	*RDI*	*SI*
9.6	13.6	102.0	30.0	5	29	/	/
17.1	12.1	101.0	33.0	5	23		
10.0	7.0	110.0	19.0	5	30		
16.8	13.8	107.0	35.0	6	29		
5.0	5.0	90.0	38.0	15			
15.8	14.8	58.0	39.0		n = 4		
				n = 5			
n = 6							

S9R1
Plane bed

HEIGHT (cm)		WAVELENGTH (cm)		DIP ANGLE		ROUNDNESS	SYMMETRY
stoss	*lee*	*stoss*	*lee*	*stoss*	*lee*	*RDI*	*SI*
n/a	n/a	n/a	n/a	n/a	n/a	n/a	n/a

S9R2
Plane bed

HEIGHT (cm)		WAVELENGTH (cm)		DIP ANGLE		ROUNDNESS	SYMMETRY
stoss	*lee*	*stoss*	*lee*	*stoss*	*lee*	*RDI*	*SI*
n/a	n/a	n/a	n/a	n/a	n/a	n/a	n/a

S9R3
Plane bed

HEIGHT (cm)		WAVELENGTH (cm)		DIP ANGLE		ROUNDNESS	SYMMETRY
stoss	*lee*	*stoss*	*lee*	*stoss*	*lee*	*RDI*	*SI*
n/a	n/a	n/a	n/a	n/a	n/a	n/a	n/a

S10R1
Large ripples

HEIGHT (cm)		WAVELENGTH (cm)		DIP ANGLE		ROUNDNESS	SYMMETRY
stoss	*lee*	*stoss*	*lee*	*stoss*	*lee*	*RDI*	*SI*
5.7	7.1	31.0	42.0	13	13	0.51	1.02
6.6	7.8	43.0	42.0	12	12	0.42	0.95
10.8	10.9	40.0	45.0	18	14	0.42	1.35
10.9	10.5	41.0	43.0	12	15	0.40	1.02
8.3	5.7	58.0	60.0	8	15	0.52	0.80
10.2	11.6	47.0	46.0	22	12		
		41.0	51.0	19		n = 5	
n = 6				16	n = 6		
		n = 7					
				n = 8			

S10R1
Small ripples

HEIGHT (cm)		WAVELENGTH (cm)		DIP ANGLE		ROUNDNESS	SYMMETRY
stoss	*lee*	*stoss*	*lee*	*stoss*	*lee*	*RDI*	*SI*
0.1	0.3	1.8	2.2	2	17	/	/
0.0	1.8	2.5	5.9	1	9		
-0.2	2.5	3.1	7.4	-5	20		
0.4	2.5	6.0	8.9	6	15		
1.1	-0.2	6.8	5.4	10	-1		
1.5	-0.2	6.4	3.7	14	-4		
0.9	0.0	4.6	3.6	10	0		
0.3	0.1	3.0	2.5	14	2		
0.6	0.1	3.4	3.7	9	4		
0.2	0.1	2.3	2.8	9	4		
0.3	0.3	2.9	3.4	8	7		
0.1	0.2	2.4	2.1	5	7		
0.2	0.4	2.6	3.5	8	8		
0.1	0.4	2.3	3.0	4	10		
0.1	0.6	2.7	3.7	4	8		
0.1	0.5	2.5	3.3	4	7		
0.2	0.4	2.9	3.2	7	5		
0.2	0.3	2.5	3.3	8	3		
0.2	0.4	2.2	4.8	8	6		
0.2	0.4	2.4	3.5	8	7		
0.4	-0.1	7.4	2.4	12	5		
0.1	0.9	2.9	4.5	2	16		
0.1	0.1	1.9	2.9	7	7		
0.3	0.2	3.0	3.3	7	8		
0.2	0.0	2.6	2.6	7	0		
0.5	0.1	3.3	2.7	13	4		
1.5	0.0	5.6	2.5	13	0		
1.7	0.0	5.3	2.7	20	0		
1.0	0.1	4.7	2.5	13	2		
0.7	0.3	4.0	2.6	11	9		
0.1	0.6	3.6	2.9	3	16		
-0.1	0.7	4.0	3.1	-2	20		
-0.1	0.6	2.1	2.1	-5	16		

n = 33

S10R2
Large ripples

HEIGHT (cm)		WAVELENGTH (cm)		DIP ANGLE		ROUNDNESS	SYMMETRY
stoss	*lee*	*stoss*	*lee*	*stoss*	*lee*	*RDI*	*SI*
5.5	6.0	38.0	53.0	12	15	0.58	0.72
9.2	8.5	58.0	58.0	15	10	0.68	1.17
10.0	11.0	38.0	34.0	20	20	0.62	0.57
7.0	4.2	49.0	42.0	11	15	0.49	0.81
5.7	9.0	24.0	41.0	8	9		
7.8	6.2	41.0	40.0	14	13	n = 4	
7.5	2.8	62.0	42.0	15	15		
10.3	9.0	39.0	36.0	18	20		
8.6	10.8	35.0	33.0	19	14		
	6.6		68.0	19	11		
n = 9		n = 9	43.0				
	n = 10			n = 10			
			n = 11				

S10R2
Small ripples

HEIGHT (cm)	WAVELENGTH (cm)		DIP ANGLE		ROUNDNESS	SYMMETRY
	stoss	*lee*	*stoss*	*lee*	*RDI*	*SI*
~ 0.3	6.5	5.3	/	/	/	/
(< 0.5)	6.0	7.3				
	6.0	6.5				
	6.2	9.2				
	8.3	7.4				
	7.1	9.0				
	5.7	6.5				
	5.8	5.5				
	5.3	5.8				
	6.0	6.0				
	7.7	8.0				
	7.5	5.5				
	5.2	5.3				
	n = 13					

S10R3
Large ripples

HEIGHT (cm)		WAVELENGTH (cm)		DIP ANGLE		ROUNDNESS	SYMMETRY
stoss	*lee*	*stoss*	*lee*	*stoss*	*lee*	*RDI*	*SI*
7.8	8.2	55.2	33.4	10	27	0.52	1.65
4.4	5.0	30.8	15.0	18	30	0.63	1.52
9.1	8.5	65.0	14.5	20	29	0.40	4.48
6.6	11.0	49.0	33.0	27	22	0.60	1.49
11.9	9.4	80.0	38.4	11		0.68	1.30
					n = 4		
n = 5						n = 5	

S10R3
Small ripples

HEIGHT (cm)		WAVELENGTH (cm)		DIP ANGLE		ROUNDNESS	SYMMETRY
stoss	*lee*	*stoss*	*lee*	*stoss*	*lee*	*RDI*	*SI*
0.7	0.1	3.9	2.1	15	3	/	/
0.3	0.1	3.2	1.8	8	2		
0.4	0.2	5.3	2.9	7	5		
0.2	0.7	6.2	3.0	3	18		
-0.1	0.6	4.7	2.3	-3	16		
0.1	0.3	1.9	2.8	1	11		
1.6	0.1	7.0	3.4	14	2		
0.8	0.1	5.7	2.5	12	3		
0.1	0.2	5.0	1.7	2	5		
0.0	0.5	6.3	3.0	1	13		
0.1	0.3	3.9	2.7	2	9		
0.1	0.2	4.2	3.0	3	4		
0.4	0.2	5.8	3.4	4	7		
0.4	0.1	3.7	3.7	11	3		
0.1	0.1	3.0	2.9	7	4		
0.1	0.2	3.4	3.1	4	9		
0.3	0.1	2.7	3.1	9	2		
0.5	0.2	3.5	1.9	10	6		
0.3	0.2	3.3	2.3	5	12		
2.1	0.1	5.1	2.2	27	5		
0.6	0.1	3.6	1.5	14	5		
1.2	-0.1	3.9	2.1	20	5		
0.6	0.1	3.9	2.0	10	1		
0.8	-0.1	5.7	3.9	10	3		
0.4	0.0	4.1	6.0	11	2		
0.2	0.1	2.4	1.5	11	4		

n = 26

S10R4
Large ripples

HEIGHT (cm)		WAVELENGTH (cm)		DIP ANGLE		ROUNDNESS	SYMMETRY
stoss	*lee*	*stoss*	*lee*	*stoss*	*lee*	*RDI*	*SI*
11.2	15.6	122.0	25.0	4	29	0.67	4.88
19.3	14.3	112.0	50.0	7 to 25	27	0.50	4.15
9.3	5.8	54.0	13.0	5 to 13	25	0.58	5.66
10.8	6.0	64.0	11.0	3 to 11	25	0.89	1.65
1.6	9.9	33.0	20.0				
				n = 4			
n = 5							

S10R4
Small ripples

HEIGHT (cm)		WAVELENGTH (cm)		DIP ANGLE		ROUNDNESS	SYMMETRY
stoss	*lee*	*stoss*	*lee*	*stoss*	*lee*	*RDI*	*SI*
0.1	0.1	6.1	3.4	6	6	/	/
0.0	0.4	1.5	3.7	0	11		
0.1	0.2	3.5	1.5	2	4		
0.2	0.7	3.8	3.1	6	11		
0.1	0.5	2.6	2.8	6	9		
0.1	0.4	2.4	3.0	7	11		
0.3	0.3	3.1	2.4	11	10		
0.5	0.6	4.0	3.2	8	11		
0.4	0.6	6.0	4.2	5	12		
0.7	0.3	11.4	4.1	3	5		
0.2	0.2	2.8	3.0	6	8		
0.3	0.1	2.0	3.6	7	7		
0.5	0.1	2.4	3.2	17	2		
0.3	0.1	2.8	2.9	9	9		
0.5	0.3	4.5	4.0	7	10		
n = 15							

S10R5
Large ripples

HEIGHT (cm)		WAVELENGTH (cm)		DIP ANGLE		ROUNDNESS	SYMMETRY
stoss	*lee*	*stoss*	*lee*	*stoss*	*lee*	*RDI*	*SI*
14.2	10.4	177.0	25.0	9	30	0.75	5.48
11.0	11.0	55.0	19.0	10 to 18	24	0.73	2.89
5.5	6.5	15.0	18.0	16	28	0.59	2.95
8.3	12.1	98.0	32.0	4 to 12	22		
12.6	11.3	59.0	20.0	10	21		
		81.0					
n = 5			n = 5				
		n = 6					

S10R5
Small ripples

HEIGHT (cm)		WAVELENGTH (cm)		DIP ANGLE		ROUNDNESS	SYMMETRY
stoss	*lee*	*stoss*	*lee*	*stoss*	*lee*	*RDI*	*SI*
0.3	0.4	10.2	3.8	16	11	/	/
0.8	1.0	9.0	2.6	8	19		
0.2	2.4	13.5	3.9	15	28		
0.2	1.0	3.9	7.9	7	11		
0.3	0.2	4.1	4.0	6	11		
0.3	0.1	3.9	4.0	3	9		
0.7	0.7	2.5	2.2	7	3		
0.3	0.3	3.4	0.8	15	1		
0.2	0.7	3.2	5.0	13	4		
0.2		3.1	3.4	0	12		
	n = 9	5.1	6.2	5	7		
n = 10				4	6		
		n = 11		0	8		
				n =13			

S10R6 # ripples (n) = 5
Large ripples

HEIGHT (cm)		WAVELENGTH (cm)		DIP ANGLE		ROUNDNESS	SYMMETRY
stoss	*lee*	*stoss*	*lee*	*stoss*	*lee*	*RDI*	*SI*
7.9	10.9	74	22	12	30	0.58	3.36
13.1	10.6	47	28	11	31	0.61	6.46
6.8	6.4	91	17	10	28	0.61	2.14
15.7	10.8		22	8	33		4.55
	12.2	n = 3	20		32	n = 3	
n = 4				n = 4			n = 4
	n = 5		n = 5		n = 5		

S10R6
Small ripples

HEIGHT (cm)		WAVELENGTH (cm)		DIP ANGLE		ROUNDNESS	SYMMETRY
stoss	*lee*	*stoss*	*lee*	*stoss*	*lee*	*RDI*	*SI*
0.4	0.4	6.1	3.3	6	6	/	/
0.3	0.8	4.6	3.5	8	8		
0.6	0.7	8.1	3.7	6	12		
0.1	0.5	2.5	2.5	4	11		
0.2	0.1	4.5	4.1	2	4		
0.3	0.2	4.0	4.2	4	5		
0.4	0.2	5.3	3.5	5	9		
0.2	0.2	3.0	1.7	6	6		
0.2	0.3	1.8	2.3	4	5		
0.2	0.2	4.0	2.2	3	8		
0.3	0.2	4.2	2.2	3	4		
0.2	0.2	5.0	2.7	4	5		
0.2	0.2	5.8	4.0	5	3		
0.3	0.3	4.8	3.2	6	8		
0.2	0.3	4.7	2.1	3	6		
0.2	0.2	5.4	2.3	5	4		
1.0	0.6	9.1	4.1	8	17		
0.9	1.1	13.2	5.2	10	16		
0.9	0.2	6.8	2.0	6	7		
0.1	0.2	1.1	2.9	4	2		
0.8	0.7	4.3	3.5	12	11		
0.3	0.2	3.3	1.1	4	17		

n = 22

S11R1

HEIGHT (cm)		WAVELENGTH (cm)		DIP ANGLE		ROUNDNESS	SYMMETRY
stoss	*lee*	*stoss*	*lee*	*stoss*	*lee*	*RDI*	*SI*
10.0	11.1	90.0	106.0	13	7	0.37	0.85
12.9	10.4	42.0	56.0	18	18	0.36	0.75
5.6	8.6	27.0	48.0	19	15	0.43	0.56
11.3	8.3	35.0	33.0	20	16	0.35	1.06
17.2	8.6	24.0	15.0	17	14	0.30	0.77
9.2	10.6	48.0	47.0	13	18	0.47	1.81
11.7	8.5	63.0	82.0	10	11		1.90
	14.4	69.0	38.0	7	23	n = 6	
n = 7	3.7	72.0	38.0		7		n = 7
				n = 8			
	n = 9				n = 9		

S11R2

HEIGHT (cm)		WAVELENGTH (cm)		DIP ANGLE		ROUNDNESS	SYMMETRY
stoss	*lee*	*stoss*	*lee*	*stoss*	*lee*	*RDI*	*SI*
8.0	8.0	68.0	30.0	15	23	0.45	2.27
11.7	12.6	65.0	46.0	12	21	0.55	1.41
11.6	11.6	81.0	44.0	9	23	0.53	1.84
15.6	13.7	72.0	38.0	9	26	0.42	1.90
12.9	8.3	61.0	35.0	10	22		
13.0				11		n = 4	
	n = 5				n = 5		
n = 6				n = 6			

S11R3

HEIGHT (cm)		WAVELENGTH (cm)		DIP ANGLE		ROUNDNESS	SYMMETRY
stoss	*lee*	*stoss*	*lee*	*stoss*	*lee*	*RDI*	*SI*
13.6	15.6	270.0	30.0	4	26	0.95	9.00

S11R4

HEIGHT (cm)		WAVELENGTH (cm)		DIP ANGLE		ROUNDNESS	SYMMETRY
stoss	*lee*	*stoss*	*lee*	*stoss*	*lee*	*RDI*	*SI*
29.5	20.5	19.0	4.0	5	32	/	/

S11R5
Plane bed

HEIGHT (cm)		WAVELENGTH (cm)		DIP ANGLE		ROUNDNESS	SYMMETRY
stoss	*lee*	*stoss*	*lee*	*stoss*	*lee*	*RDI*	*SI*
n/a	n/a	n/a	n/a	n/a	n/a	n/a	n/a

S11R6
Plane bed

HEIGHT (cm)		WAVELENGTH (cm)		DIP ANGLE		ROUNDNESS	SYMMETRY
stoss	*lee*	*stoss*	*lee*	*stoss*	*lee*	*RDI*	*SI*
n/a	n/a	n/a	n/a	n/a	n/a	n/a	n/a

S12R1

HEIGHT (cm)		WAVELENGTH (cm)		DIP ANGLE		ROUNDNESS	SYMMETRY
stoss	*lee*	*stoss*	*lee*	*stoss*	*lee*	*RDI*	*SI*
1.1	0.1	4.9	3.6	17.0	18.0		
0.0	0.1	1	1	0	7		
0.6	0.4	3.7	1.9	16	18		
1.1	1.4	5.7	4.8	18	21		
1.1	1.2	3.9	6.8	21	18		
0.1	0.0	1.5	1.2	4	0		
0.4	0.6	4.0	2.6	12	21		
1.3	1.2	4.8	5.0	20	24		
0.2	0.2	2.4	2.2	8	8		
0.9	0.9	3.5	3.5	18	21		
0.2	0.1	2.2	2.1	11	3		
1.2	1.2	4.4	4.5	21	25		
1.4	1.3	4.4	6.4	25	20		
0.1	0.1	1.7	2.1	4	3		
1.1	1.1	4.1	5.3	19	19		
0.3	0.5	2..4	3.9	14	12		
1.0	1.0	3.8	4.3	18	19		
1.3	0.7	3.7	5.4	29	13		
0.1	0.2	1.8	3.0	7	8		
1.6	1.4	4.8	4.8	18	18		
0.4	0.2	2.0	1.7	16	9		
0.3	0.5	2.0	2.1	13	26		
1.1	0.4	3.0	2.1	28	13		
0.3	1.1	1.9	4.3	12	22		
1.3	0.7	4.1	5.5	24	18		
1.1	1.1	5.0	3.7	20	26		
0.9	1.1	4.6	3.2	18	25		
0.9	0.5	3.5	2.9	25	18		
1.0	0.6	4.7	2.7	20	17		
0.3	0.7	2.4	4.2	10	12		
1.2	1.2	3.5	3.9	26	23		
0.3	0.3	2.9	2.3	14	16		
0.9	1.0	3.7	3.4	18	20		
0.6	0.9	3.0	3.7	15	20		
0.9	0.8	3.3	2.8	23	22		
0.4	0.5	2.7	2.6	13	17		
1.0	1.3	5.0	5.2	22	23		
0.6	0.8	3.5	2.8	15	25		
0.8	0.6	3.0	2.5	22	19		
0.3	0.8	2.4	2.3	19	30		

n = 40

S12R2

HEIGHT (cm)		WAVELENGTH (cm)		DIP ANGLE		ROUNDNESS	SYMMETRY
stoss	*lee*	*stoss*	*lee*	*stoss*	*lee*	*RDI*	*SI*
1.0	1.3	3.5	4.7	20	22	n/a	n/a
0.1	0.0	3.3	1.1	4	0		
0.8	1.8	3.8	5.1	16	25		
0.1	0.2	3.9	2.0	1	8		
1.2	1.6	4.5	6.2	14	20		
0.2	0.0	3.3	1.1	4	0		
1.2	1.1	4.5	4.2	19	19		
1.3	2.3	5.2	9.1	16	22		
1.8	0.1	5.5	2.0	27	4		
0.6	2.0	7.1	5.3	14	30		
1.1	1.5	7.5	7.0	12	23		
0.5	0.8	2.8	2.1	8	33		
0.1	0.7	2.0	1.9	3	26		
1.2	0.6	5.0	2.4	22	15		
0.7	1.2	3.4	3.5	14	26		
0.1	0.1	2.5	1.5	1	1		
1.3	1.4	6.5	3.8	16	28		
1.7	0.9	5.3	4.7	24	14		
0.0	0.7	1.7	3.6	0	20		
1.2	1.4	4.6	5.4	19	16		
1.5	1.0	4.5	6.8	28	15		
1.1	1.5	5.7	5.4	17	28		
1.1	0.2	4.6	2.0	17	11		
1.5	1.2	4.5	5.5	23	18		
0.3	0.3	2.0	2.5	19	9		
0.0	0.5	0.8	1.7	4	27		
0.9	1.0	3.9	3.1	17	27		
1.5	1.0	5.6	4.5	20	21		
1.0	0.1	5.5	1.9	21	6		
0.9	1.9	4.4	4.1	12	24		
-0.1	1.1	1.3	4.1	-6	23		
0.9	0.7	3.5	3.5	20	20		
1.8	0.5	3.8	4.3	27	13		
1.5	0.9	5.3	4.6	22	22		
0.2	0.3	3.5	2.1	12	18		
1.1	1.5	5.5	4.4	17	27		
0.2	0.1	3.7	0.8	7	18		
0.7	1.7	5.6	4.0	16	31		
1.7	0.1	5.9	1.5	22	7		
0.8	1.6	3.3	4.8	17	29		

n = 40

S12R3

HEIGHT (cm)		WAVELENGTH (cm)		DIP ANGLE		ROUNDNESS	SYMMETRY
stoss	*lee*	*stoss*	*lee*	*stoss*	*lee*	*RDI*	*SI*
1.6	1.6	6.5	4.0	18	31	0.59	1.78
-0.1	0.4	0.7	1.0	-6	21	0.72	1.45
1.2	1.3	9.1	3.6	15	22	0.49	1.11
2.1	2.9	6.0	5.6	29	29	0.40	1.55
1.3	1.4	5.8	4.4	16	27	0.41	1.42
0.4	1.3	5.1	3.5	7	27	0.40	1.57
2.9	2.0	8.4	5.7	27	28		
0.1	0.2	2.2	1.7	14	9	n = 6	
1.3	1.0	6.0	2.7	20	27		
0.9	1.9	6.9	4.3	14	30		
2.3	1.7	8.8	4.9	22	29		
0.5	1.2	5.0	3.5	10	29		
1.9	1.9	7.7	5.5	30	28		
1.6	1.4	5.3	3.7	29	25		
1.1	1.3	4.0	3.8	24	28		
0.1	0.4	5.1	1.8	3	19		
3.0	20.0	10.9	4.9	25	29		
1.9	2.2	6.6	5.4	22	28		
1.2	0.9	5.5	3.3	20	20		
2.1	1.8	6.8	5.3	24	28		
3.2	0.9	5.3	3.9	25	18		
0.1	0.5	1.1	3.4	6	13		
0.2	1.2	2.8	3.9	7	32		
1.0	0.3	3.4	2.6	20	16		
1.1	1.0	4.1	4.0	16	23		
1.4	1.7	5.7	4.8	22	30		
0.8	0.9	6.0	2.9	12	25		
0.0	0.2	2.7	1.3	0	17		
0.2	1.2	2.8	3.2	7	29		
1.0	0.3	2.5	2.2	28	16		
2.3	1.3	4.9	4.7	35	22		
0.0	1.1	3.0	3.5	0	31		
1.2	0.9	3.5	3.4	27	27		
1.5	0.8	4.6	4.3	23	16		
0.2	0.9	2.2	2.7	6	30		
1.3	1.0	5.0	3.4	20	29		
0.1	0.1	1.6	1.4	7	5		
0.6	0.9	2.9	3.2	17	25		
1.1	0.9	5.2	2.8	20	27		
0.1	0.2	3.1	1.4	4	11		

n = 40

S12R4

HEIGHT (cm)		WAVELENGTH (cm)		DIP ANGLE		ROUNDNESS	SYMMETRY
stoss	*lee*	*stoss*	*lee*	*stoss*	*lee*	*RDI*	*SI*
1.3	2.0	4.8	4.3	25	30	0.60	1.35
0.5	0.8	2.9	2.0	18	32	0.52	1.59
0.3	1.4	8.1	2.9	10	33	0.62	1.45
1.6	1.5	5.8	3.3	31	29	0.68	2.04
1.6	1.3	5.8	3.1	27	30	0.48	1.71
0.4	0.4	10.4	1.7	5	16	0.55	1.71
0.0	0.2	2.8	0.7	0	18		
1.8	1.4	9.5	3.0	19	28	n = 6	
2.4	2.1	6.9	6.0	31	30		
0.8	0.8	6.0	5.6	14	10		
2.5	2.1	6.8	5.7	39	33		
0.6	0.7	4.6	2.1	14	31		
1.4	0.9	6.0	2.9	25	25		
-0.1	1.1	1.8	5.8	-8	13		
0.0	0.1	2.7	1.5	-3	8		
3.8	1.3	10.4	3.0	36	28		
1.9	1.8	7.1	4.6	23	30		
1.2	1.9	8.4	4.2	15	30		
3.4	1.8	8.2	4.2	31	29		
0.9	0.7	3.5	2.5	18	32		
0.7	0.1	5.3	1.7	14	3		
0.1	0.8	2.0	1.8	2	30		
0.0	1.1	2.9	2.3	0	34		
1.4	1.3	5.4	3.2	28	33		
2.9	0.6	5.2	2.1	35	30		
0.2	1.5	4.7	3.4	5	34		
1.9	1.2	5.4	3.5	27	32		
0.0	1.0	4.4	3.7	2	22		
1.7	1.2	3.8	3.7	36	32		
0.8	0.5	3.3	1.3	17	30		
0.1	0.9	2.7	1.9	2	33		
1.4	0.6	4.2	1.3	29	31		
-0.3	0.4	3.3	2.5	-7	18		
0.8	0.6	3.7	1.5	25	32		
1.2	2.0	4.7	4.3	19	38		
1.9	0.8	6.0	2.7	23	30		
1.2	1.0	5.8	2.5	18	32		
0.0	1.0	4.6	2.6	-2	33		

n = 38

S12R5

HEIGHT (cm)		WAVELENGTH (cm)		DIP ANGLE		ROUNDNESS	SYMMETRY
stoss	*lee*	*stoss*	*lee*	*stoss*	*lee*	*RDI*	*SI*
2.5	3.4	9.0	9.8	25	26	0.53	1.68
2.0	2.1	7.1	5.2	29	26	0.53	1.47
2.0	1.4	10.7	3.7	17	29	0.46	1.8
1.7	3.2	14.8	7.0	19	28	0.51	1.33
2.0	2.5	8.3	7.5	26	27	0.65	1.18
0.5	1.6	4.3	3.9	12	27	0.41	1.17
0.1	0.6	2.3	1.7	0	22		
-0.1	0.4	3.2	1.3	3	14	n = 6	
0.0	0.3	5.5	2.3	0	13		
0.7	0.3	7.1	3.5	10	9		
3.6	0.4	11.1	2.2	28	16		
2.2	1.2	6.9	5.2	28	22		
1.4	1.1	8.6	3.6	23	23		
0.4	0.2	5.9	3.3	9	29		
0.5	1.3	5.5	4.1	32	30		
3.0	2.2	7.7	5.7	23	25		
2.0	0.9	7.4	3.5	14	30		
1.1	1.3	5.5	3.0	21	30		
-0.1	0.7	1.2	2.1	20	32		
1.8	2.4	9.2	5.4	28	29		
1.4	1.6	5.3	3.7	21	30		
2.8	1.1	8.0	2.2	17	26		
-0.1	2.1	0.6	4.8	30	29		
2.3	1.4	11.8	3.7	2	25		
1.3	0.7	6.7	2.7	30	34		
1.9	1.2	4.6	3.4	26	28		
0.1	0.7	5.2	2.8	23	18		
1.9	2.2	7.3	4.4				
1.6	1.2	5.5	3.7	n = 27			
0.9	0.3	3.0	1.3				

n = 30

S13R1

HEIGHT (cm)	WAVELENGTH (cm)	DIP ANGLE		ROUNDNESS	SYMMETRY
		stoss	*lee*	*RDI*	*SI*
41.4	563	7 to 20	25	/	/
		2 to 11	40		
		5 to 16	33		
		n = 3	n = 3		

S13R2

HEIGHT (cm)	WAVELENGTH (cm)	DIP ANGLE		ROUNDNESS	SYMMETRY
		stoss	*lee*	*RDI*	*SI*
27.4	266	21	32	0.55	1.33
33.2	105	26	33		
34.3	133	18	22		
14.9		13	29		
14.0	n = 3	15			
10.4		29			
n = 6					

S13R3

HEIGHT (cm)		WAVELENGTH (cm)	DIP ANGLE		ROUNDNESS	SYMMETRY
stoss	*lee*		*stoss*	*lee*	*RDI*	*SI*
9.1	5.1	173.5	19	30	0.35	1.06
13.9	9.9	70.0	25	19	0.46	1.03
23.6	21.6	187.0	16	13	0.64	1.74
9.0	15.0	114.0	7	22		
16.2	20.2	142.0	16	14	n = 3	
6.0	8.0	74.0	12	22		
30.0	22.0	225.0				
			n = 6			
n = 7						

S13R4

HEIGHT (cm)		WAVELENGTH (cm)		DIP ANGLE		ROUNDNESS	SYMMETRY
stoss	*lee*	*stoss*	*lee*	*stoss*	*lee*	*RDI*	*SI*
20.7	25.7	102.0	44.0	7 to 14	29	0.70	2.32
19.3	20.3	122.0	43.0	6 to 15	32	0.43	2.84
22.1	23.1	97.0	49.0	4 to 14	30	0.61	1.98
22.1	19.7	142.0	61.0	3 to 14	24	0.51	2.49
26.3	24.9	114.0	60.0	4 to 17	28		
	26.3		57.0			n = 4	
n = 5		n = 5	49.0	n = 5			
	n = 6						
			n = 7				

S13R5

HEIGHT (cm)		WAVELENGTH (cm)		DIP ANGLE		ROUNDNESS	SYMMETRY
stoss	*lee*	*stoss*	*lee*	*stoss*	*lee*	*RDI*	*SI*
23.7	16.7	115.0	45.5	3 to 14	25	0.68	2.53
16.2	22.2	109.5	42.0	8	28	0.67	2.61
20.7	15.4	129.0	42.0	7 to 12	24	0.72	2.80
20.5	21.9	96.0	46.0	4 to 13	28	0.18	2.46
	22.7	112.4	46.0		26	0.56	
n = 4	17.5		39.0	n = 4	26		n = 4
		n = 5				n = 5	
	n = 6		n = 6		n = 6		

S13R6

HEIGHT (cm)		WAVELENGTH (cm)	DIP ANGLE		ROUNDNESS	SYMMETRY
stoss	*lee*		*stoss*	*lee*	*RDI*	*SI*
28.7	24.7	184.0	9 to 17	23	0.73	2.17
5.5	22.8	65.0	13	24	0.64	2.36
23.5	15.0	164.0	4 to 16	19	0.43	1.75
22.0	29.0	208.5	4 to 17	32		
26.1	18.1	151.0	19	21	n = 3	
10.8	15.8	88.0	10	28		
16.9	17.9	158.0		24		
			n = 6			
n = 7				n = 7		

S14R1
Plane bed

HEIGHT (cm)		WAVELENGTH (cm)		DIP ANGLE		ROUNDNESS	SYMMETRY
stoss	*lee*	*stoss*	*lee*	*stoss*	*lee*	*RDI*	*SI*
n/a	n/a	n/a	n/a	n/a	n/a	n/a	n/a

S14R2
Plane bed

HEIGHT (cm)		WAVELENGTH (cm)		DIP ANGLE		ROUNDNESS	SYMMETRY
stoss	*lee*	*stoss*	*lee*	*stoss*	*lee*	*RDI*	*SI*
n/a	n/a	n/a	n/a	n/a	n/a	n/a	n/a

S14R3
Plane bed

HEIGHT (cm)		WAVELENGTH (cm)		DIP ANGLE		ROUNDNESS	SYMMETRY
stoss	*lee*	*stoss*	*lee*	*stoss*	*lee*	*RDI*	*SI*
n/a	n/a	n/a	n/a	n/a	n/a	n/a	n/a

S15R1

HEIGHT (cm)	WAVELENGTH (cm)	DIP ANGLE		ROUNDNESS	SYMMETRY
		stoss	*lee*	*RDI*	*SI*
29.1	385	14 to 30	4 to 9	0.78	0.61
36.0	397	30	3 to 18	0.13	
34.7	395	30	3 to 12		
28.6		20 to 31	4 to 11	n = 2	
	n = 3				
n = 4		n = 4			

S15R2

HEIGHT (cm)	WAVELENGTH (cm)	DIP ANGLE		ROUNDNESS	SYMMETRY
		stoss	*lee*	*RDI*	*SI*
42.5	358.1			/	/

S15R3

HEIGHT (cm)		WAVELENGTH (cm)		DIP ANGLE		ROUNDNESS	SYMMETRY
stoss	*lee*	*stoss*	*lee*	*stoss*	*lee*	*RDI*	*SI*
30.3	30.3	153.0	55.0	4 to 13	13 to 31	0.60	1.43
28.8	28.8	157.0	110.0	14	9 to 24	0.37	1.34
		158.0	118.0				
		158.0					
			n = 3				
		n = 4					

S15R4

HEIGHT (cm)		WAVELENGTH (cm)	DIP ANGLE		ROUNDNESS	SYMMETRY
stoss	*lee*		*stoss*	*lee*	*RDI*	*SI*
31.0		230.0	3	30	/	/
		550.0				

S15R5

HEIGHT (cm)		WAVELENGTH (cm)	DIP ANGLE		ROUNDNESS	SYMMETRY
stoss	*lee*		*stoss*	*lee*	*RDI*	*SI*
28.5	28.5	243.0	11	30	0.71	3.67
32.5	32.5	423.0	4	30	0.75	6.42
29.4	29.4	420.0	5	25		
29.0	29.0	244.0	12	30		
n = 4						

S16R1

HEIGHT (cm)		WAVELENGTH (cm)		DIP ANGLE		ROUNDNESS	SYMMETRY
stoss	*lee*	*stoss*	*lee*	*stoss*	*lee*	*RDI*	*SI*
1.5	0.2	6.0	2.5	16	8	0.47	0.78
1.5	0.1	4.5	2.6	22	1	0.41	0.92
1.2	2.6	4.8	5.4	24	32	0.38	1.00
0.5	2.6	3.1	6.8	12	23	0.47	0.73
0.1	0.7	3.2	2.8	2	17	0.50	0.63
1.1	0.2	5.0	2.2	14	8		
1.8	1.0	7.4	3.1	20	21	n = 5	
0.2	1.1	1.8	2.5	8	30		
1.5	0.6	3.8	3.9	29	9		
1.1	1.6	5.5	6.5	18	16		
0.4	1.6	4.5	5.2	8	22		
1.1	2.8	7.5	5.8.	14	28		
1.7	0.3	5.9	2.2	18	6		
0.9	0.3	3.5	2.7	20	10		
0.4	0.1	3.9	6.9	7	7		
0.3	0.6	3.1	9.8	9	6		
1.1	0.7	4.5	6.2	20	6		
1.4	0.3	3.6	4.4	28	1		
0.5	0.2	2.2	3.1	17	1		
0.1	1.9	3.0	6.4	4	22		
0.6	0.5	4.3	2.5	14	10		
0.2	0.8	2.8	4.7	4	13		
1.3	0.4	4.5	2.6	21	9		
1.4	0.4	5.2	3.1	15	5		
0.7	1.1	2.9	5.6	14	10		
0.7	0.8	3.8	3.7	12	12		
0.3	0.3	2.8	2.2	5	7		
0.6	0.6	3.0	6.0	11	4		
1.1	1.6	3.7	7.2	23	13		
1.0	0.5	3.3	2.4	19	11		
1.6	1.1	5.5	6.0	15	8		
1.6	0.2	3.7	2.7	28	2		

n = 34

S16R2

HEIGHT (cm)		WAVELENGTH (cm)		DIP ANGLE		ROUNDNESS	SYMMETRY
stoss	*lee*	*stoss*	*lee*	*stoss*	*lee*	*RDI*	*SI*
0.2	1.8	2.8	4.7	2	25	0.56	1.13
1.6	0.2	3.5	1.9	33	2	0.51	0.97
0.8	1.1	3.4	6.2	20	7	0.46	1.49
0.3	0.9	2.1	4.8	10	11	0.63	1.20
0.7	1.6	4.6	6.5	8	16	0.51	1.90
1.9	1.3	2.1	4.8	18	19	0.35	0.98
1.0	0.8	6.6	2.4	13	14		
0.2	0.5	3.0	4.0	3	4	n = 6	
0.2	0.1	2.7	2.0	7	5		
1.1	0.5	4.5	4.0	22	5		
0.2	1.1	2.0	5.0	6	20		
0.2	0.2	1.5	2.0	5	6		
0.8	0.7	4.9	2.8	11	18		
1.5	0.8	6.0	2.4	18	20		
0.1	1.5	7.8	5.3	0	23		
2.6	1.5	7.5	5.1	24	20		
0.1	1.0	2.4	3.4	4	21		
0.9	0.3	8.1	3.9	4	17		
1.5	2.2	5.8	5.2	14	31		
0.3	0.3	4.7	1.5	6	10		
1.1	1.1	4.9	4.8	12	23		
0.7	0.5	2.8	3.3	12	12		
1.1	1.4	5.4	4.2	14	29		
2.2	1.0	6.7	3.3	27	28		
0.3	0.2	3.4	2.0	12	8		
0.3	0.3	2.8	2.5	13	10		
1.7	2.4	5.5	8.9	17	13		
1.8	1.3	7.8	3.9	17	28		
1.3	0.6	5.4	2.7	13	18		
0.3	0.8	3.4	2.8	5	23		

n = 30

S16R3

HEIGHT (cm)		WAVELENGTH (cm)		DIP ANGLE		ROUNDNESS	SYMMETRY
stoss	*lee*	*stoss*	*lee*	*stoss*	*lee*	*RDI*	*SI*
11.8	13.1	43.5	25.5	4 to 20	31	0.71	1.71
9.3	9.0	21.2	15.0	3 to 16	34	0.66	5.41
8.7	11.6	38.5	26.5	19	31	0.84	1.45
11.5	8.4	86.0	17.0	5 to 30	29	0.82	5.06

n = 4

S17R1

HEIGHT (cm)		WAVELENGTH (cm)	DIP ANGLE		ROUNDNESS	SYMMETRY
			stoss	*lee*	*RDI*	*SI*
/		/	/	/	/	/

S18R1

HEIGHT (cm)		WAVELENGTH (cm)	DIP ANGLE		ROUNDNESS	SYMMETRY
stoss	*lee*		*stoss*	*lee*	*RDI*	*SI*
10.5	17.4	193.0	9	15	0.66	1.17
14.1	10.9	73.0	28	24	0.39	0.70
8.0	8.9	125.0	19	9	0.49	1.68
5.2	15.6	70.0	10	20	0.38	0.75
16.8	8.7	166.0	28	12	0.41	0.57
11.8		70.0	17	23		
	n = 5			18	n = 5	
n = 6		n = 6	n = 6			
				n = 7		

S18R2

HEIGHT (cm)		WAVELENGTH (cm)	DIP ANGLE		ROUNDNESS	SYMMETRY
stoss	*lee*		*stoss*	*lee*	*RDI*	*SI*
9.6	8.0	59.0	12 to 21	20	0.31	2.40
11.4	8.0	86.5	4 to 15	22	0.51	1.31
11.1	15.8	131.5	14	25	0.53	2.12
9.4	10.2	118.0	16	14 to 26	0.36	0.59
11.7	13.7	132.5	3 to 17	26		
18.5	17.5	168.0	19	3 to 20	n = 4	
11.2	11.2	93.5	10	9 to 26		
n = 7						

S18R3

HEIGHT (cm)		WAVELENGTH (cm)		DIP ANGLE		ROUNDNESS	SYMMETRY
stoss	*lee*	*stoss*	*lee*	*stoss*	*lee*	*RDI*	*SI*
13.5	13.5	105.0	35.0	14	22	0.48	2.99
9.5	13.5	78.0	30.0	8 to 14	21 to 35	0.43	2.62
13.8	14.8	72.0	29.0	8 to 15	34	0.49	2.48
14.0	15.0	59.0	32.0	15	20 to 26	0.46	1.24
6.3	14.0	84.0	35.0	7	28	0.67	2.72
	12.7	74.0	26.0	4 to 8	31	0.20	2.80
n = 5	15.3		27.0		30		
		n = 6		n = 6		n = 6	
	n = 7		n = 7		n = 7		

S18R4

HEIGHT (cm)		WAVELENGTH (cm)		DIP ANGLE		ROUNDNESS	SYMMETRY
stoss	*lee*	*stoss*	*lee*	*stoss*	*lee*	*RDI*	*SI*
12.0	18.7	84.0	30.0	12	31	0.58	4.32
23.7	24.6	160.0	37.0	7	34	0.66	2.80
24.2	19.5	153.0	44.0	10	30	0.57	4.25
		124.0	46.0		28		
n = 3			36.0	n = 3	30	n = 3	
		n = 4					
			n = 5		n = 5		

S18R5

HEIGHT (cm)	WAVELENGTH (cm)	DIP ANGLE		ROUNDNESS	SYMMETRY
		stoss	*lee*	*RDI*	*SI*
27.2	224.0	/	/	/	/